Development and Commissioning of a Double-Prism Spectrometer for the Diagnosis of Femtosecond Electron Bunches

Dissertation zur Erlangung des Doktorgrades

an der Fakultät für Mathematik, Informatik und Naturwissenschaften
Fachbereich Physik
der Universität Hamburg

vorgelegt von

Dipl.-Phys. Steffen Wunderlich
aus Siegen

Hamburg
2016

Folgende Gutacher empfehlen die Annahme der Dissertation:
Herr Prof. Dr. Brian Foster
Herr Dr. Jens Osterhoff

Prüfungskommission der Disputation:
Frau Prof. Dr. Caren Hagner (Vorsitz)
Herr Prof. Dr. Brian Foster (einfaches Mitglied)
Frau Prof. Dr. Gudrid Moortgat-Pick (einfaches Mitglied)
Herr Dr. Jens Osterhoff (einfaches Mitglied)
Herr PD Dr. Bernhard Schmidt (einfaches Mitglied)

Datum der Disputation: 14.10.2016

Abstract

Development and Commissioning of a Double-Prism Spectrometer for the Diagnosis of Femtosecond Electron Bunches

Free-electron lasers as accelerator-driven light sources and wakefield-based acceleration in plasmas require the knowledge of the longitudinal extension and the longitudinal current profile of the involved electron bunches. These bunches can yield lengths below 10 µm, or durations shorter than approx. 33 fs, as well as charges less than 30 pC. During this work, transition radiation from relativistic electron bunches was investigated in the mid-infrared wavelength regime. A spectrometer using an arrangement of two consecutive zinc selenide prisms was developed, built and commissioned. The instrument covers the spectral range from 2 µm to 18 µm in a single shot. Measurements with the double-prism spectrometer were conducted at the FEL facilities FLASH at DESY in Hamburg, Germany and FELIX at the Radboud Universiteit in Nijmegen, The Netherlands. The assessment of the spectrometer and comparative studies with established diagnostic devices at FLASH show high signal-to-noise ratios at bunch charges below 10 pC and confirm the obtained results.

Linear accelerators, Free-electron laser, Laser-driven acceleration, Other advanced accelerator concepts, Transition radiation, Infrared spectrometers, Optical system design

Zusammenfassung

Entwicklung und Inbetriebnahme eines Doppelprismen-Spektrometers zur Untersuchung von Femtosekunden-Elektronenpaketen

Freie-Elektronen Laser als beschleuniger-getriebene Lichtquellen und Plasma-Kielfeldbeschleuniger benötigen die Kenntnis der Länge und des longitudinalen Stromprofils der beschleunigten Elektronenpakete. Diese Pakete weisen Längen von unter 10 µm bzw. Pulsdauern kürzer als 33 fs, sowie Gesamtladungen unterhalb von 30 pC auf. In dieser Arbeit wurde Übergangsstrahlung relativistischer Elektronenpakete im mittleren Infrarotbereich untersucht. Ein Spektrometer, welches auf einer Doppelprismen-Anordnung basiert, wurde entwickelt, aufgebaut und in Betrieb genommen. Das Spektrometer deckt den Wellenlängenbereich zwischen 2 µm und 18 µm in einer Einzelschussmessung ab. Messungen mit dem Doppelprismen-Spektrometer wurden an den FEL-Anlagen FLASH bei DESY, Hamburg, Deutschland und FELIX, betrieben von der Radboud Universiteit, Nijmegen, Niederlande, durchgeführt. Die Untersuchung und der Vergleich des Spektrometers mit existierenden Instrumenten am FLASH-Linearbeschleuniger zeigen hohe Signal-zu-Rausch-Verhältnisse bei Paketladungen unter 10 pC und bestätigen die Ergebnisse aus genommenen Messdaten.

Linearbeschleuniger, Freie-Elektronen Laser, Laser-getriebene Beschleunigung in Plasmen, andere Beschleunigungskonzepte, Übergangsstrahlung, Infrarotspektrometer, Design optischer Systeme

Contents

List of Figures

List of Tables

Introduction

The operation of electron accelerators as light sources gained more and more importance within the last decades. Synchrotrons, storage rings as well as free-electron lasers can deliver intense light pulses of high brightness in wavelength regimes where no optical laser are available. *Brightness* is a measure of the photon beam quality, that essentially accounts for source size, divergence and the photon flux in a defined spectral bandwidth. These accelerator-driven light sources are suited for experiments that demand for x-ray, ultraviolet and infrared light with strong requirements in intensity, spectrum and radiation pulse length [1].

Synchrotron radiation intrinsically provides a broad spectrum. However, experiments that require a small spectral bandwidth need a monochromator and suffer from the inherent strong decrease of the intensity. The concept of the free-electron laser (FEL) can mitigate this feature by the amplification of a defined and tunable spectral line of high brightness and a spectral line width on the level $\lesssim 1\,\%$. Here, a beam of electron bunches passes a periodic arrangement of magnetic fields, an undulator, where an interaction between the electron bunches and the electric field of a light wave can occur: an energy transfer from the electron beam to the light wave leads to the amplification of the latter. Depending on the wavelength regime, the FEL process is used for light captured in an optical cavity or in a linear arrangement of several undulators [2].

A special class of experiments aims for the study of molecular processes that elapse on the sub-picosecond level. Figuratively speaking, short exposure times, or equivalently, light pulse durations on the same scale are needed to resolve the dynamics. The FEL can particularly deliver radiation pulses that also fulfil the demand for radiation pulse durations of just a few femtoseconds, $10^{-15}\,\mathrm{s}$. The photon pulse duration is predominately determined by the dura-

tion of the electron bunches that drive the FEL process. The electron bunches are provided by linear accelerators and are prepared for sub-picosecond durations by compression at relativistic energies. A detailed understanding of the compression and the knowledge about the longitudinal current profile is an unalienable requirement for the achievement and control of ultrashort photon pulse durations within the FEL process [2–4].

Due to the field gradients which by far exceed the limits of conventional RF-based accelerators, laser- and particle beam-driven acceleration in plasmas are the subject of intense research and development aiming for driving FELs and colliders for particle physics. Plasma wakefield-based accelerators can deliver sub-10 fs electron bunches by design and also require the longitudinal diagnosis of the accelerated bunches, as well as for the bunches that drive the wakefield, for the investigation of the acceleration process itself [5–7].

The investigation of the spectral composition of the longitudinally compressed Coulomb field of relativistic electron bunches offers an approach for the diagnosis of electron bunches of femtosecond durations, whereas time-domain methods become technically and monetarily challenging. The phenomenon of the coherent emission of secondary radiation from the ultra-relativistic electrons is of particular interest [8, 9].

The investigation of the spectral level of coherence with spectroscopic instruments enables the reliable determination of the length and moreover, a likely current profile of the emitting collective of electrons. The spectral range of interest for sub-picosecond electron bunches ranges from the visible light to the far-infrared, but shifts to shorter wavelengths for decreasing bunch length. For instance, for bunch lengths below 3 µm, that correspond to durations < 10 fs, the mid-infrared is identified to be of special interest.

This work addresses the spectral investigation of transition radiation in the spectral regime of the mid-infrared between 2 µm to 20 µm, that is emitted by short and high-relativistic electron bunches of charges well below 30 pC.

The monograph at hand is structured as follows. The basic concepts of electron acceleration, transition radiation as a secondary radiation from relativistic electron bunches and spectroscopy are introduced in the first part. The second part describes the development and the application of a double-prism spectrometer that is then confirmed to be particularly suited for ultrashort

and low-charge electron bunches. A collection of supplementary information on the depicted developments and studies is followed by the bibliography and the list of the author's publications.

Part I

Theory

1 Principles of electron acceleration and free-electron lasers

Accelerators for elementary particles and ions are today widely applied in various fields. Besides their use for industrial material manipulation and sterilisation [10], state-of-the-art accelerators were originally built and operated for particle and nuclear physics [1]. Since the experimental evidence for synchrotron radiation in 1947 [11, 12], synchrotrons, storage rings and linear accelerators for electrons as well as positrons, are designed and operated as light sources. Accelerator-driven light sources are of particular interest in wavelength ranges where no lasers of suitable beam parameters are available. Examples are hard x-rays with wavelengths at the Å-scale to the ultraviolet (tens of nanometres) and in the infrared with $\lambda > 5\,\mu\text{m}$ [2].

The first chapter of this thesis shortly introduces the basic concepts of free-electron lasers (FELs), which impose several key requirements for the driving electron beam such as the length of the accelerated bunch of electrons. Subsequently, conventional electron acceleration based on electromagnetic fields in vacuum and wakefield-based acceleration in plasmas are introduced.

1.1 Free-electron lasers

Electromagnetic radiation is emitted whenever the momentum of a charged particle is changed. The radiation, that is emitted by particles at relativistic velocities, is concentrated into the direction of the particle's motion due to the Lorentz transformation into the laboratory frame [13]. The term *bremsstrahlung* in particular is associated with decreasing the longitudinal momentum of par-

ticles in matter due to the deflection at the electrons and nuclei, whereas synchrotron radiation is emitted when transverse momentum is imprinted onto the electron, e. g. by a dipole magnet in a synchrotron or storage ring (confer, for instance, [11, 13] and [14, p. 798]).

In order to satisfy the requirement for a photon beam with a small spectral bandwidth, the continuous and broad spectral intensity distribution of synchrotron radiation has to be spectrally truncated by a monochromator. The inherent loss in usable intensity can be immense.

A periodic arrangement of alternating magnetic fields, a wiggler or an undulator, forces the electron to radiate light that, due to interference, consists of a single narrow-band spectral line. The subsequent depiction follows the references [2, 15] and [16].

The properties of the emerging light depend on the magnetic design. The fundamental centre wavelength, λ_{UR}, for an electron passing through the undulator centre is given by the expression

$$\lambda_{\mathrm{UR}} = \frac{\lambda_u}{2\gamma^2}\left(1 + \frac{K^2}{2} + \gamma^2\Theta^2\right), \tag{1.1}$$

where λ_u is the magnetic period length and K denotes the undulator parameter that exhibits, among others, a linear dependency of the magnetic field strength on the electron axis. Θ is the observation angle with respect to the beam axis in the deflection plane. Typical values for the undulator parameter at FELs are between 1 and 4. In the case of $K \gg 1$, which corresponds to high deflection amplitudes, the emitted radiation spectrum contains many higher orders. The envelope of the spectral intensities reflects the continuous spectrum of synchrotron radiation from a single dipole magnet. Such a configuration is often denoted as a *wiggler* [1, 13].

The FEL is characterised by the stimulated emission of light by an incident light wave in the presence of an electron bunch in an undulator. A light wave can interact with the electron bunch such that energy transfer occurs in both directions. By the appropriate choice of the electron beam and undulator parameters, an exponential enhancement of the intensity of the light wave can be achieved.

The essential condition for an energy transfer between an existing light wave and an electron beam in an undulator is fulfilled for the resonance wavelength

that equals the wavelength of undulator radiation, $\lambda_r = \lambda_{\mathrm{UR}}(\gamma = \gamma_r)$, as defined by eqn. (1.1).

Within the electron bunch, periodic sections gain and lose energy from the light wave. This leads to a periodic energy modulation of the bunch. Since the path length of the sinusoidal movement in the undulator is energy-dependent, a modulation of the longitudinal particle density arises. At resonance energy, the density modulation with length, λ_r, is symmetric with respect to the zero-crossing of the electric field of the light wave. Thus, the net energy transfer between electron bunch and light wave is zero.

If the mean energy of the electron bunch is slightly above the resonance energy, the phase of the longitudinal particle density with respect to the electric field of the light shifts such that an increasing number of electrons transfer energy to the light wave. A positive net energy transfer from the electron bunch to the light occurs for a certain number of undulator periods.

The *FEL gain length* is the undulator distance in which the power of the light rises by e and depends on undulator and electron beam parameters. The gain length is typically on the metre-scale, for example 1.25 m at $\lambda = 13\,\mathrm{nm}$ at the FLASH facility in Hamburg and 3.5 m ($\lambda = 0.15\,\mathrm{nm}$) at LCLS at Stanford [2].

A saturation in the intensity gain after a certain undulator length is, without adjustments of e. g. the parameter K in eqn. (1.1), inevitable. With increasing undulator length, more and more particles slip into phase regions where a negative energy transfer occurs. The saturation power is connected to the electron beam power by the *FEL* or *Pierce parameter*, which accounts for example for the undulator parameter, beam charge and energy. The Pierce parameter is typically on the order of 10^{-3}.

For optical and infrared wavelengths, the enhancement in radiation power is carried out during multiple round trips of light pulses in an optical cavity that encloses an undulator with length shorter than one gain length: a *FEL oscillator* (FELO), cf. Fig. 1.1. In practice, a linear accelerator delivers a pulsed electron beam that is guided via dipole magnets onto the undulator central axis and dumped into an absorber after passing through the undulator.

However, the intensity gain must be achieved in a single passage through a long undulator or multiple consecutive undulators in wavelength regimes where

no mirrors of sufficient reflectivity exist. The positive energy transfer for more than one gain length in such *high-gain free-electron lasers* relies on a second characteristic of the FEL process apart from the energy transfer between light and electron beam, namely the change of the phase of the light wave. The phase between the light wave and the peak of the electron density modulation is shifted and ensures an exponential energy gain with respect to the passed undulator length until saturation.

Undulator radiation from, for instance, the beginning of the undulator chain of a high-gain FEL, can act as the seed for the amplification process within a FEL. The mechanism is accordingly named Self-Amplified Spontaneous Emission (SASE) and is a widely used operation mode. An equivalent interpretation is the start of the FEL process from a longitudinal density modulation of the randomly distributed electrons in the bunch, i. e. shot noise. However, this circumstance results in a band of wavelengths λ_r and longitudinal modes that can be amplified. The actual spectral distribution of self-amplified radiation differs from shot to shot [2].

In order to control the amplified wavelength and to increase the shot-to-shot stability, various seeding techniques have been studied and demonstrated. Here, external light is coupled into the FEL and predefines the amplified wavelength [17–22].

The transverse emittance and the shape of the longitudinal phase space of the bunch, i. e. the peak current, bunch length and energy spread are the electron beam parameters which define the FEL gain and photon beam quality. The quality criterion of the photon pulse length is of particular interest for experiments aiming for the temporal analysis of e. g. molecular processes with x-rays [23–25]. The length or temporal duration of pulses for such experiments are requested to be on the scale of a few microns or femtoseconds respectively. This demand, which cannot be satisfied with synchrotron radiation, implies a detailed knowledge of the emitting electron bunch that yields lengths on the same scale.

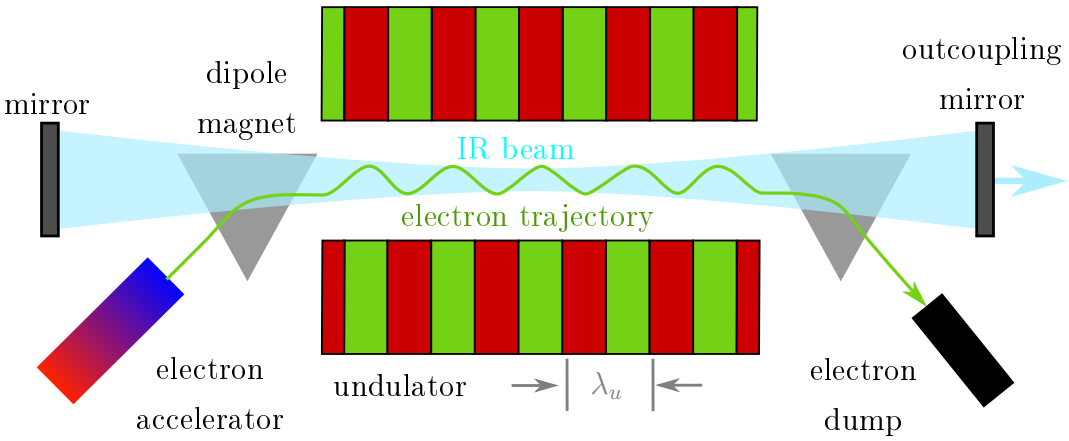

Figure 1.1: Simplified and idealised schematic of a free-electron laser oscillator (FELO). The optical cavity is omitted in the case of a high-gain FEL. The drawing is not to scale and is adapted from [26]. Please note that the electron oscillations are perpendicular to the magnetic field lines of the undulator magnets.

1.2 Conventional RF accelerators

The first linear accelerator was built by Wideröe in 1928 as a demonstration experiment [27], where potassium and sodium ions were accelerated via alternating electromagnetic fields between drift tubes. The lengths of the structures is proportional to $\beta_c = v/c$, with the velocity, v, and the speed of light, c, in order to reach the accelerating phase of the RF field in the successive tube gap. Since radio frequency (RF) amplifiers were available only up to a few MHz, the concept of acceleration between drift tubes was only suitable for non-relativistic velocities [1].

The development of the klystron in the late 1930s enabled the generation of high-power RF fields with frequencies in the GHz range [1, 28], which was required to decrease the length of the drift tube arrangement for relativistic particle velocities, $\beta_c \to 1$. Alvarez refined the structure used by Wideröe by enclosing the drift tubes with a metallic shielding, which acted together as a resonator and avoided radiative losses of the RF power [1], [14, p. 799].

Aside from circular electron accelerators like the betatron (1941) [29] and the synchrotron (1945) [1, 30], the first linear accelerator (linac) for electrons was built by Hansen et al. in 1947, who used disc-loaded RF resonators and

travelling waves [31].

Nowadays, the acceleration of elementary particles is conducted in radio frequency resonators or cavities, via a time-dependent electric field, $E_{\mathrm{acc}}(t)$, on the centre axis. The resonator radius is given by the frequency of the RF wave, $f_{\mathrm{acc}} = \omega_{\mathrm{acc}}/(2\pi)$. ψ denotes a phase offset of the RF field with respect to the centre of the electron bunch.

$$E_{\mathrm{acc}}(t) \;=\; E_{\mathrm{grad}}\, \cos(\omega_{\mathrm{acc}} t + \psi) \tag{1.2}$$

The electric field gradient, E_{grad}, strongly depends on the design of the RF cavities. In normal-conducting (NC) cavities, the thermal load, induced by resistive losses in the material, and breakdown effects, due to field emission, limit the gradient amplitude as well as the time for which the maximum gradient can be exposed to the resonator. Current research programmes have reported gradients on the order of $100\,\mathrm{MV\,m^{-1}}$ [32, 33].

In the case of superconducting (SC) cavities, the maximum gradient is determined by effects leading to the breakdown of the superconducting state. Apart from the critical temperature of 9.2 K for niobium, the critical magnetic field is of particular importance for the resonator operation. In the case of the TESLA-type cavities, the limiting magnetic field is on the order of 240 mT, whereas the design value of the peak magnetic field during operation, B_{peak}, is connected to the accelerating electric field by $B_{\mathrm{peak}}/E_{\mathrm{acc,\,max}} = 4.26\,\mathrm{mT\,MV^{-1}\,m}$. This predicts an ideal peak gradient of approx. $55\,\mathrm{MV\,m^{-1}}$. The design gradient for the European x-ray free-electron laser (European XFEL) is $23.6\,\mathrm{MV\,m^{-1}}$, whereas gradients of $35\,\mathrm{MV\,m^{-1}}$ have already been achieved [34–36].

Besides the beam energy, the peak current of the electron bunches is crucial for the operation of a FEL. The peak current is defined by the longitudinal electron bunch length and the number of contained particles. Peak currents of a few kA are commonly achieved by compression in magnetic chicanes, since the generation and acceleration of electron bunches with µm lengths at low energies is restricted due to space charge effects [37].

A longitudinal position-energy dependency is introduced by the appropriate choice of the phase, ψ, in formula (1.2). The longitudinal phase space of the electron bunch, energy versus longitudinal position, is adjusted in the accelerating structures until the bunch head has a lower energy than the tail,

or, yields a negative energy slope. A linearisation of the cosine-like dependency, that is imprinted by the curvature of the accelerating field, is possible by using a cavity operated at a higher harmonic of the accelerating frequency [38]. Due to the momentum-dependent deflection induced by dipole magnets, a chicane setup can be chosen to longitudinally compress the electron bunch. However, collective effects such as coherent synchrotron radiation and space charge forces can negatively influence the longitudinal phase space and thus, the FEL process [2, 39].

At free-electron lasers for x-ray and extreme ultraviolet (EUV) photon pulses, electron bunch lengths well below 30 fs have been reported, such as 11 fs (FWHM) at LCLS at SLAC [3] and approx. 24 fs (r.m.s.) at FLASH at DESY [4].

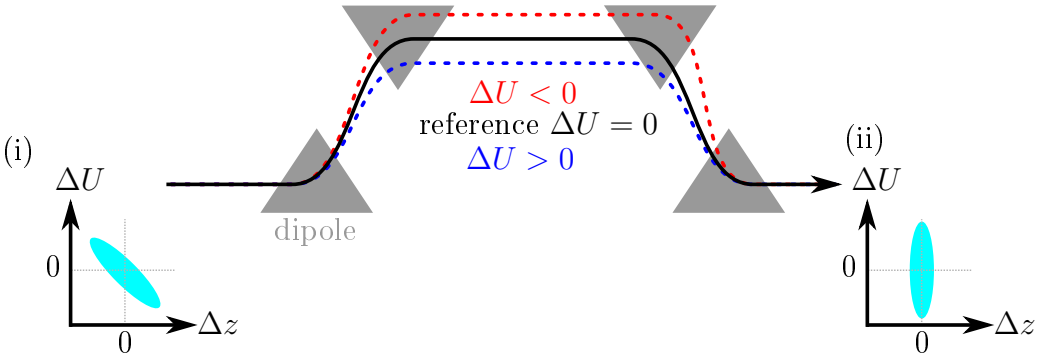

Figure 1.2: Simplified and idealised schematic of the electron bunch compression in a magnetic chicane. The RF field in the accelerating modules imprints a position-energy dependency onto the bunch, that is indicated in the phase space diagram (i). The energy distribution leads, due to the momentum-dependent deflection of the dipole magnets, into a longitudinal rearrangement of the electron bunches (ii). The depiction is adapted from [40].

1.3 Plasma-based acceleration of electrons

In 1956, V. I. Veksler proposed the possibility to generate an electric field, that is supposed to accelerate particles, by the excitation of a particle density mod-

ulation in a plasma [5]. The density modulation, a plasma wave, is invoked by an externally accelerated electron beam and can, if the excitation amplitude and the plasma properties are appropriate, be accompanied by wakefields with high electric field strengths in longitudinal and transverse direction. In comparison to plasma-wakefield acceleration (PWFA), the approach of laser-wakefield acceleration (LWFA) employs an intense laser pulse to generate the density modulation in a plasma [6, 41].

An important property of a plasma, considered as an externally neutral collective of electrically charged and neutral constituents, is the plasma frequency,

$$\omega_p = \sqrt{\frac{n_e\, q_e^2}{\varepsilon_0\, m_e}}, \tag{1.3}$$

with the plasma electron density, n_e, vacuum permittivity, ε_0, elementary charge, q_e, and electron mass, m_e [42]. Typical plasma densities for plasma-based accelerators are $(10^{17} - 10^{19})\,\mathrm{cm}^{-3}$, which result into plasma frequencies of approx. $(2 \times 10^{13} - 2 \times 10^{14})\,\mathrm{s}^{-1}$. The resulting wavelengths, $\lambda_p \simeq 2\pi c\,\omega_p^{-1}$, are approximately 106 µm and 11 µm respectively [43, 44].

A suitable driver with a duration on the order of $\lambda_p\, c^{-1}$, a laser pulse or an electron bunch, generates a plasma wave. The shape of the longitudinal electric field of this wave depends, among others, on the excitation strength of the wave. Transversally focusing and defocusing fields are also excited. The plasma waves for small excitation amplitudes are sine-like with wavelength λ_p (linear regime). In the highly nonlinear regime, often called blow-out regime, pronounced longitudinal density peaks arise due to the radial expulsion of almost all plasma electrons around the driver trajectory, where a electron-free bubble or cavity is formed [6, 45]. Hence, strong accelerating fields are created. A comparison of the shape of the plasma wave, potential and longitudinal electric field for the linear, quasi non-linear and highly non-linear regime is depicted in Fig. 1.3.

Electrons are injected into the accelerating and focusing phase of the plasma wave-induced fields via different processes. The capturing of plasma electrons from the plasma wave itself via the electric fields, via longitudinal density gradients and via injection by the ionisation of a dopant gas have been studied in addition to the utilisation of multiple laser pulses and external electron

sources [6, 45].

The expected length of the accelerated electron bunches is determined by the length of the accelerating, and moreover the focusing phase, of the plasma wave, that is considered to be approx. $\lambda_p/4$ [46].

Examples for experimental realisation of plasma-based accelerators are capillary waveguides and gas jets as well as metal vapor ovens [43, 47–49]. A PWFA experiment showed a gradient of $52\,\mathrm{GV\,m^{-1}}$ over a distance of 0.85 m in a lithium vapor oven [43]. Electron bunches with energies up to 4.2 GeV, accelerated via LWFA in a 9 cm-long capillary discharge waveguide have been reported by [48].

Up to now, electron beams from plasma-based accelerators yield energy spreads on the percent level and pronounced shot-to-shot fluctuations. The improvement of these properties is still the subject of investigations, which eventually aim for staged plasma-based accelerators and driving a free-electron laser with the accelerated electron bunches [45].

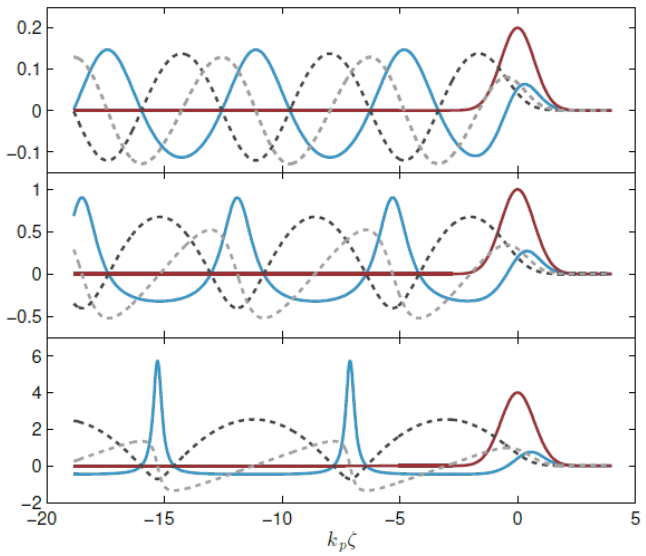

Figure 6: Transition from linear to nonlinear plasma waves for driver amplitudes of $a_0 = 0.2$, $a_0 = 1.0$ and $a_0 = 4.0$ (top to bottom). The individual graphs show the normalized laser intensity of the circular polarized pulse $\mathbf{a}^2$ (—), wakefield potential ψ (- -), longitudinal electric field E_z/E_0 (- -), and plasma electron density perturbation $n/n_0 - 1$ (—).

Figure 1.3: Comparison of plasma waves for different excitation regimes. The parameter a_0 denotes the amplitude of the vector potential of the driving laser pulse, normalised to the electron rest energy. The abscissa reads the plasma wave number, $k_p = \omega_p\, c^{-1}$, and the longitudinal coordinate, ζ, in the frame co-moving with the driver. By courtesy of T. Mehrling [45, p. 49].

2 The longitudinal diagnosis of femtosecond electron bunches

The determination of the longitudinal current profile of relativistic electron bunches with lengths and substructures on the order of 10 µm is a challenging task, which gained importance with the advances in laser- and particle beam-driven wakefield acceleration and conventional accelerators driving free-electron lasers. The former intrinsically delivers, depending on the realisation, bunches on the µm-scale, whereas the latter demands, in order to produce photon pulses of such lengths, electron bunches on the same length scale (cf. sections 1.1 and 1.3 respectively).

Regarding the scope of this monograph, the chapter at hand gives a brief synopsis of possible measurement techniques with frequency-domain methods using coherent radiation presented in more detail. Figure 2.1 illustrates the operation principles of the introduced methods.

The reader may find more details e. g. in [4, 50] and [51].

2.1 Time-domain methods

The mapping of the longitudinal plane into a transverse plane with a transverse deflecting structure (TDS) is a widely used technique to access the longitudinal current distribution of electron bunches at relativistic energies, $\beta_c \approx 1$. In analogy to photoelectrons in optical streak cameras [54, 55, and references cited therein], an arrangement of radio frequency cavities is utilised to apply a position-dependent sinusoidal transverse kick to the electron bunch. The zero crossing of the RF field amplitude is set close to the longitudinal centre of the bunch. Hence, the head and tail of the particle distribution experience transverse momenta that are different in amplitude and direction. In a drift

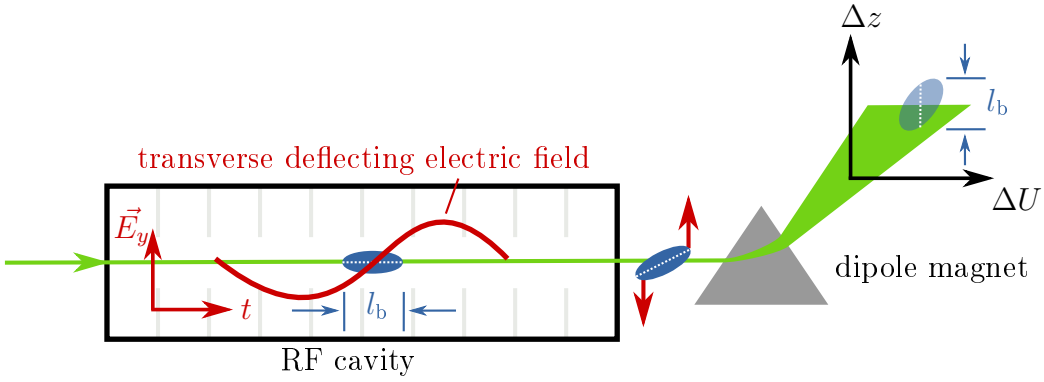

(a) transverse deflecting structure (TDS)

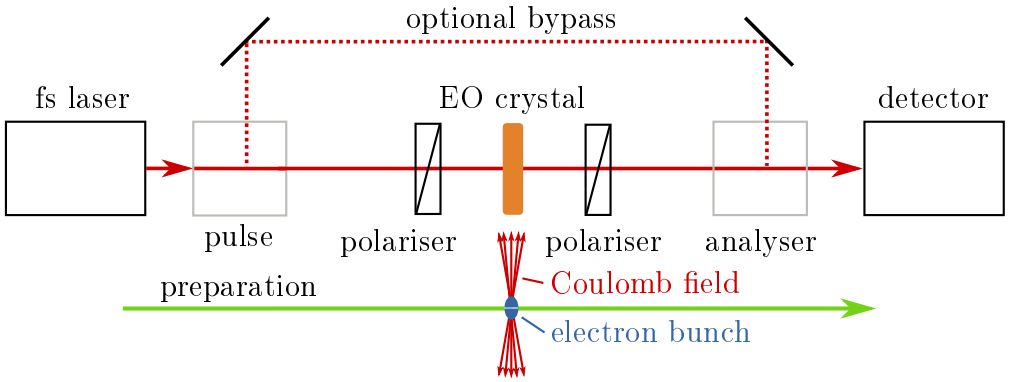

(b) electro-optic (EO) methods

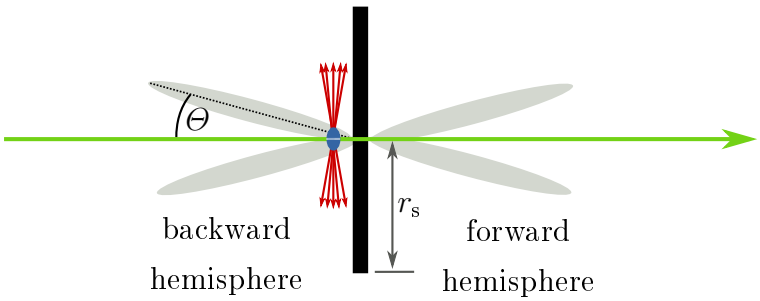

(c) transition radiation (TR)

Figure 2.1: Schematics of selected longitudinal diagnostics for relativistic electron bunches. The figures were adapted from [52, 53] and [26].

space, the position-dependent momenta lead to a shearing of the bunch: the longitudinal axis is transferred into the transverse plane and is now observable via a scintillation screen [56–59].

The resolution in electron bunch length is predominately set by the amplitude and frequency of the deflecting RF field, by the magnet optics defining transverse size of the non-sheared electron beam in the observation plane and the resolution of the subsequent optical imaging system. A transverse deflector installed at the Linac Coherent Light Source (LCLS) at the Stanford Linear Accelerator Center (SLAC) showed resolutions of $(1-4)\,\mathrm{fs}$ (r.m.s.) for different electron beam energies, which corresponds to $0.3\,\mu\mathrm{m}$ and $1.2\,\mu\mathrm{m}$ respectively. The operation frequency is approx. $11.4\,\mathrm{GHz}$ [3, Supplementary Note 1]. Measurements with the TDS at the FLASH facility ($f = 2.856\,\mathrm{GHz}$) yielded r.m.s. resolutions between $6\,\mathrm{fs}$ and $15\,\mathrm{fs}$ ($1.8\,\mu\mathrm{m}$ and $4.5\,\mu\mathrm{m}$) [4].

However, the TDS measurement is a destructive measurement - the sheared electron bunch cannot be used for e. g. driving a FEL. For superconducting linear accelerators that provide bunch trains, this feature can be mitigated by the operation by combining a pulsed RF deflector with a pulsed kicker magnet that picks one sample bunch from the bunch train [60]. The placement of the TDS behind the FEL undulators, as present at the normal-conducting linac of LCLS, also enables the study of the FEL process [3, 57, 61].

The investigation of the transversally concentrated Coulomb field of the relativistic electron bunch [13] with electro-optic (EO) methods allows, within certain limits, the estimation of the bunch length and the current profile. The EO effect can be regarded as the electric field-induced phase modulation in an optically active crystal. This modification can be probed with a laser pulse in different configurations. The temporal resolution of electro-optic techniques are limited to about $10\,\mu\mathrm{m}$ and is still the subject of further studies [62–65].

2.2 Frequency-domain methods

In the case where measurements in the time domain and EO techniques are no longer applicable due to approaching the respective resolution limits, the spectral composition of the Coulomb field of a relativistic electron bunch can be investigated [8, 9].

The radiation emitted by an electron bunch at relativistic energies is examined in the spectral ranges where the emission is incoherent with an intensity proportional to the number of particles in the bunch, N, and where coherent emission with a dependency on N^2 occurs. The following derivation, which has been adapted from [66] and [67], demands equal emission properties for each of the individual non-correlated electrons in the bunch and is, when preserving this constraint, valid for various emission processes such as synchrotron radiation, diffraction radiation and transition radiation.

The spectral energy density, $\frac{\mathrm{d}^2 U}{\mathrm{d}\,\omega\,\mathrm{d}\,\Omega}$, follows the Fourier transform (FT) of the electric field, $\vec{E}^*(\omega) = \mathrm{FT}(\vec{E}(t))$, that is emitted by a bunch of N electrons:

$$\frac{\mathrm{d}^2 U}{\mathrm{d}\,\omega\,\mathrm{d}\,\Omega} \propto \left\langle \left| \vec{E}^*(\vec{k}) \right|^2 \right\rangle, \tag{2.1}$$

with the wave vector, $\vec{k} = \frac{\omega}{c}\,\vec{n}$, angular frequency ω, solid angle, Ω, and the speed of light in vacuum, c. The brackets indicate the ensemble average. The normal vector, $\vec{n}$, points from a chosen reference particle in the electron bunch towards the observation point that is located at a large distance from the reference particle. The distance between the two points is denoted by d_{ref}.

The quantity $\vec{E}^*(\vec{k})$ can be expressed by the superposition of the single-electron components, $\vec{E}_1^*(\vec{k})$:

$$\vec{E}^*(\vec{k}) \;=\; \vec{E}_1^*(\vec{k}) \sum_{j=1}^{N} e^{i\,\vec{k}\,\vec{r_j}}, \tag{2.2}$$

where the vector $\vec{r_j}$ is defined between the particle j and the reference particle. Equation (2.1) now yields the form

$$\frac{\mathrm{d}^2 U}{\mathrm{d}\,\omega\,\mathrm{d}\,\Omega} \;=\; \left(\frac{\mathrm{d}^2 U}{\mathrm{d}\,\omega\,\mathrm{d}\,\Omega}\right)_1 \left\langle \left| \sum_{j=1}^{N} e^{i\,\vec{k}\,\vec{r_j}} \right|^2 \right\rangle. \tag{2.3}$$

The ensemble average can be written as

$$\begin{aligned} \left\langle \left| \sum_{j=1}^{N} e^{i\,\vec{k}\,\vec{r_j}} \right|^2 \right\rangle \;&=\; \left\langle \sum_{j=1}^{N} e^{i\,\vec{k}\,\vec{r_j}} \sum_{l=1}^{N} e^{-i\,\vec{k}\,\vec{r_l}} \right\rangle \\ &=\; \sum_{j=1,l=j}^{N} e^{i\,\vec{k}\,(\vec{r_j}-\vec{r_l})} + \left\langle \sum_{j=1}^{N} e^{i\,\vec{k}\,\vec{r_j}} \right\rangle \left\langle \sum_{l=1,l\neq j}^{N} e^{-i\,\vec{k}\,\vec{r_l}} \right\rangle. \end{aligned} \tag{2.4}$$

The first part, $\sum_{j=1,l=j}^{N} e^{i\,\vec{k}\,(\vec{r_j}-\vec{r_l})}$, reduces to the number of particles in the bunch, N.

The translation property of the Dirac delta function [68],

$$f(\vec{x}) \;=\; \int\limits_{-\infty}^{\infty} \delta(\vec{y}-\vec{x}) f(\vec{y})\,\mathrm{d}\,\vec{y},$$

allows the two remaining factors in (2.4) to be expressed as

$$\sum_{j=1}^{N} e^{i\,\vec{k}\,\vec{r_j}} \;=\; \sum_{j=1}^{N} \int\limits_{-\infty}^{\infty} \delta(\vec{r}-\vec{r_j})\, e^{i\,\vec{k}\,\vec{r}}\,\mathrm{d}\,\vec{r} \tag{2.5}$$

and

$$\sum_{l=1,l\neq j}^{N} e^{-i\,\vec{k}\,\vec{r_l}} \;=\; \sum_{l=1,l\neq j}^{N} \int\limits_{-\infty}^{\infty} \delta(\vec{r}-\vec{r_l})\, e^{-i\,\vec{k}\,\vec{r}}\,\mathrm{d}\,\vec{r}. \tag{2.6}$$

The distribution of the particles, which are located at $\vec{r_j}$ and $\vec{r_l}$, can be interpreted as a continuous distribution that is normalised to the number of involved particles:

$$\rho(\vec{r}) \;=\; N^{-1} \left\langle \sum_{j=1}^{N} \delta(\vec{r}-\vec{r_j}) \right\rangle \tag{2.7}$$

$$\;=\; (N-1)^{-1} \left\langle \sum_{l=1,l\neq j}^{N} \delta(\vec{r}-\vec{r_l}) \right\rangle. \tag{2.8}$$

When interchanging the sum and integration, Equations (2.5) and (2.6) become to

$$\left\langle \sum_{j=1}^{N} e^{i\,\vec{k}\,\vec{r_j}} \right\rangle \;=\; N \int\limits_{-\infty}^{\infty} \rho(\vec{r})\, e^{i\,\vec{k}\,\vec{r}}\,\mathrm{d}\,\vec{r} \tag{2.9}$$

and

$$\left\langle \sum_{l=1,l\neq j}^{N} e^{-i\,\vec{k}\,\vec{r_l}} \right\rangle \;=\; (N-1) \int\limits_{-\infty}^{\infty} \rho(\vec{r})\, e^{-i\,\vec{k}\,\vec{r}}\,\mathrm{d}\,\vec{r}, \tag{2.10}$$

respectively.

Inserting the information from Equations (2.4), (2.9) and (2.10) into (2.3) leads to

$$\boxed{\frac{\mathrm{d}^2 U}{\mathrm{d}\,\omega\,\mathrm{d}\,\Omega} = \left(\frac{\mathrm{d}^2 U}{\mathrm{d}\,\omega\,\mathrm{d}\,\Omega}\right)_1 \left(N + N\,(N-1) \left| \int_{-\infty}^{\infty} \rho(\vec{r})\, e^{-i\,\vec{k}\,\vec{r}}\,\mathrm{d}\,\vec{r} \right|^2 \right).} \tag{2.11}$$

The first summand expresses the incoherent emission ($\propto N$), whereas the second refers to the coherent emission, which is proportional to N^2 as well as to the three-dimensional form factor, the Fourier transform of the normalised charge distribution, $\rho(\vec{r})$, [66]:

$$F(\omega, \Omega) := \int_{-\infty}^{\infty} \rho(\vec{r})\, e^{-i\,\frac{\omega}{c}\,\vec{n}\,\vec{r}}\,\mathrm{d}\,\vec{r} \tag{2.12}$$

The wave vector, $\vec{k}$, was substituted by $\vec{k} = \frac{\omega}{c}\,\vec{n}$ in order to emphasise the dependency on the angular frequency, ω.

Coherent fraction The assessment of electron bunch parameters from the coherent emission is possible using the form factor, $F = F(\omega, \Omega)$, a complex number with an absolute value, $|F| \in [0, 1]$. Since the longitudinal profile of the charge distribution is of particular interest, the longitudinal component, $|F_{\mathrm{long}}|$, is separated from the transverse component in the three-dimensional form factor, where correlations between the longitudinal and transverse planes are disregarded. The information on F_{trans}, as well as on the charge, $Q = N\,q_e$, have to be determined by dedicated measurements [66].

$$F(\omega, \Omega) \;=\; F_{\mathrm{long}}(\omega, \Omega)\, F_{\mathrm{trans}}(\omega, \Omega). \tag{2.13}$$

While the limit $|F_{\mathrm{long}}(\omega \to 0)| = 1$, the absolute value of the form factor increases with decreasing bunch length, l_{b}, for $\omega \neq 0$. The coherent emission is strongly suppressed for $\omega \gg 2\pi l_{\mathrm{b}}/c$, or wavelengths shorter than the bunch length. In other words, the short-wavelength cut off for coherent emission is shifted towards shorter wavelengths with decreasing bunch length. At a fixed bunch length, the coherently emitted fraction rises with increasing wavelength. Examples of form factors for bunches of different lengths are depicted in Figure 4.1 in chapter 4.

A wavelength-integrated measurement of the emitted energy, allowing the estimation of the bunch length, is employed, e. g. at the FLASH facility (cf. appendix A), in bunch compression monitors (BCMs). The detected signal amplitude is inversely proportional to the bunch length. The spectral bandwidth of the instrument sets the detectable range in bunch length [66].

The lack of information about the current profile is mitigated via the measurement of the spectral slope of $|F_{\mathrm{long}}(\omega)|$ in a broad wavelength range. When considering, for instance, Gaussian envelopes of the current profile in the time domain, the global spectral slope of the form factor is unique for a bunch length, even without knowledge of the absolute value.

Since such an assumption is not justified in many cases, the additional knowledge of the amplitude of the form factor, i. e. the irradiated spectral energy and bunch charge, is required in order to gain information on substructures and changes in the current profile that can occur by altering the bunch compression.

The full information on the normalised current profile in the time domain is included in

$$F(\omega) = |F(\omega)|\ e^{i\,\varphi(\omega)}, \tag{2.14}$$

but only $|F(\omega)|$ is experimentally accessible. The spectral phase, $\varphi(\omega)$, cannot be acquired by standard intensity spectroscopy. Hence, it is not possible to unambiguously retrieve the original time-domain profile.

Mathematical methods, that are often misleadingly entitled as *phase retrieval*, can be employed to access a likely phase and a likely time-domain profile within limitations imposed by the approach itself [69] and the method. Examples are the *Kramers-Kronig relation* [8] and iterative processes based on consecutive Fourier transforms between time and frequency domain [70–72, and the references cited therein]. Studies at the FLASH facility indicate that the results are in agreement with time-domain measurements with the TDS [4, 9, 73].

Although phase-sensitive spectral detection techniques, such as frequency-resolved optical gating (FROG) [74], exist and are widely used in laser physics, the limited spectral bandwidth and high intensity demands due to a non-linear process in an optically active medium prevent these techniques to be employed for the diagnosis of low-charge and short electron bunches.

Incoherent fraction The analysis of the statistical fluctuation of the spectrum is applied to the incoherent fraction of the spectrum [75–77]. For bunches yielding a Gaussian current profile with $\sigma \approx 10\,\mu\mathrm{m}$ and without substructures, the wavelength regime of the visible light, extended to the near-UV and -IR, can be considered as incoherent. The subsequent treatment follows [75] and [77].

In the time domain, the electric field of the emitted incoherent radiation can be treated as the product of the current profile, $I(t)$, and a stochastic contribution, $p(t)$, that is due to the finite number of emitting particles.

The fluctuation of the Fourier transform of the emitted spectrum, σ_Γ, carries the information of the autocorrelation of the current profile. With the Fourier transform

$$\Gamma(\tau) = \int_{-\infty}^{\infty} \frac{\mathrm{d}\,U}{\mathrm{d}\,\omega}\, e^{-i\,\omega\,\tau}\,\mathrm{d}\,\omega, \tag{2.15}$$

of the spectral energy density, $\frac{\mathrm{d}\,U}{\mathrm{d}\,\omega}$, the statistical fluctuations can be written as

$$\begin{aligned}\sigma_\Gamma(\tau) &= \left\langle |\Gamma(\tau)|^2 \right\rangle - \left| \langle \Gamma(\tau) \rangle \right|^2 \\ &= p^\star \int_{-\infty}^{\infty} I(t)\, I(t-\tau)\,\mathrm{d}\,t.\end{aligned} \tag{2.16}$$

The factor $p^\star$ accounts for the autocorrelation of the stochastic contribution [75].

2.3 Transition radiation of relativistic electron bunches

Transition radiation occurs when a charged particle passes the interface between media with different electromagnetic characteristics. The properties of the Coulomb field of a charged particle at relativistic velocities with $\gamma \gg 1$ correspond to the material through which the particle propagates and are subject to adjustments at a material transition. The adjustments in Maxwell's equations correspond to the emission of transition radiation with properties that depend on the particle properties such as velocity, mass and charge as well as on the dielectric permittivity and permeability of the involved media [13].

The theory of transition radiation was described by Ginzburg and Frank in 1945 and reviewed in [78]. The subsequent short introduction is based on the publications [9, 13] and [79], where the reader can find further details.

The spectral energy density of transition radiation of a single electron with $\gamma \gg 1$ can be described by the formula found by Ginzburg and Frank

$$\left(\frac{\mathrm{d}^2 U}{\mathrm{d}\,\omega\,\mathrm{d}\,\Omega}\right)_{\mathrm{GF}} = \frac{e^2}{4\pi^3 \varepsilon_0 c} \frac{\beta^2 \sin^2(\Theta)}{(1-\beta^2\cos^2(\Theta))^2}, \tag{2.17}$$

that is valid for

- the transition from a medium with refractive index $n = 1$ to a medium with $n = \infty$,
- frequencies ω far below the plasma frequency, ω_p, of the boundary material, that are
- emitted into the backward hemisphere and are
- observed in the far field, i. e. in a large distance from the boundary.
- The boundary yields an infinite transverse extension and
- a perfect reflectivity.

In short, transition radiation following eqn. (2.17) has the following key properties:

1. the angular distribution yields zero at $\Theta = 0$ and a maximum at $\Theta = \gamma^{-1}$
2. the total intensity scales with $\ln(\gamma)$
3. the spectral intensity is independent of ω
4. the polarisation is radially pointing from the centre to the outside

A "real" transition radiation emitter, namely a target made of e. g. aluminium or silicon in the beam pipe of an accelerator, yields a finite transverse extension (cf. appendix A.3) and the emitted radiation does not, especially for multi-100 MeV electron beams, reach the far field at the position of the first object that causes diffraction [13].

Equation (2.17) can now be modified in order to cope with finite circular screens and the near field. Whereas the former is expressed by the Bessel function of the first kind, J_1, and the second-kind modified Bessel function, K_1 [68], the latter involves the second order approximation of the distance between a source point and a point on the observation plane and delivers an additional phase term, $e^{i\omega\rho^2/(2c\,d_{\mathrm{ref}})}$ [66, 79].

$$\frac{\mathrm{d}^2 U}{\mathrm{d}\,\omega\,\mathrm{d}\,\Omega} = \frac{e^2\,\omega^4}{4\pi^3\varepsilon_0 c^5 \beta^4 \gamma^2} \left| \int_0^{r_\mathrm{s}} J_1\left(\frac{\omega\rho\sin(\Theta)}{c}\right) K_1\left(\frac{\omega\rho}{c\beta\gamma}\right) e^{i\omega\rho^2/(2c\,d_{\mathrm{ref}})}\,\rho\,\mathrm{d}\,\rho \right|^2 . \tag{2.18}$$

Here, the measure d_{ref} is the distance between an observation point and the centre of a circular transition radiation emitter of radius, r_s. The distance between a point on the source plane and its centre is given by ρ. The centre is considered to be the point where the electron hits the interface [13] and to coincide with the centre of the physical target.

The consideration of the transverse size of the TR emitter, as well as near field diffraction leads to modifications of the spectrum and the angular intensity distribution [79–81]. For instance, the finite extension of the transition radiation screens suppresses the emission of long wavelengths, i. e. for λ approaching r_s. The near-field treatment reveals a wavelength-dependent angular distribution. The far field approximation following Ginzburg and Frank, eqn. (2.17), is valid in the case $d_{\mathrm{ref}} \gg \gamma^2\lambda$ [81]. Figure 2.2 qualitatively compares the

influence of the wavelength and the observation distance on the angular distributions of transition radiation as given by formula (2.18).

The expression (2.18) can now be regarded as the single-particle contribution in Formula (2.11) in the previous section. A quantitative assessment of coherent transition radiation for the problem of this thesis can be found in chapter 4.

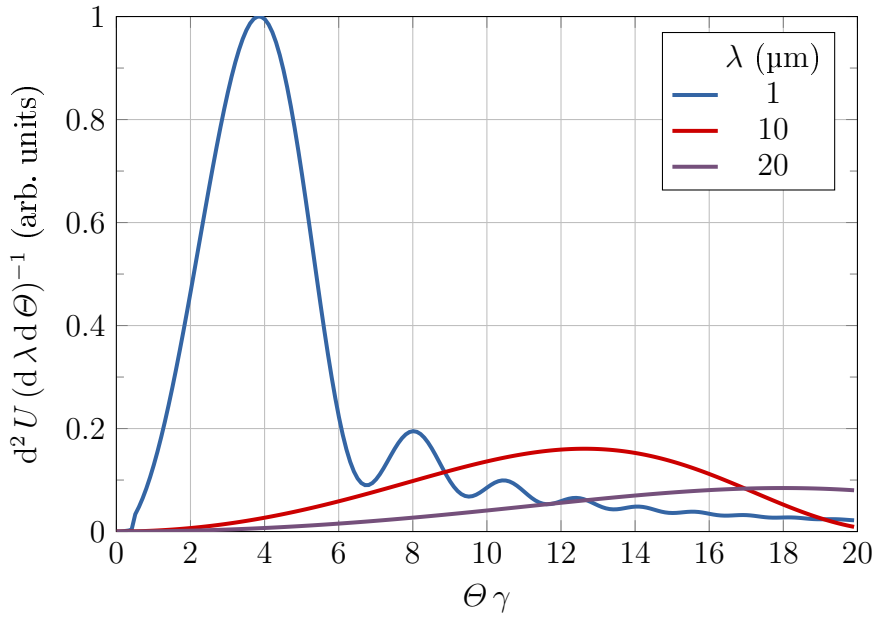

(a) wavelength scan in the near field ($d_{\mathrm{ref}} = 0.045\,\mathrm{m}$)

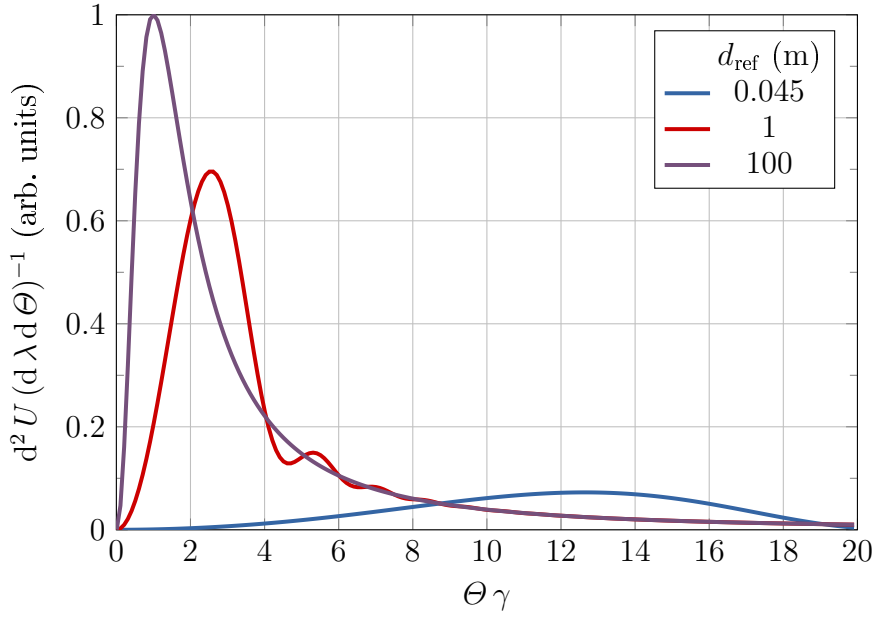

(b) distance scan for $\lambda = 10\,\mu\mathrm{m}$

Figure 2.2: Normalised angular distributions of transition radiation following eqn. (2.18) for $\gamma = 1000$ and a circular TR screen with $r_{\mathrm{s}} = 20\,\mathrm{mm}$ for (*a*) three wavelengths obverved in the distance $d_{\mathrm{ref}} = 0.045\,\mathrm{m}$, i. e. in the near field. The setup at the FLASH facility (cf. appendix A) yields the first limiting aperture at that distance. (*b*) The distributions for three distances, d_{ref}, visualise near field effects at $\lambda = 10\,\mu\mathrm{m}$. The trace for $d_{\mathrm{ref}} = 100\,\mathrm{m}$ can be considered as the far field.

3 Spectroscopy of infrared radiation

The spectroscopy of light in the infrared regime is a fundamental technique in the investigation of a large variety of properties. For example, the spectral analysis of absorption properties allows the determination of the composition of a sample based on characteristic spectral lines of the atoms, molecules and complex compounds [82]. This feature is not only utilised in chemistry and material science, but also in astronomy for the investigation of galaxies with observatories operated in the stratosphere and in space [83, 84].

The infrared (IR) regime of the electro-magnetic spectrum is often defined as the wavelength range beginning with the *near-infrared* at 0.78 µm, which is also considered as the upper limit of the spectrum visible to the human eye [85]. The *intermediate* or *mid-IR* regime ranges from 3 µm to 25 µm, followed by the *far-infrared* from 25 µm to 1000 µm [82, 86].

3.1 Dispersive elements

The purpose of a spectrometer is the disassembly of incident polychromatic light into its wavelength composition. The spectral sorting is carried out either by diffraction at regularly arranged structures, i. e. gratings, or by dispersion by a wavelength-dependent refractive index of an optically transparent material.

Dispersion is commonly defined as the dependency of the phase velocity of a light wave, v_p, on the angular frequency: $v_p(\omega) = c\,n(\omega)^{-1}$ [86]. In this thesis, the affix "dispersion" is also used to express the dependency of a quantity on the wavelength, e. g. the *angular dispersion*, $\mathrm{d}\theta/\mathrm{d}\lambda$, which is introduced in section 3.1.3.

3.1.1 Gratings

Gratings are arrangements of regular grooves, edges or apertures [85]. Considering a regularly grooved surface of perfect reflectivity, a reflection grating, the interference of the partial waves from each of the grooves with spacing, d_g, leads to a periodic wavelength-dependent angular distribution of the intensity. Principal maxima occur at

$$\sin(\alpha) - \sin(\beta) = m\,\lambda\,d_g^{-1}, \tag{3.1}$$

with the angle of incidence, α, the angle of the reflected wave, β, wavelength, λ, and diffraction order, m [85]. The zeroth order, $m = 0$, is equal to the specular reflection according to the *law of reflection* [80], $\alpha = \beta$, whereas the light is sorted by wavelength beginning with $|m| > 1$.

A grating, as depicted in Figure 3.1a, reflects most of the light intensity into the zeroth order, $m = 0$. An arrangement of sawtooth-like facets in *blazed gratings* (see Figure 3.1b) is used to increase the intensity in the dispersive orders, $m \neq 0$. The facets are tilted with respect to the normal of incidence by the blaze angle, θ_b.

The reflection depends on the angle towards the individual facet surface normals, whereas diffraction still occurs in dependency of the groove spacing, d_g, the angle of incidence, α, and the exit angle, β. The choice of a blaze angle, θ_b, for which the diffraction maximum of a certain wavelength coincide with the specular reflection, enables the enhancement of the intensity which is concentrated in the desired diffraction order [85].

3.1.2 Prisms

Prisms are samples of a transparent material, whose front and exit surfaces are not parallel to each other [85]. Figure 3.2a schematically depicts a prism geometry with the nomenclature used in this thesis.

The *law of refraction* or *Snell's law*,

$$\tilde{n_1}\,\sin(\alpha) = \tilde{n_2}\,\sin(\beta), \tag{3.2}$$

describes the rotation of the angle of incidence, α_1, at the transition from one material with refractive index $\tilde{n_1}$ to β_1 in another material with $\tilde{n_2}$ [80].

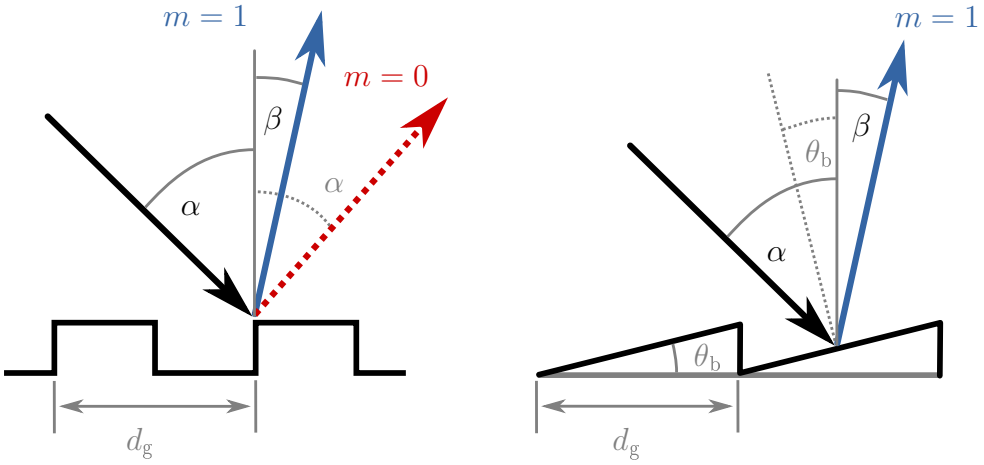

(a) reflection grating (b) blazed grating

Figure 3.1: Geometries of a grating with rectangular grooves (*left*) and a blazed grating (*right*). The formula (3.1) is valid for both arrangements.

Since the refractive index, $\tilde{n} = \tilde{n}(\lambda)$, is wavelength-dependent, the deflection angle, θ, also depends on the wavelength, λ. Consequently, a polychromatic light beam is dispersed.

3.1.3 Angular and linear dispersion

The angular dispersion is the evolution of the total deflection angle with the wavelength, $\mathrm{d}\theta/\mathrm{d}\lambda$ and $\mathrm{d}\beta/\mathrm{d}\lambda$ for a prism (Fig. 3.2a) and a grating (Fig. 3.1) respectively.

Regarding a prism, as presented in Figure 3.2, the angular dispersion can be described by the relation

$$\frac{\mathrm{d}\,\theta}{\mathrm{d}\,\lambda} = \frac{\mathrm{d}}{\mathrm{d}\,\lambda}\left[\alpha_1 + \alpha_2(\lambda) - \epsilon\right] \tag{3.3}$$

$$= \frac{\mathrm{d}}{\mathrm{d}\,\lambda}\left[\alpha_1 - \epsilon - \arcsin\left(\sin(\epsilon)\sqrt{\frac{n_2(\lambda)^2}{n_1(\lambda)^2} - \sin^2(\alpha_1)} - \cos(\epsilon)\sin(\alpha_1)\right)\right]. \tag{3.4}$$

In order to transform the angular dependency into a position dependency on the detector plane, a focusing element follows the dispersive stage. The

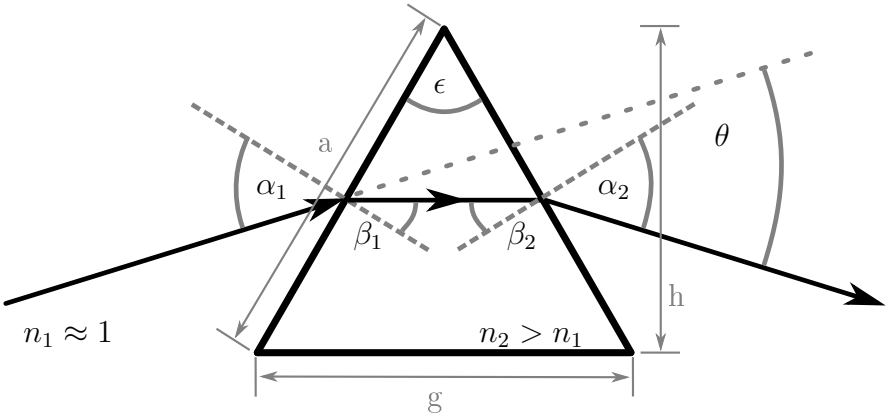

(a) prism parameters

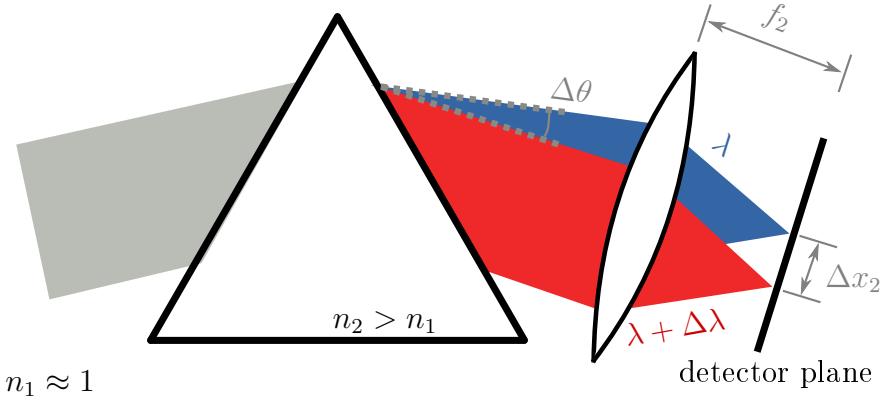

(b) linear dispersion

Figure 3.2: (a) Definitions of the prism parameters used in this monograph. By convention, Greek letters are assigned to angles, whereas distances and length measures are labelled with Latin letters. (b) Illustration of the linear dispersion in the detector plane, Δx_2, following the treatment in [86].

influence of the focal length of the focusing element, f_2, is considered by the definition of the linear dispersion,

$$\Delta x_2 \;=\; f_2 \,\tan(\Delta\theta) \;\approx\; f_2\,\Delta\theta = \; f_2\,\frac{\mathrm{d}\,\theta}{\mathrm{d}\,\lambda}\,\Delta\lambda \;=\; \frac{\mathrm{d}\,x}{\mathrm{d}\,\lambda}\,\Delta\lambda, \tag{3.5}$$

where $\Delta\lambda$ is the wavelength interval of interest [86]. The linear dispersion represents the wavelength distribution in the detector plane and is consequently a direct measure of the dispersion of a spectrometer.

3.2 Imaging and spectral resolution

The spectral resolution of a spectrometer is predominantly defined by the dispersion properties and the imaging system. The latter defines the transverse size of the focus in the detector plane, which is fundamentally limited by diffraction [86]. Envisaging an imaging system as depicted in Figure 3.3a, an entrance aperture of a given width in the dispersive plane, b, is imaged by two focusing elements onto the detector plane.

The *Rayleigh criterion* defines the resolution of a spectrometer [86]. Two adjacent spectral lines are considered to be resolved, if the principal maximum of the intensity distribution of a line with $\lambda + \Delta\lambda$ coincides with the first minimum of the spectral line with wavelength λ - Figure 3.3. Utilising the *Fraunhofer approximation* for the far field regime, the sum (*grey*) of the two intensity distributions (*blue* and *red*), which are just resolved, is $\approx 0.8\,I_0^*$ at $x_2 = \pm\, f_2 \frac{\lambda}{a_{\mathrm{lim}}}$ (cf. Figure 3.3b). The intensity distribution behind a one-dimensional aperture of width a_{lim} is described by

$$I^*(\phi) \;\approx\; I_0^* \left(\frac{\sin\left(a_{\mathrm{lim}}\,\pi\,\phi\,\lambda^{-1}\right)}{a_{\mathrm{lim}}\,\pi\,\phi\,\lambda^{-1}} \right)^2. \tag{3.6}$$

The geometric divergence, $\phi = \frac{x_2}{f_2}$, allows the definition of a diffraction-limited transverse size, w_2:

$$w_2 \;=\; 2\,\phi\,f_2 \;=\; f_2\,\frac{2\,\lambda}{a_{\mathrm{lim}}}. \tag{3.7}$$

Here, the size of the focus in the detector plane is defined as the distance between the first minima surrounding the principal maximum, which are located at $x_2 = \pm\, f_2 \frac{\lambda}{a_{\mathrm{lim}}}$ [80, 86].

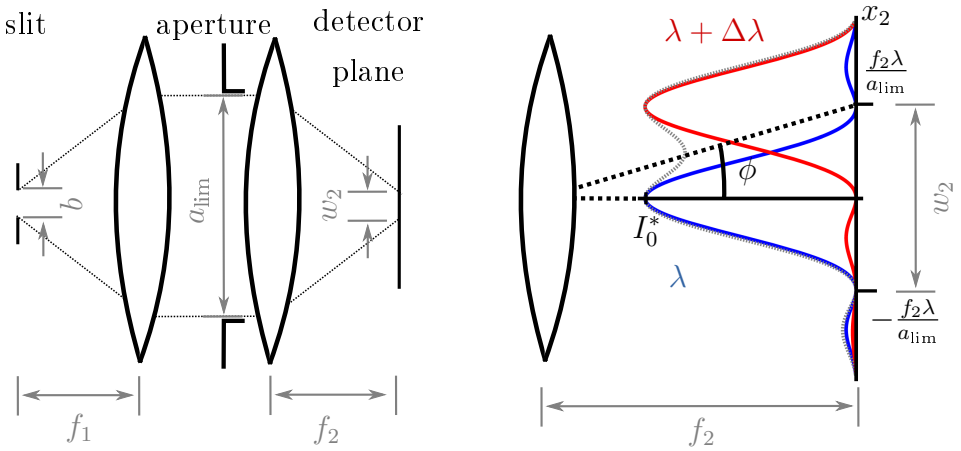

(a) imaging system (b) diffraction limit

Figure 3.3: Illustration of an imaging system (a) and the resulting spectral resolution limit (*Rayleigh criterion*) of a spectrometer, (b). The depictions are adapted from [86].

The optical arrangement in Fig. 3.3a images the entrance aperture of finite width, b, onto the detector plane. This image yields a width $b_2 = M\,b$, where the optical magnification, M, is given by the focal lengths of the two lenses, $M = f_2\,f_1^{-1}$. The width of the slit image on the detector plane, b_2, has to be considered additionally to the diffraction limit introduced above. The distance between two resolved lines, Δx_2, has to be

$$\begin{aligned} \Delta x_2 &\geq f_2 \frac{\lambda}{a_{\mathrm{lim}}} + b_2 \\ &\geq f_2 \frac{\lambda}{a_{\mathrm{lim}}} + b\,M, \end{aligned} \tag{3.8}$$

which translates, considering the definition of the linear dispersion in Equation (3.5), into an expression for the narrowest spectral line, that can be resolved [86]:

$$\begin{aligned} \Delta\lambda &= \frac{\Delta x_2}{f_2} \left(\frac{\mathrm{d}\,\theta}{\mathrm{d}\,\lambda}\right)^{-1} \\ &\geq \left(\frac{\lambda}{a_{\mathrm{lim}}} + \frac{b}{f_1}\right) \left(\frac{\mathrm{d}\,\theta}{\mathrm{d}\,\lambda}\right)^{-1}. \end{aligned} \tag{3.9}$$

For an entrance aperture of infinitesimal width, $b \to 0$, the diffraction-limited resolving power, valid for prisms and gratings, can be written as

$$\left|\frac{\lambda}{\Delta\lambda}\right| \leq a_{\mathrm{lim}} \frac{\mathrm{d}\,\theta}{\mathrm{d}\,\lambda}. \tag{3.10}$$

3.3 Comparison of gratings and prisms

The choice of a dispersive element, which is adequate to the specific spectrometric problem, involves attention to the angular dispersion, spectral resolving power, distortions in the dispersion process and the efficiency regarding the intensity distribution of the dispersed radiation.

The **angular dispersion** is, besides the angle of incidence, determined by the groove spacing, d_{g}, and the dispersion, $\mathrm{d}\,n/\mathrm{d}\,\lambda$, for a grating and a prism respectively. In contrast to gratings, the monotonic dispersion of a prism, which is in most cases not linear with the wavelength, does not suffer from higher orders and allows the unambiguous coverage of more than a factor of two in wavelength.

The **spectral resolution** is determined by the evolution of the linear dispersion, the slit image on the detector and diffraction effects by the limiting aperture, a_{lim}. The diffraction-limited resolving power (cf. Equation 3.10) of a prism is determined by the base length, g, apex angle, ϵ, and the distribution of the refractive index:

$$\left|\frac{\lambda}{\Delta\lambda}\right| \leq \frac{g}{2\,\sin(\epsilon\,/\,2)} \frac{\mathrm{d}\,\theta}{\mathrm{d}\,\lambda}. \tag{3.11}$$

For gratings, the limit is given by the diffraction order, m, and the number of illuminated grating grooves, N_{g} [86]:

$$\left|\frac{\lambda}{\Delta\lambda}\right| \leq m\,N_{\mathrm{g}}. \tag{3.12}$$

The **efficiency** is the intensity ratio of the dispersed radiation to the incident radiation at a given wavelength [66]. Besides the reflectance of the grating material, angle of incidence and the blaze angle, the groove distance, d_{g}, and the number of illuminated grooves define the angular width of the dispersed light in a given diffraction order [86] and thus, the efficiency of a grating. Recent studies on reflection gratings for infrared wavelengths [66, 87] suggested

that a narrow interval allows dispersion with a high efficiency. As an example for $\alpha = 19\,\mathrm{deg}$ and $\theta_b = 26.7\,\mathrm{deg}$, the interval

$$0.72 \leq \lambda\, d_\mathrm{g}^{-1} \leq 1.32$$

yields a high efficiency in the first diffraction order, $m = 1$, for the polarisation perpendicular to the grating grooves. Considering e. g. $d_\mathrm{g} = 15\,\mu\mathrm{m}$ ($\approx 67\,\mathrm{lines\,mm^{-1}}$), the interval between 10.8 µm and 19.8 µm can be covered with high efficiency [87].

Prisms, on the other hand, yield absorption in the optical material and reflective losses at the surfaces that cannot be completely avoided. The efficiency of prisms is in almost all cases lower than for gratings [88]. Thus, the prism material has to be carefully chosen for the wavelength range of interest. Section 3.4 presents various IR-compatible materials.

Distortions in the dispersion process can also limit the spectrometer resolution.

For example, a non-uniform distribution of the groove spacing, d_g, along the grating can lead to undesired diffraction maxima, so-called *grating ghosts* [86].

Under certain conditions, prisms suffer from total internal reflection. Above the critical angle, $\beta_\mathrm{crit} = \arcsin\left(n^{-1}\right)$, almost no intensity is transmitted at the transition from the prism material ($n > 1$) into air ($n \approx 1$) [80]. This feature limits the usable range of angle of incidence and apex angle of a prism.

In summary, gratings allow the high-resolution dispersion of light. However, the wavelength range of a high grating efficiency is limited to an interval of up to a factor of two in wavelength. Prisms suffer from absorption in the bulk material. The constraint in suitable materials also limits the achievable angular dispersion, because it is a direct consequence of the material property of the refractive index, n. On the contrary, the monotonic distribution of $n = n(\lambda)$ enables the continuous and unambiguous coverage of a broad wavelength range (see e.g. [89]), which is, within certain limits, also tunable due to possible adjustments of the prism angles and arrangements.

3.4 IR materials

The applicability of an optical material for the infrared regime is primarily determined by its complex refractive index, $\tilde{n}(\lambda) = n(\lambda)\ (1 + i\kappa(\lambda))$ [80]. The refractive index sets the dispersive properties such as the angular dispersion and reflective losses at the material surfaces following the formulae named for Fresnel [80].

The transmission of the electric field of a wave polarised perpendicularly to the optical plane (s polarisation) and for the polarisation parallel to the optical plane (p polarisation) are given by

$$\mathfrak{T}^*_{\mathrm{s}} = \frac{2\,\tilde{n}_1\,\cos(\alpha_1)}{\tilde{n}_1\,\cos(\alpha_1) + \tilde{n}_2 \frac{\mu_1}{\mu_2}\,\cos(\beta_1)}, \tag{3.13}$$

$$\mathfrak{T}^*_{\mathrm{p}} = \frac{2\,\tilde{n}_1\,\cos(\alpha_1)}{\tilde{n}_2 \frac{\mu_1}{\mu_2}\,\cos(\alpha_1) + \tilde{n}_1\,\cos(\beta_1)}, \tag{3.14}$$

with the complex refractive indices, $\tilde{n}_{1,2}$, the magnetic permeabilities, $\mu_{1,2}$, and the angles, α_1 and β_1, between the propagation direction of the wave and the surface normal in the respective media [80, 85].

The transmission factor regarding the transmitted intensity, $I^*_{\mathrm{transmitted}}$, with respect to an incident intensity, I^*_{incident}, can now be written as

$$\mathfrak{T} = \frac{I^*_{\mathrm{transmitted}}}{I^*_{\mathrm{incident}}} = \frac{\tilde{n}_2}{\tilde{n}_1}\,\frac{\cos(\beta_1)}{\cos(\alpha_1)}\,\left|\mathfrak{T}^*\right|^2. \tag{3.15}$$

The imaginary part of the complex refractive index causes a wavelength-dependent damping of the electro-magnetic wave in a non-dielectric medium [80]. The *Beer-Lambert law* describes the exponential attenuation of the intensity as a dependency of the material intersection, d, via the absorption coefficient, Υ. The absorption coefficient contains the extinction coefficient, κ, as a property of the material.

$$I^*_{\mathrm{transmitted}} = I^*_{\mathrm{incident}}\,e^{-\Upsilon\,d} = I^*_{\mathrm{incident}}\,e^{-4\,\pi\,\kappa\,n\,d\,\lambda^{-1}} \tag{3.16}$$

Figure 3.5, cited from [93], depicts various IR-compatible materials. Regarding the transmission properties, NaCl, KRS-5, KBr and ZnSe, among others, are suitable materials for mid-IR wavelengths.

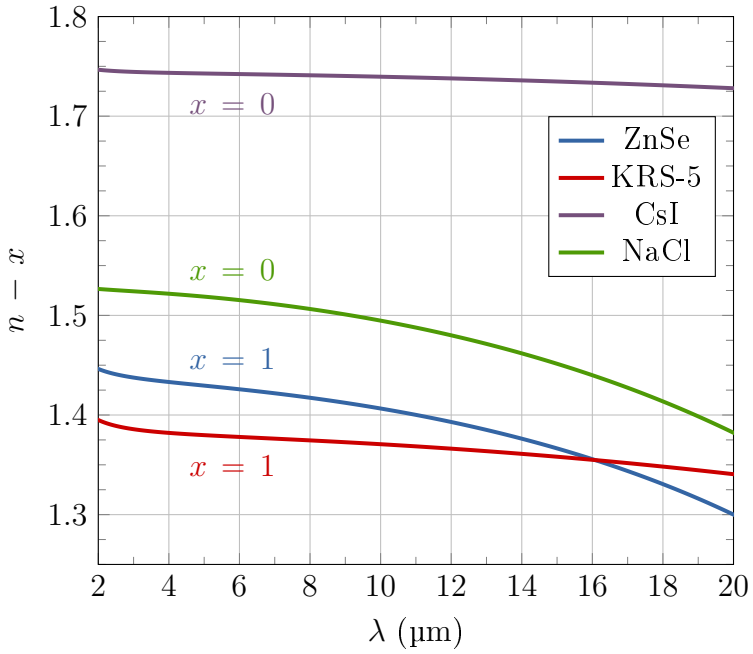

Figure 3.4: Real part n of the refractive index for IR-compatible materials following [90–92]. The traces for ZnSe and KRS-5 have been shifted by x for a better visualisation.

3.5 Detectors

Detectors for infrared radiation are based on several physical processes. The synopsis in the following is based on the references [93] and [94], where the reader can also find a detailed treatment of the detection mechanisms and characteristics.

3.5.1 Thermal detectors

The irradiated thermal power of incident infrared radiation changes the electric and mechanical properties of appropriate materials. In **thermoresistive detectors** such as bolometers, the temperature change of an optical absorber is electrically detected based on the temperature-dependent conductivity of e. g. a thermistor [95]. Arrays of microbolometers are utilisied in infrared cameras. The thermal time constant is on the order of 1 ms [96]. Recent developments are based on the high-temperature superconductor YBaCuO [97].

The thermal load induced by the incident radiation can also lead to the

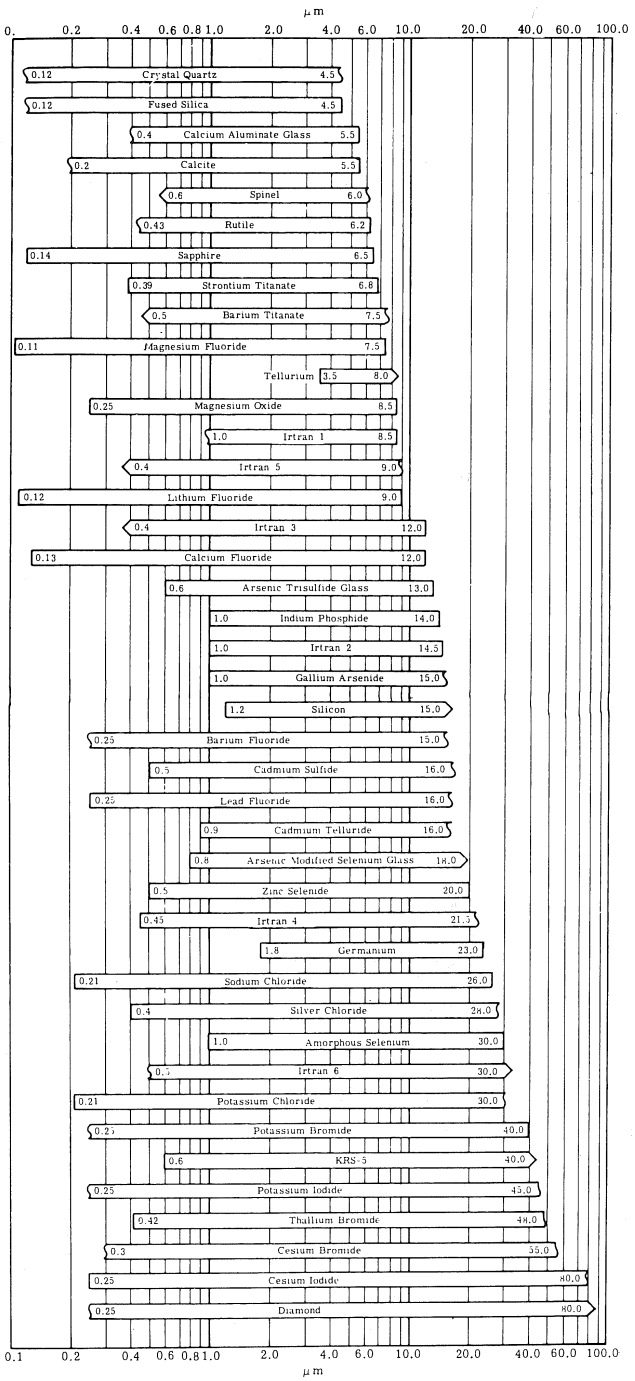

Fig. 7-5. Transmission regions of optical materials (2 mm thickness). The cutoff is defined as 10 percent external transmittance. Irtran 6 is no longer manufactured by the Eastman Kodak Co. Irtran® is a registered trademark of the Eastman Kodak Co.

Figure 3.5: Comparison of the transmission of materials in the infrared regime. Cited from [93, p. 7-17].

expansion of an appropriate material. A Golay cell [98] within a group of **thermopneumatic detectors** utilises a membrane as the absorbing medium and an optical system for the detection of the mechanical deformation.

Furthermore, the dependency of the polarisation density on the temperature variation in a crystal is known as the pyroelectric effect. In **pyroelectric detectors**, the induced change in polarisation is detected via an evoked potential difference [66].

3.5.2 Detectors based on quantum effects

Incident photons can cause a change in the average number of free charge-carriers in semiconductors, which is detected via different techniques. A schematic of the detection mechanism is depicted in Figure 3.6.

Photoconductive (PC) detectors are based on the effect that the induced change in electrical resistance is, disregarding saturation and "sweep-out" effects, proportional to the variation in the quantity of incident photons. The thereby invoked potential difference between the read-out contacts, for a certain bias current, is electrically detected. The charge carrier lifetime, transit time to the read-out contacts and bias current influence the detector performance. The time constants are on the sub-µs scale. Material examples are structures of HgZnTe and HgCdTe, where the latter is often abbreviated to MCT.

In **photoelectromagnetic (PEM) detectors**, infrared photons generate electron-hole pairs at the surface of a semiconductor, which diffuse into the material. A magnetic field separates the charge carriers and generate a potential difference, which is detectable as a voltage [99]. PEM-based detectors are particularly suitable for operation at room temperature and without bias supply and amplifiers. Mercury cadmium telluride and indium antimony structures are utilised in this detector type.

Photovoltaic (PV) detectors as well as photo diodes are based on the generation of electron-hole pairs close to a pn-junction between semiconductors, which lead to a shift of the Fermi level at the junction. In the positively doped region, for example, the photo effect excites an electron to the conduction band, which moves, due to diffusion and drift, towards a position at a lower potential in the n-region (see Fig. 3.6c). Also regarding the correspond-

ing mechanism for a "hole" generated in the n-region close to the junction, the excess in charge carriers alters the energy levels of the valence and conduction band, which is measured as a potential difference, u_{signal}. Aside from InGaAs, PbS and PbSe, HgCdTe is also an example of a possible active material here.

3.5.3 Detectivity and comparison

In order to enable the comparison of various detection techniques, the measure *specific detectivity*, $D^* = D^*(\lambda, f_c, \Delta f)$, has been defined with respect to the wavelength, λ, optical chopping frequency, f_c, noise bandwidth, Δf, and active area of one detector element, A [94, 100].

$$\boxed{D^*(\lambda, f_c, \Delta f) = \frac{\sqrt{A\,\Delta f}}{P_{\text{NEP}}}} \tag{3.17}$$

In general, the noise-equivalent power, P_{NEP}, is the incident radiative power equalling the noise of the detector [101]. It can be seen as the required power, P, to achieve a signal-to-noise ratio, $r_{S/N}$, of unity (cf. formula 5.1).

Background limit The performance limit of an infrared detector is not only set by the active material, bias supply and the consequent chain of read-out electronics. The fluctuation of the background photon flux sets a fundamental detection limit [94]. The Background Limited Infrared Photodetector (BLIP) detectivity is considered as the situation when the fluctuations of the ambient background radiation equals the noise level of the detector system. In this model, the noise-equivalent power is given by

$$P_{\text{NEP}} = \frac{h\,c}{\lambda}\sqrt{\frac{2\,A\,\Phi_{\text{bg}}\,\Delta f}{\eta}} \tag{3.18}$$

with the flux density of background photons, Φ_{bg}, and quantum efficiency, η. The latter is the number of electron-hole pairs generated by an incident photon for quantum effect-based detectors [94].

Consequently, the BLIP detectivity can be written for photovoltaic (PV) detectors as

$$D^*_{\text{PV}} = \frac{\lambda}{h\,c}\sqrt{\frac{\eta}{2\,\Phi_{\text{bg}}}}. \tag{3.19}$$

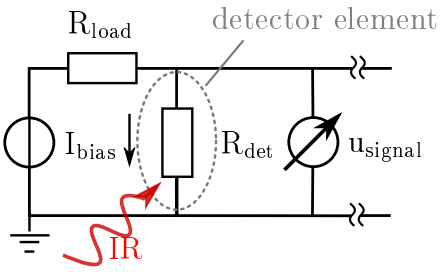

(a) photoconductive detectors: the resistance of the active material depends on the irradiated intensity.

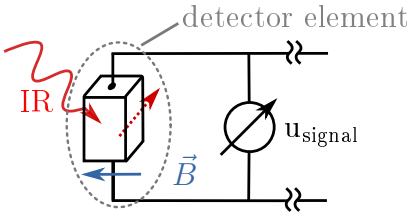

(b) photoelectromagnetic detectors: a magnetic field separates free-charge carriers, which diffuse from the surface into the material.

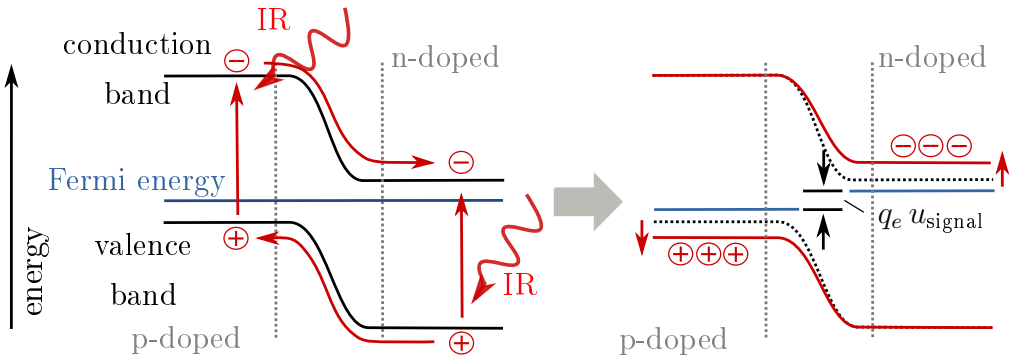

(c) photovoltaic detectors: in the band diagram, photo-induced charge carriers shift the Fermi energy at both sides of the junction and induce a potential difference.

Figure 3.6: Illustration of the operation principles of photoconductive, photovoltaic and photoelectromagnetic detectors. See text for details. The depictions are adapted from [86, 94].

The expression for photoconductive (PC) has to be modified [94, 100] such that

$$D^*_{\mathrm{PC}} = \frac{\lambda}{h\,c}\sqrt{\frac{\eta}{4\,\Phi_{\mathrm{bg}}}}. \tag{3.20}$$

The difference is, following [94], due to the non-correlated generation and recombination processes of free charge-carriers in photoconductive detectors.

Comparison The Figure 2-1 in reference [100], a technical information from the manufacturer Hamamatsu Photonics, compares the specific detectivity of various detection techniques with respect to the BLIP detectivity. The depiction claims that detectors based on e. g. MCT (HgCdTe), InGaAs, PbS and germanium offer an increased detectivity compared to pyroelectric detectors. The photovoltaic detectors based on InGaAs, PbS and germanium are expected to reach detectivities close to the background limit at wavelengths around 2 µm, but yield bandwidths of $(1-2)$ µm. The detectivity of e. g. MCT detectors is apparently strongly dependent on the detector bandwidth: the narrower the bandwidth of the detector is, the higher is the detectivity. Despite the decreased detectivity for MCTs with bandwidths larger than 10 µm, an improvement of the factor $> 10^2$ in D^* with respect to pyroelectric detectors is expected for cryogenic MCT detectors for mid-IR wavelengths. Additionally, MCTs offer a response time on the µs scale, which cannot be offered e. g. by thermoresistive and -pneumatic detectors.

Part II

Experimental setup and measurements

4 Design of the Double-Prism Spectrometer

The main objective of the spectrometer is that it should be able to cope with transition radiation generated using electron beams of femtosecond duration which contain only a few picocoloumbs of charge. The spectrometer has been designed especially for the diagnosis of electron bunches from plasma wakefield acceleration experiments as well as a complement to existing spectrometers at the FLASH facility at DESY in Hamburg, Germany (App. A), a radio frequency (RF) linear accelerator for a free-electron laser (FEL) in the SASE mode [102].

As an example for laser-driven plasma wakefield acceleration (LWFA), the application of the spectrometer at an experiment at the Central Laser Facility at the Rutherford Appleton Laboratory, Chilton, UK [103] is presented in appendix B.

This chapter introduces the boundary conditions set by the electron bunches of interest. Based on these parameters, the key transition radiation parameters and the consequent spectrometer design are presented and justified.

4.1 Design criteria

4.1.1 Electron beam parameters

The electron beam parameter space for the two applications are summarised in Table 4.1, more details can be found in the Appendices A and B. The two key parameters, the bunch duration and the bunch charge are estimated to be below 10 fs full width at half maximum (FWHM) and less than 10 pC respectively.

For the experiment investigating LWFA, the transverse extensions of the electron bunches were estimated from previous experiments [104].

The mentioned requirement in bunch length for the FLASH facility is valid for a dedicated short-pulse operation mode (see e. g. [105]).

Table 4.1: Overview of the electron beam parameters used as design criteria for the transition radiation spectrometer. Please refer to Appendices A and B for details.

parameter	unit	value		
		LWFA	FLASH	
bunch length (FWHM)	µm	< 3		[104], [105]
bunch charge	pC	< 10		[104], [105]
transverse beam size (FWHM)	µm	> 230	> 450	[104], [9]
beam energy	MeV	$500 - 700$	$450 - 1250$	[104], [102]

4.1.2 Transition radiation parameters

The electron beam parameters presented in Table 4.1 determine the characteristics including transverse profile, spectrum and intensity of the generated transition radiation. In order to adapt the spectrometer design to these parameters, analytical and numerical studies have been performed. The code *THzTransport* [106] for MATHEMATICA [107] has been utilised to perform the numerical studies on the expected transition radiation parameters.

Spectral range The requirement for the spectral range is predominantly set by the range of electron bunch lengths that are of interest. Referring to the section 'Frequency-domain methods' in chapter 2, the chosen spectral region of interest is preferably where;

1. the form factor exhibits the largest possible variation for the varying bunch length within the specified range,
2. the form factor approaches unity as the long wavelength limit and
3. substructures in the longitudinal electron beam profile are accessible (short wavelength limit).

The evaluation of Formula (2.12), for the modulus of the longitudinal form factor $|F|$, yields the distributions depicted in Figure 4.1b for the parameters summarised in Table 4.1. The corresponding current profiles, considering a Gaussian electron bunch shape, are depicted in Figure 4.1a. Both figures also show the current profile and form factor for electron bunches with a box-like longitudinal profile in order to illustrate the resulting modulation at short wavelengths.

A significant variation in the form factor is clearly visible in the wavelength range between $(1 - 30)\,\mu\text{m}$. This implies that the mid-infrared regime is the wavelength range of interest for the bunch lengths expected at the two applications.

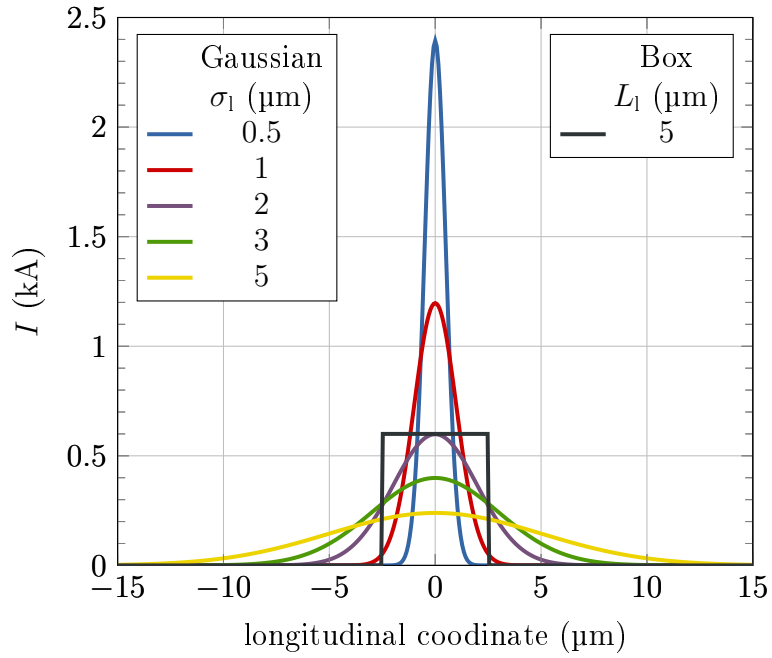

(a) projected current profile

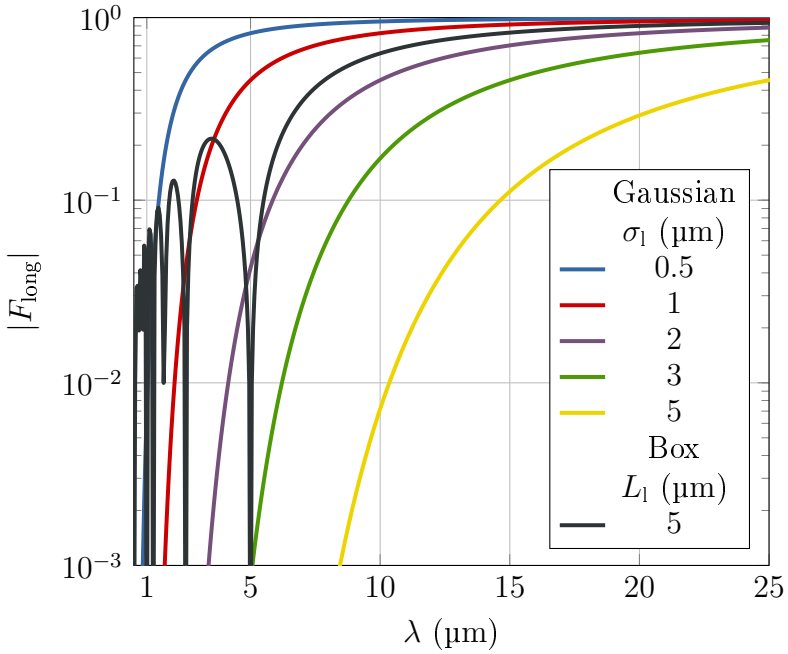

(b) longitudinal form factor

Figure 4.1: Projected longitudinal current profiles and the corresponding form factors of bunches with Gaussian and rectangular box shape, each with a charge of 10 pC.

Intensity range The spectral energy of the transition radiation pulses not only depends on the number of electrons contributing to the emission, but also on the three-dimensional form factor of the electron bunch (cf. chapter 2.3).

In order to estimate the sensitivity requirement of the detector system, numerical studies of the radiated spectra have been performed with *THzTransport*. The transverse radiation profile, spectral energy content and divergence are strongly wavelength-dependent, as is the transport of the radiation with regard to diffraction. A simple optical system introduced in the Appendix C.1 was used to transport the radiation from an electron bunch, containing 10 pC of charge, with Gaussian transversal and longitudinal shape with $\sigma_{\mathrm{trans}} = 100\,\mu\mathrm{m}$ and $\sigma_{\mathrm{long}} = 1\,\mu\mathrm{m}$ respectively.

A single detector element of e. g. a line detector in a spectrometer is exposed to a spectral distribution of limited width and shape, which are determined by the dispersive stage of the spectrometer and the detector geometry. Regarding the distributions shown e. g. in [66, section 4.4], the shape of the spectral distributions on the detector elements was chosen to be Gaussian with a width of $\sigma = 1\,\%$ of the centre wavelength of the individual distribution. The spectral energy density has been integrated in the range of $\pm 4\sigma$ to determine the pulse energy deposited onto a circular detector plane of radius $r = 1\,\mathrm{mm}$.

The spectral energy has been calculated for spectral distributions at distinct wavelengths between 2 µm and 30 µm and the results of this assessment are presented in Figure 4.2. Radiation pulse energies on the nanojoule level are expected.

Repetition rate and radiation pulse duration Superconducting RF accelerators often operate with pulse structures consisting of macro-pulses carrying up to hundreds of radiation pulses [61, 102, 108]. Therefore, the spectrometer data acquisition system has to be able to separate single radiation pulses with a spacing on the microsecond level. As presented in Appendix A, the repetition rate of the linear accelerator of the FLASH FEL facility is 10 Hz, whereas the intra-burst repetition rate is up to 1 MHz in standard operation mode.

The response of both the optically active material and the subsequent electronics is affected by the radiation pulse length and thus, the optical and electronic integration times [66, 94, and section 3.5]. In this application, the

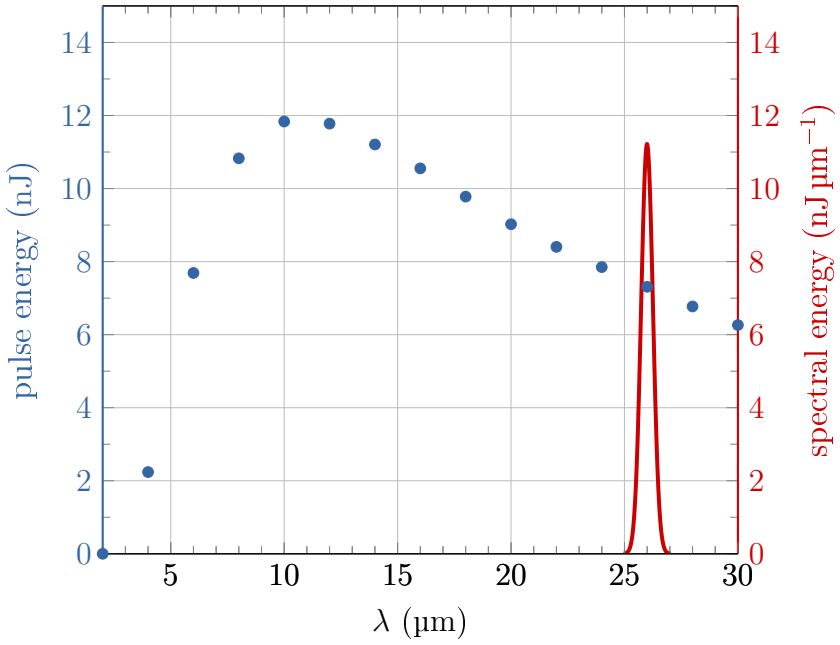

Figure 4.2: Calculated pulse energies of transition radiation (*blue*) emitted by an electron bunch with the parameters $Q = 10\,\mathrm{pC}$, $\sigma_{\mathrm{trans}} = 100\,\mu\mathrm{m}$ and $\sigma_{\mathrm{long}} = 1\,\mu\mathrm{m}$. The energies have been estimated by integration of a Gaussian spectral distribution yielding $\sigma = 1\,\%$ spectral bandwidth. One distribution is exemplarily shown for the centre wavelength $\lambda = 26\,\mu\mathrm{m}$ (*red*).

duration of one radiation pulse observed at the detector plane is determined by the longitudinal current profile and overall duration of the electron bunch and moreover, by the dispersive stage, i. e. the spectral width exposed to the individual detector elements of finite size.

The bandwidth-limited duration of a pulse, that yields a spectral Gaussian distribution with a r.m.s. width of $\sigma = 0.1\,\mu\mathrm{m}$ at $\lambda = 10\,\mu\mathrm{m}$, is approx. 1.47 ps [109]. This pulse duration is short compared to typical read-out time scales (nanoseconds to microseconds).

4.2 Setup of the spectrometer

4.2.1 Detector system

Based on the overview presented in section 3.5, photoconductive mercury cadmium telluride (MCT) detectors have been chosen. The semiconductor-based detection process provides fast optical response and relaxation times with increased sensitivity compared to pyroelectric detectors. The following argument justifies that the detector type and its data acquisition system fulfil the requirements stated previously.

Detector head The commercially available system, manufactured by Infrared Systems Development Corp. [110, 111], consists of a horizontally arranged line of eight 16-element groups, equalling 128 elements. The elements yield an optically active area of 200 µm by 500 µm each, horizontally and vertically respectively. The elements are horizontally separated by inactive regions of 50 µm width. Hence, the total length of the detector line is 31.95 mm.

The detector elements are cooled by liquid nitrogen (LN_2), to a temperature of 77 K for low-noise operation close to the background-limited sensitivity of the detector [94]. The LN_2 dewar has a capacity of 0.7 l, which has been confirmed to be sufficient to operate for at least 8 h without refilling. The temperature is monitored online utilising a temperature diode. The optically sensitive elements are sealed from ambient air using a wedged zinc selenide (ZnSe) window. Details of ZnSe are discussed in section 3.4.

The figure of merit for the sensitivity of an infrared radiation detector is the specific detectivity, D^* (see chapter 3), which essentially enables the comparison of various detection mechanisms. Measured data of the peak specific detectivity, $D^* = D^*(\lambda_p, 1\,\mathrm{kHz}, 1\,\mathrm{Hz})$, for the 128 individual elements have been provided by the manufacturer. The data was acquired using a blackbody radiator with a temperature of 500 K and a chopping frequency of $f_c = 1\,\mathrm{kHz}$, noise bandwidth $\Delta f = 1\,\mathrm{Hz}$ and the wavelength of peak sensitivity λ_p. It should be noted that the data depicted in Figure 4.3 are of limited validity for a quantitative assessment of the detection of short radiation pulses and integration times. The specific detectivity is the subject of further investigation for the radiation pulse properties mentioned above, especially regarding pulse

duration and intensity.

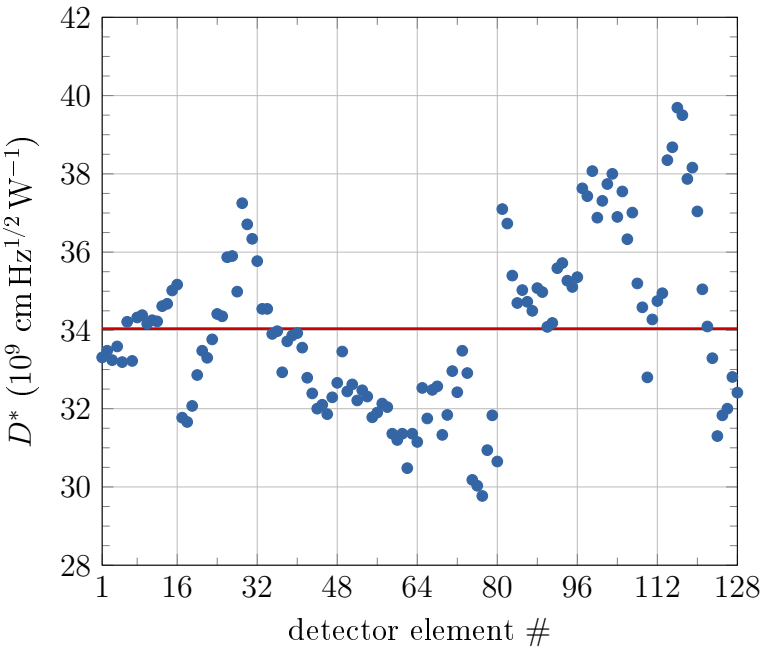

Figure 4.3: Data of the specific detectivity D^* as provided by [110]. The mean value (*red line*) is calculated to be $(34.05 \pm 0.19) \cdot 10^9\,\mathrm{cm\,Hz^{1/2}\,W^{-1}}$. This value is higher by a factor of 10^2 compared to pyroelectric detectors (see section 3.5).

The mean detectivity has been calculated, from the data presented in Figure 4.3, to

$$\overline{D^*\left(\lambda_p, 1\,\mathrm{kHz}, 1\,\mathrm{Hz}\right)} = (34.05 \pm 0.19) \cdot 10^9\,\mathrm{cm\,Hz^{1/2}\,W^{-1}}. \tag{4.1}$$

The spectral detector response is not flat in the design wavelength range. Until a scheduled calibration campaign has been completed, the spectral response is modelled on the basis of data provided by the manufacturer. The data are available for 17 individual elements. The mean value of the available elements (*solid line*), which has been used for the data analysis, and the variation range (*grey area*) are presented in Figure 4.4.

Also referring to chapter 3, the increased sensitivity of the MCT detectors in the wavelength band of interest compared to pyroelectric detectors qualified the system for the use in a spectrometer for low-charge electron bunches.

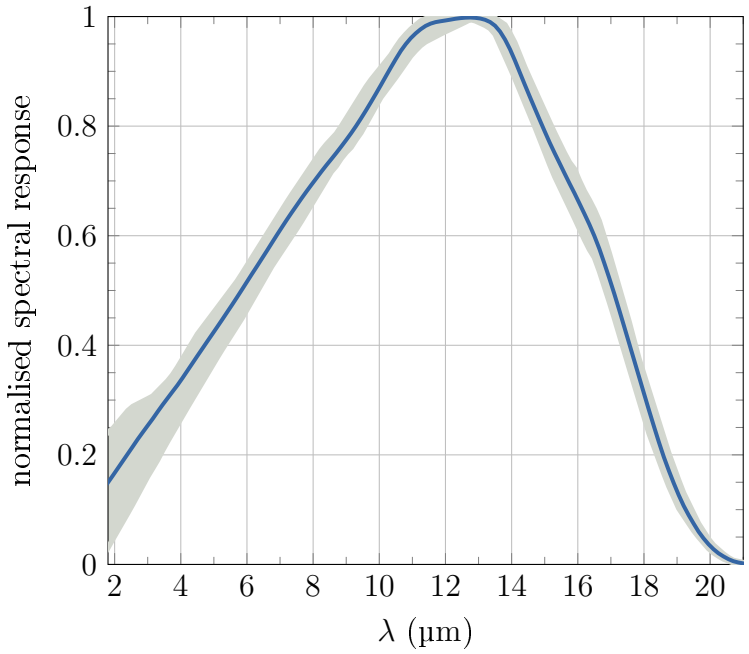

Figure 4.4: Normalised wavelength response of the MCT detector. The mean value of the distributions for the 17 elements provided by the manufacturer is depicted in *blue*, whereas the *grey area* represents the full variation width of the traces of the individual elements.

Electronics The bias supply for the photoconductive MCT elements and the read-out electronics are combined in a data acquisition system. This system provides a digital interface to a personal computer for data storage by a software based on National Instruments LabView [112]. A direct connection to the control system of the FLASH facility was not available during the preparation time of this thesis. Details on the data analysis can be found in section 5.4.

The detector signal, the voltage modulation due to the change in resistance of the detector elements induced by the radiation exposure, is processed by a chain of analogue and digital electronics. A two-stage amplifier, with a bandwidth of $\Delta f = 10\,\mathrm{MHz}$, is followed by a gated boxcar integrator. The circuit is equipped with a remotely-selectable capacitance between 0.25 nF and 4 nF, which allows 16 electronic gain settings [95, 113]. The individual capacitor values (Table 4.2) are divided in two operation modes. The hereby introduced electronic gain factor G is normalised to the minimum gain setting "0" in the *low-gain mode*. During the measurements, the gain value is adjusted such

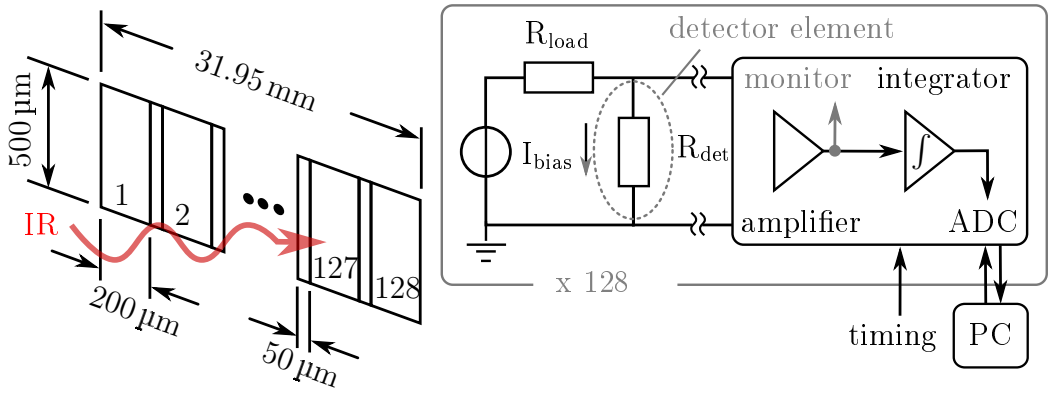

Figure 4.5: (*Left*) Sketch of the detector element geometry. (*Right*) Typical wiring of a photoconductive detector as indicated by the manufacturer of the detector head, [111], and the subsequent analogue and digital electronics chain [110].

that the signal of the detector elements is approximately in the centre of the dynamic range of the ADC (cf. Table 4.3).

The signals from the two-stage amplifier are accessible for each individual elements via output connectors, which enable a monitoring of the signals and the future application of an alternative signal processing chain with direct connection to the control system of the FLASH facility.

Figure 4.6 presents as an example the output signal of the amplifier stage for element 82, which is further processed by the integrator. A gate signal restricts the temporal integration range to a narrow window, typically between 1 µs and 2 µs, to minimise the contribution of adjacent electron bunches in the bunch train to the signal of the bunch of interest. The low duty cycle of $\approx 10^{-5}$ suppresses offset and noise contributions by e. g. ambient thermal radiation. The temporal gate width and position with respect to a timing reference, that is synchronous to the electron bunch train repetition rate, can be adjusted remotely.

The output of the boxcar integrator, which is a DC voltage held until the next trigger signal, is digitised by an analogue to digital converter (ADC) with a resolution of 16 bit within the dynamic range of 0 V to 5 V. The digital signals of the 128 detector elements are transferred via a National Instruments PCI card *DIO-32-HS* to a personal computer and stored for the data analysis.

Table 4.2: Gain settings of the gated integrator of the MCT electronics unit. Details on the electronics can be found in section 4.2.1.

(a) low-gain mode

setting	C_2 (pF)	G
0	4000	1
1	3750	16/15
2	3500	8/7
3	3250	16/13
4	3000	4/3
5	2750	16/11
6	2500	8/5
7	2250	16/9

(b) high-gain mode

setting	C_2 (pF)	G
0	2000	2
1	1750	16/7
2	1500	8/3
3	1250	16/5
4	1000	4
5	750	16/3
6	500	8
7	250	16

The specifications of the read-out system are summarised in Table 4.3.

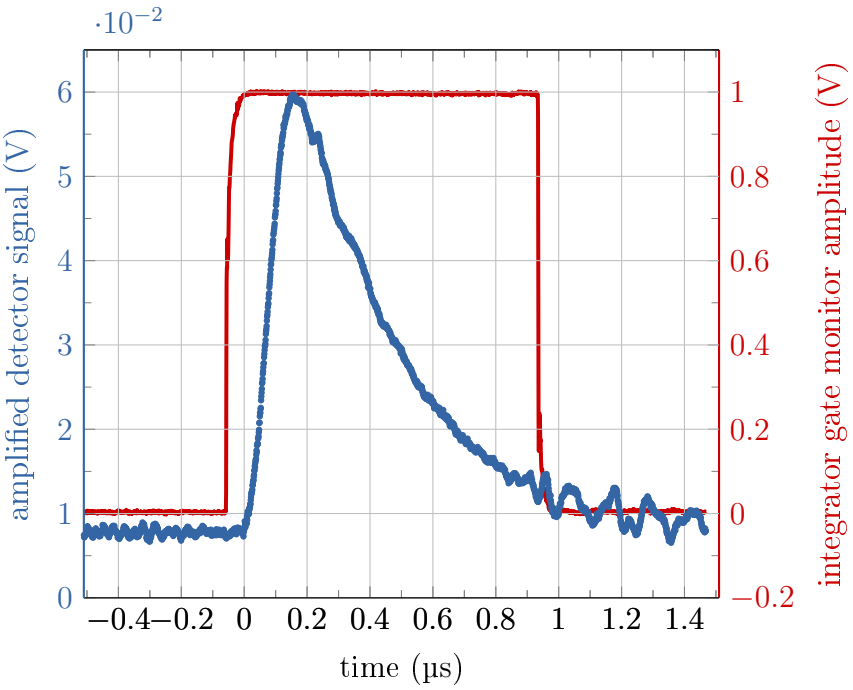

Figure 4.6: A typical voltage signal from the amplification stage of one detector element (*blue*), which is fed into the integrator. The total rise time is approx. 150 ns and the decay time to $1/e$ of the peak signal 340 ns. The adjustable gate pulse (*red*) selects the temporal integration window.

Table 4.3: Summary of the key parameters of the detector system consisting of the head and the electronics provided by Infrared Systems Development Corp. [110]. The values for the bias current and the specific detectivity have been averaged over the 128 elements.

parameter	unit	value
number of elements		128
element height	µm	500
element width	µm	200
width of inactive interspacing	µm	50
bias current (mean)	mA	8.97 ± 0.09
specific detectivity (mean)	$10^9\,\mathrm{cm\,Hz^{1/2}\,W^{-1}}$	34.05 ± 0.19
pre-amplifier analogue bandwidth	MHz	10
integrator gate width	ns	$54 - 5154$
ADC dynamic range	V	$0 - 5$
ADC resolution	bit	16
maximum repetition rate	kHz	50

4.2.2 Dispersive stage

The purpose of the dispersive stage is to disperse the wavelength range of approximately 2 µm to 20 µm onto the detector plane of 31.95 mm width. A prism arrangement was chosen to achieve a continuously dispersed beam without higher orders and the capability of single-shot operation. Due to the complexity and the cost of the detector system, only a single detection stage is available. Similar concepts are being pursued at the Helmholtz-Zentrum Dresden-Rossendorf (HZDR) [114] and LCLS at the Stanford Linear Accelerator Center (SLAC) [89]. The latter system has shown convincing results, but yields with the single-prism arrangement a significant difference in the design compared to the system introduced here. The spectrometer built at HZDR spectrally subdivides the incident light into three spectral bands with individual dispersive stages.

The starting point for the design of a prism spectrometer is the choice of the dispersive material and the prism geometry. The first is determined by the refractive index, n, whereas the latter has to fulfil several constraints, on e. g. the total deflection angle, θ, and the linear dispersion, Δx_2, in the detector plane. The dispersion formulae used in the following are presented in Chapter 3.

Single-prism arrangement

Figure 4.7 presents the distribution of the angular dispersion, $\mathrm{d}\theta/\mathrm{d}\lambda$, and linear dispersion, Δx_2, in the detector plane for various IR-compatible materials, which are discussed in the theory part of this monograph. The latter, which also depends on the imaging system, is included as an illustration of the dispersive power of the dispersive medium.

Referring to sec. 3.1.2, the thallium compound KRS-5 offers the broadest spectral transmission range, but yields a lower angular dispersion in comparison to zinc selenide (ZnSe) and sodium chloride (NaCl). In order to achieve a linear dispersion with KRS-5, which is similar to ZnSe, the focal length f_2 is required to be three times larger than for zinc selenide. Referring to the introduction of the imaging system later in this chapter, an increased focal length f_2 leads to an increase in the preceding focal lengths and in the trans-

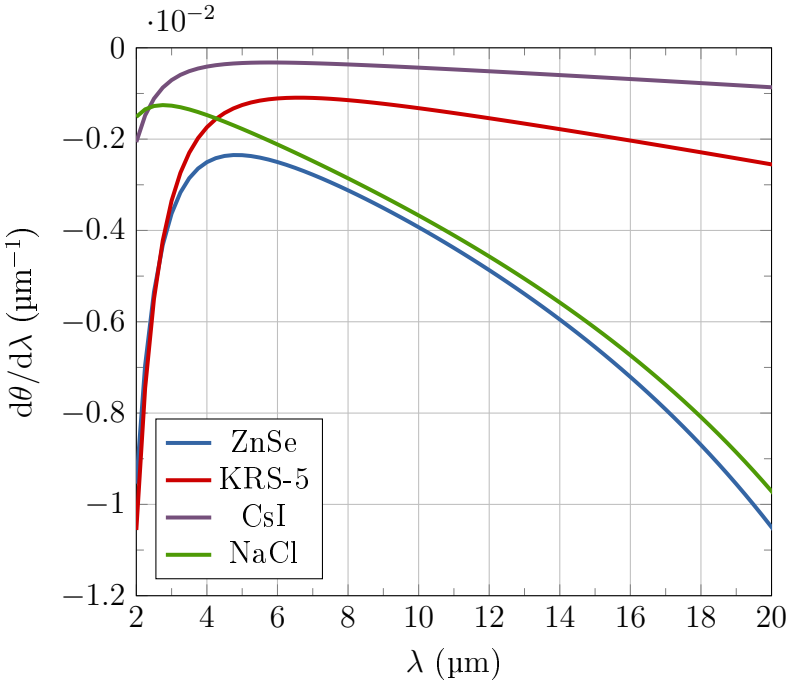

(a) angular dispersion

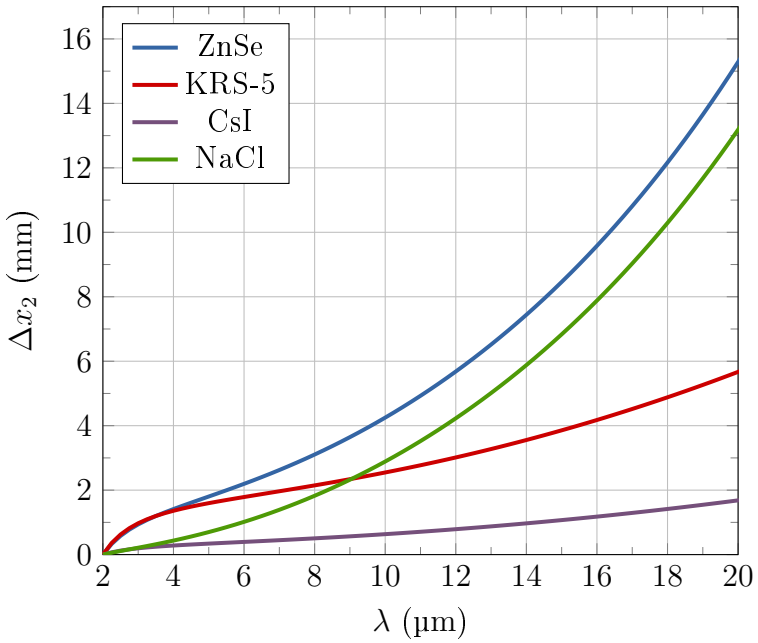

(b) linear dispersion

Figure 4.7: Angular and linear dispersion of various materials for infrared optics. The prism parameters are $\epsilon = 35\,\mathrm{deg}$ and $\alpha_1 = 30\,\mathrm{deg}$. A focal length of $f_2 = 163\,\mathrm{mm}$ has been used for the linear dispersion in the detector plane.

verse beam extension. Although sodium chloride shows suitable parameters in transmission and dispersion, the demands on the handling, e. g. due to the hygroscopic characteristic [115], exclude this material for a system which is intended to be operated in ambient air without special precautions.

Following the comparison in Fig. 4.7, zinc selenide offers the highest dispersive power at a constant focal length, f_2. In combination with a limited, but still sufficient spectral transmission (please refer to chapter 3), ZnSe was chosen as the dispersive material.

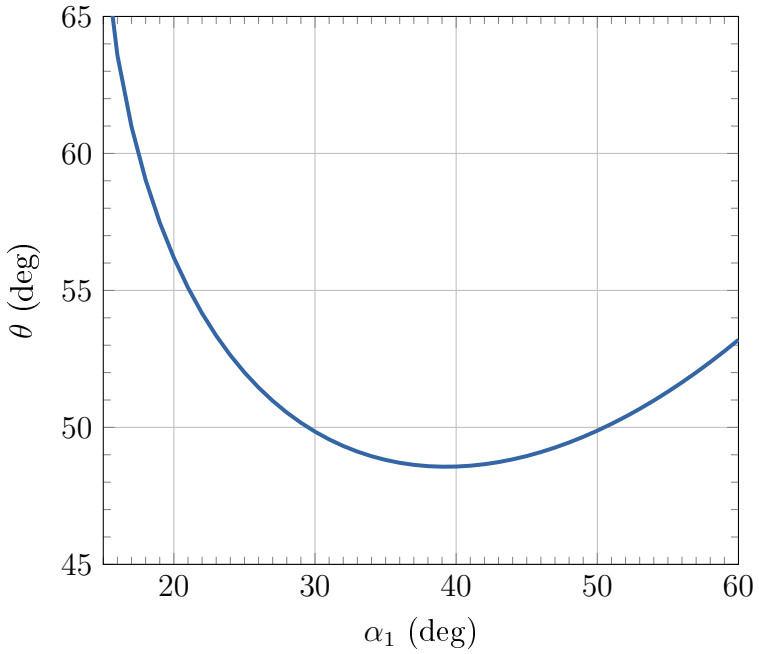

Figure 4.8: Variation in deflection angle, θ, with the angle of incidence, α_1, at $\lambda = 2\,\mu m$, for a single ZnSe prism with an apex angle $\epsilon = 30\,deg$.

Apart from the prism material, the angle of incidence (AOI), α_1, with respect to the front surface normal of the prism, and the apex angle, ϵ, define the total angular deflection, θ, of the light from its original direction of propagation. Regarding the parameters $\lambda = 2\,\mu m$, $n(2\,\mu m) = 2.45$, $\alpha_1 = 40\,deg$ and $\epsilon = 30\,deg$ as an example, the minimum total deflection angle for zinc selenide is already $\theta = 48.6\,deg$ (cf. Figure 4.8).

In combination with the dimension of the prism surface in the dispersive plane, the prism apex angle, ϵ, is a measure for the prism volume that the light has to pass while accumulating losses due to the non-negligible absorption.

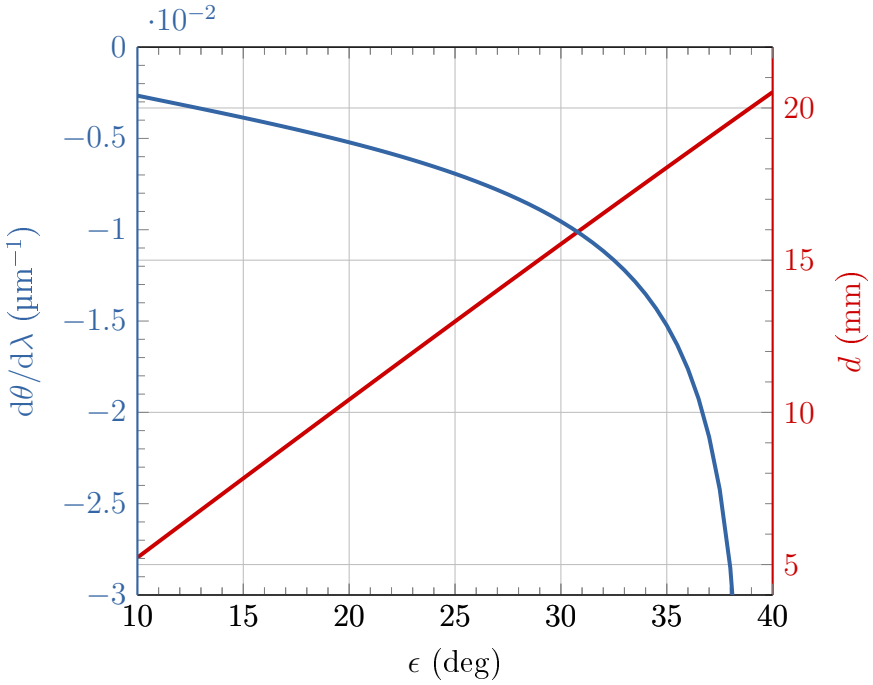

Figure 4.9: Dependency of the angular dispersion (*blue*) on the prism apex angle, ϵ, at $\lambda = 2\,\mu m$, valid for a zinc selenide prism arranged for an angle of incidence $\alpha_1 = 40\,deg$. The corresponding length of material intersection, d, is depicted in *red*. The $\lambda = 2\,\mu m$-component is assumed to enter the prism at the height $h/2 = 29\,mm$ from the prism base for $a = 60\,mm$ (see Figure 3.2a).

Figure 4.9 shows the effect of the apex angle on the angular dispersion, $d\theta/d\lambda$, and the propagation length in a prism with the parameters $\alpha_1 = 40\,deg$, $a = 60\,mm$ at the wavelength of $2\,\mu m$.

In order to cover the full detector width of 31.95 mm with the spectral region of interest between $2\,\mu m$ and $20\,\mu m$, a single prism with the parameters $\alpha_1 = 30\,deg$ and $\epsilon = 34\,deg$ is sufficient. This configuration has the consequence of not only a strong total deflection up to $\theta\,(\lambda = 2\,\mu m) = 63.6\,deg$, but also the angle between the normal of the exit transition surface ZnSe to air and the dispersed rays in the prism (cf. Figure 4.10), β_2, approaches with a value $\beta_2 = 22.2\,deg$ the critical angle of total internal reflection $\beta_{crit} = \arcsin\left(n_{ZnSe}^{-1}\right) = 24.1\,deg$ [80]. Consequently, already a small mismatch of α_1 or ϵ with respect to the design values would lead to a loss of the system functionality.

Double-prism arrangement

Based on various previously developed prism concepts beginning with [116], an arrangement of two or more prisms can be employed to increase, and moreover to adjust, the dispersive power of the system by the introduction of further degrees of freedom provided by the relative arrangement of the prisms. Examples are *direct-view* or *Amici* prisms [117, 118, and references therein] and multi-prism arrangements consisting of different materials or geometries [119–121].

A possible solution for the problem of a transition angle, β_2, close to the critical angle is an arrangement of two independent prisms with lower individual deflection angles, θ_1 and θ_2. Figure 4.10 presents a setup of two consecutive prisms with the definition of the inter-prism angle, Π, between the normals of the subtending surfaces of the two prisms. This adds a further degree of freedom in the deflection angle and the linear dispersion in the detector plane. The derivation of the dispersion formula for the double-prism arrangement is presented in D.3.

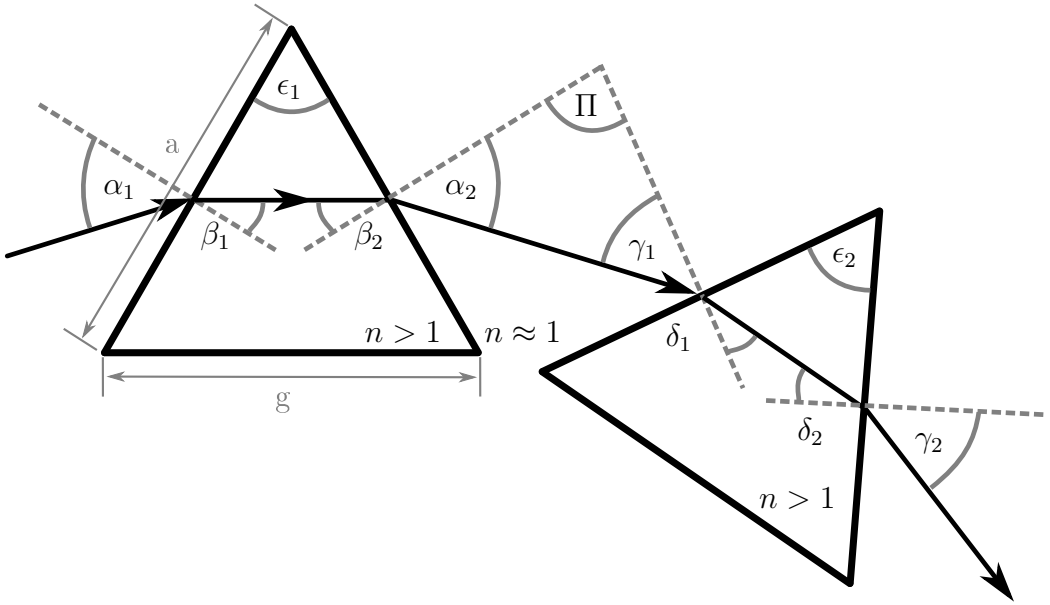

Figure 4.10: Sketch of the double-prism arrangement (not to scale).

During this work, an arrangement was found with $\alpha_1 = 40\,\text{deg}$, $\epsilon_1 = \epsilon_2 = 30\,\text{deg}$ and $\Pi = 105\,\text{deg}$ (see Figure 4.10). This configuration increases the

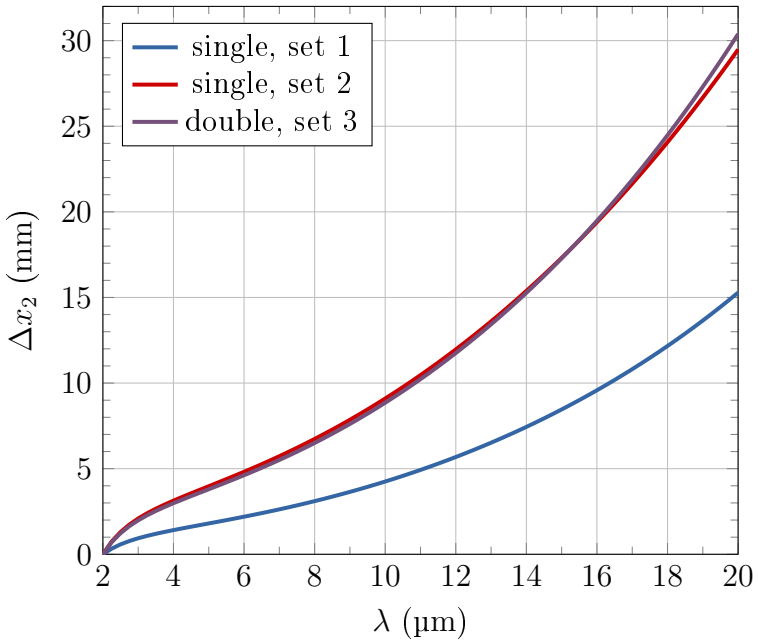

Figure 4.11: Comparison of three prism arrangements. *Set 1*: single prism with $\alpha_1 = 40\,\text{deg}$ and $\epsilon = 30\,\text{deg}$. *Set 2*: single prism with $\alpha_1 = 30\,\text{deg}$ and $\epsilon = 34\,\text{deg}$. *Set 3*: double-prism with $\alpha_1 = 40\,\text{deg}$, $\epsilon_1 = \epsilon_2 = 30\,\text{deg}$ and $\Pi = 105\,\text{deg}$. The focal length of the final focusing mirror was 163 mm in all cases.

optical path length in the prism material (cf. Table 4.4), but enables a continuous linear dispersion suitable for the MCT detector line of 31.95 mm width. In addition, the double-prism setup avoids transition angles, β_2 and δ_2, close to critical values and adds with the inter-prism angle, Π, another degree of freedom to adjust the linear dispersion on the detector plane.

4.2.3 Imaging system

The imaging system determines not only the transmission efficiency of the spectrometer, by matching the transverse beam profile to the detector element dimension, but also defines the spectral resolution limits e. g. due to diffraction effects [86].

The demands on the imaging system, in order to achieve an appropriate transmission efficiency and spectral resolution of the spectrometer, are predominantly defined by the:

1. transition radiation source size and divergence,
2. size of the dispersive elements,
3. slit width or aperture size, i. e. the size of the "object", which is imaged onto the detector plane,
4. the detector element dimension in the dispersive plane and its perpendicular plane.

The most simple imaging system is a telescope-like setup [86] of two focusing elements, which can be mirrors or lenses, arranged as depicted in Figure 4.12. Here, the focusing elements $M0$, $M1$ and $M2$ are shown as lenses. Due to the transmission losses and chromatic effects of IR-compatible lens materials (cf. section 3.1.2), the real design utilises mirrors, in particular off-axis parabolic mirrors (OAP), as focusing elements. OAPs yield no spheric aberrations, but have the disadvantage of their exclusive capability of focusing a point towards infinity and vice versa [122]. Since misalignments of off-axis parabolic mirrors lead to aberrations, a proper alignment of the mirrors has to be ensured (see section 5.1).

The assessment to determine the properties of the complete optical system was done iteratively to consider the influence of one parameter on parameters

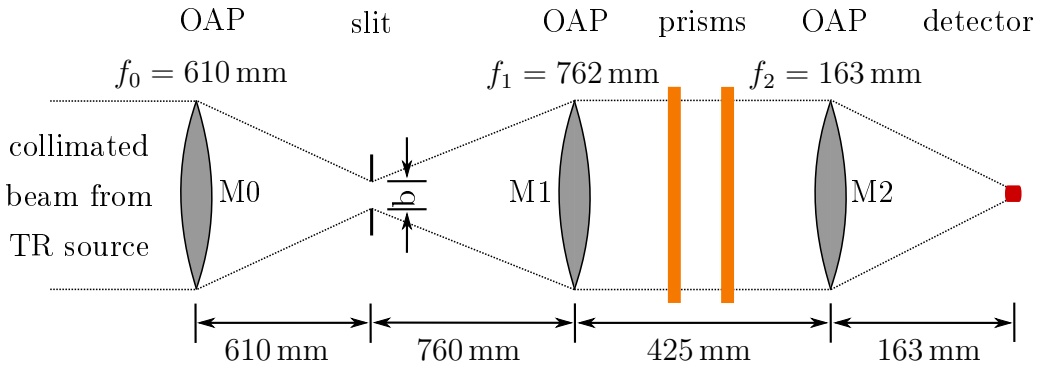

Figure 4.12: Design of the imaging system of the spectrometer. The focusing elements, which are off-axis parabolic mirrors, are depicted as lenses. The slit width, b, is typically 1 mm. Please refer also to section 5.1 for details on the alignment.

directly linked to the first. For example, the focal length of element $M0$, f_0, influences the profile of the transverse intensity distribution on the slit [85] and also the divergence behind the slit and thus, the required dimensions for the dispersive stage.

The design of the imaging system of the spectrometer, which is depicted in Fig. 4.12, is based on an optical setup developed for the experiment on LWFA, presented in appendix B. The light emerging from an aluminium foil, acting as transition radiation emitter, is collimated by a $f/20$ spherical mirror of 1016 mm focal length in order to propagate the radiation over a distance of approximately 3.6 m from the source to the spectrometer setup, in particular to the slit. The spherical mirror is horizontally tilted by 10 deg.

The determination of the entrance aperture width, which is a slit in the dispersive plane, will be presented first. An off-axis parabolic mirror focuses the beam onto this aperture, where, according to simulations with *THzTransport*, the distance between the first maxima of the transverse profile is approximately 1.5 mm at $\lambda = 10\,\mu\mathrm{m}$. The beam profile at the slit for this particular wavelength and a horizontal line out at $y = 0\,\mathrm{mm}$ are depicted in Figure 4.13. Distributions for $\lambda = 2\,\mu\mathrm{m}$ and $18\,\mu\mathrm{m}$ have been added to the latter plot to illustrate the profiles for the extremes of the spectral range. Further details on the simulations are summarised in the appendix 'THzTransport' in section

C.1.

The reduction of the transmitted radiation intensity, which decreases the sensitivity of the spectrometer for low-intensity transition radiation pulses, has to be considered in the determination of the slit width as well as diffraction effects affecting the transverse profile.

A vertical slit arrangement located at the transverse beam centre (cf. Figure 4.13a) suppresses the contribution of the horizontal polarisation in the transmitted light by cropping the transverse profile, since the incident transition radiation is radially polarised (cf. section 2.3). This spatial polarisation filtering simplifies the treatment of reflective losses at the prism surface intersections [85]. The efficiency of the polarisation filtering is wavelength dependent due to wavelength-dependent transverse profile.

Based on the distributions depicted in Figure 4.13b and the assessment of the expected intensities in Figure 4.2, a slit width of $b = 1\,\mathrm{mm}$ is sufficient. The slit still crops the horizontal radiation profile, but ensures a high transmission at wavelengths below 5 µm, which are expected to yield lower spectral energies than longer wavelengths.

The detector element width in the dispersive plane (cf. Table 4.3) is 0.2 mm plus 0.05 mm inactive area, implying that a demagnification of $M = 0.25$ is required to image the slit onto one detector element. Utilising the fundamental relationship for the magnification M of optical systems [86], $M = f_2\, f_1^{-1}$, the first focusing element has to yield a focal length of $f_1 = 4\, f_2$. The choice of $f_2 = 6\,\mathrm{inch} \approx 152\,\mathrm{mm}$ for the focusing element in front of the detector led to the choice of $f_1 = 30\,\mathrm{inch} \approx 762\,\mathrm{mm}$.

Up to this point, the optics in the main spectrometer stage and the slit have been defined and thus the spectrometer now has a fixed acceptance angle, Ω_{lim}. During the selection of the focusing element $M0$, in front of the entrance aperture of the spectrometer, it is necessary to consider the transverse size of the incident collimated light from the TR source and the acceptance angle, Ω_{lim}. Envisaging a focal length, f_0, to be much smaller than f_1, results in a divergence larger than the geometric divergence of $M1$ approximated geometrically by $\phi_{M1} = r_{M1}\, f_1^{-1}$. Hence, the transmission efficiency of the spectrometer is dramatically reduced due to the large transverse extension of the light on the mirror $M1$ of finite diameter. The spectral resolution is simultaneously

distorted by diffraction effects introduced by the boundaries of $M1$ [86]. Consequently, a value $f_0 = 24\,\text{inch} \approx 610\,\text{mm}$, which is slightly smaller than f_1, has been chosen in order to decrease the spot size on the slit at an acceptable divergence with respect to the diameter of $M1$. Figure 4.16 presents calculated transverse profiles at the most important positions in the imaging system at the wavelengths 2 µm, 10 µm and 18 µm.

The light that has been collimated by $M1$ (cf. Figure 4.14) now passes the dispersive stage, which provides a limited clear aperture a_{eff}. The effective aperture, a_{eff}, is given in this case by the projected size of the prisms with respect to the incident radiation: $a_{\text{eff}} = a\cos(\alpha_1) = 46\,\text{mm}$ for $a = 60\,\text{mm}$ and $\alpha_1 = 40\,\text{deg}$. The diffraction due to the finite aperture a_{eff} limits the spectral resolution by degrading the sharpness of the slit image in the detector plane (see section 3.2 and the references cited therein).

The dispersion introduced by the prisms is not only a spatial offset with respect to the centre of the final focusing mirror, $M2$, but also an angular spread, which leads to comatic aberrations [85] and thus, an increase in the focus spot size in the detector plane [87]. In order to reduce this distortion, ray-tracing simulations with the software *ZEMAX* [123] suggested the deflection angle of the off-axis parabolic (OAP) mirror, Ψ, to be lower than 90 deg. A value $\Psi = 30\,\text{deg}$ and a focal length of $f_2 = 163\,\text{mm}$ has finally been chosen for the mirror $M2$. Figure 4.17 depicts the results of the simulations. The corresponding details are specified in section D.5.

Figure 4.15 shows a sketch of the spectrometer setup as it was assembled in November 2013. Notes on the initial alignment including, final distances of the components, can be found in chapter 5.

Since the spectrometer is supposed to operate in areas with limited access, due to radiation protection, all the focusing mirrors, one plane mirror and the slit are equipped with stepper motors and remote control.

The details of the key components used for the optical system are summarised in Table 4.5.

Table 4.4: Prism parameters for a linear dispersion suitable for the available MCT detector line regarding $\lambda = 2\,\mu m$. Please note that the single-prism solution yields the disadvantage of the transition angle, β_2, close to the critical angle for total internal reflection, $\beta_{crit} = 24.1\,deg$.

parameter	unit	value	
		single prism	double prism
linear dispersion Δx_2	mm	31.95	
angle of incidence α_1	deg	30	40
apex angle ϵ	deg	34	30
total deflection angle θ	deg	63.6	97.5
transition angle β_2 (first prism)	deg	22.2	14.8
total material intersection d	mm	17.6	31.1

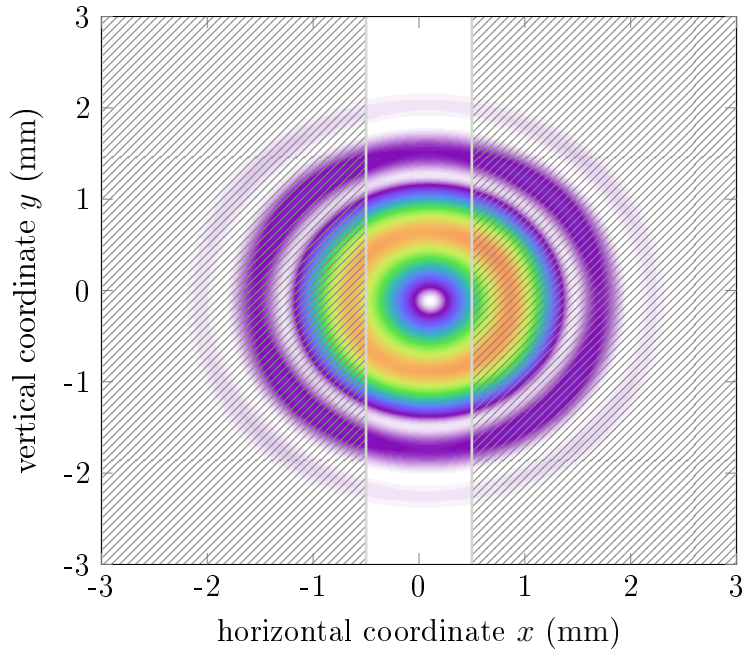

(a) intensity distribution for $\lambda = 10\,\mu m$

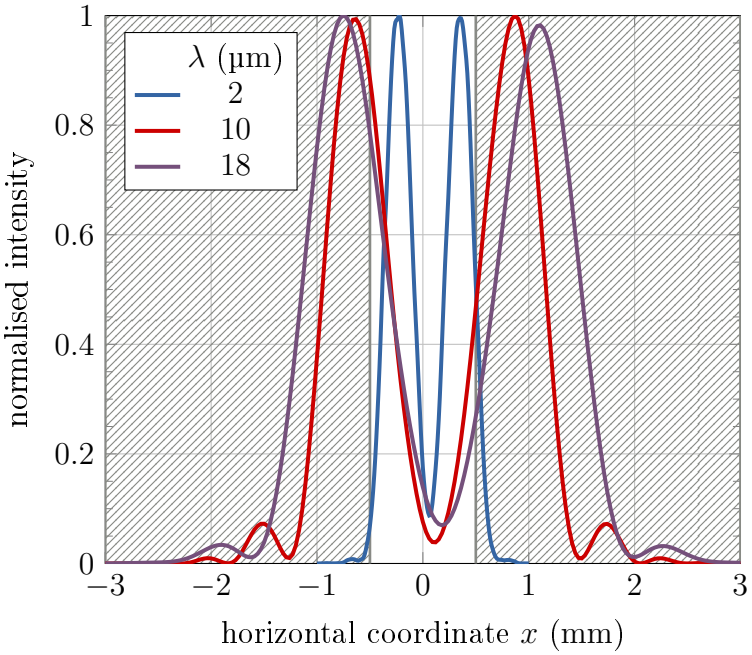

(b) horizontal line distributions at $y = 0\,mm$

Figure 4.13: Intensity distribution on the entrance aperture of the spectrometer determined with *THzTransport* (see section C.1 for details). The asymmetry in the profile is due to a slightly tilted spherical mirror which collimates the light from the transition radiation source. The traces have been normalised individually. The shaded areas indicate the opaque blades of the entrance slit.

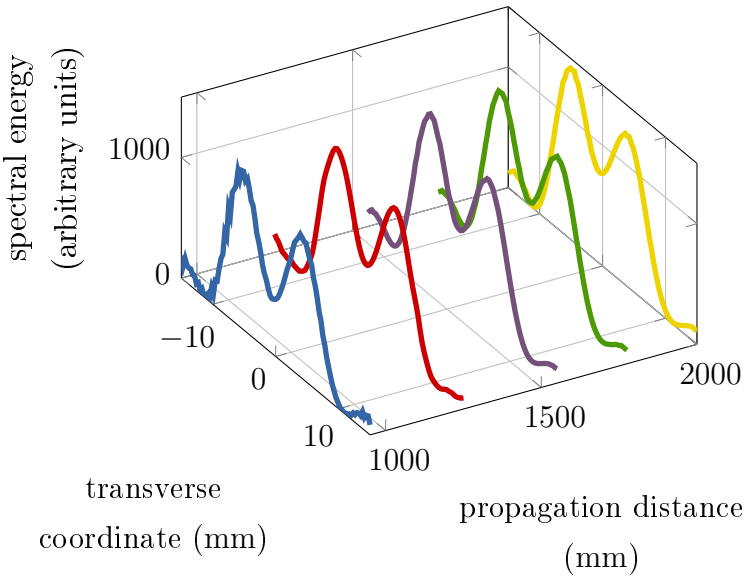

Figure 4.14: Calculated transverse profiles at $\lambda = 10\,\mu m$ for several propagation distances from the collimating mirror, $M1$. As depicted, the radiation passing through the prisms can be treated as collimated. Please note that the final focusing mirror, $M2$, is placed at a propagation distance of 425 mm in the actual setup.

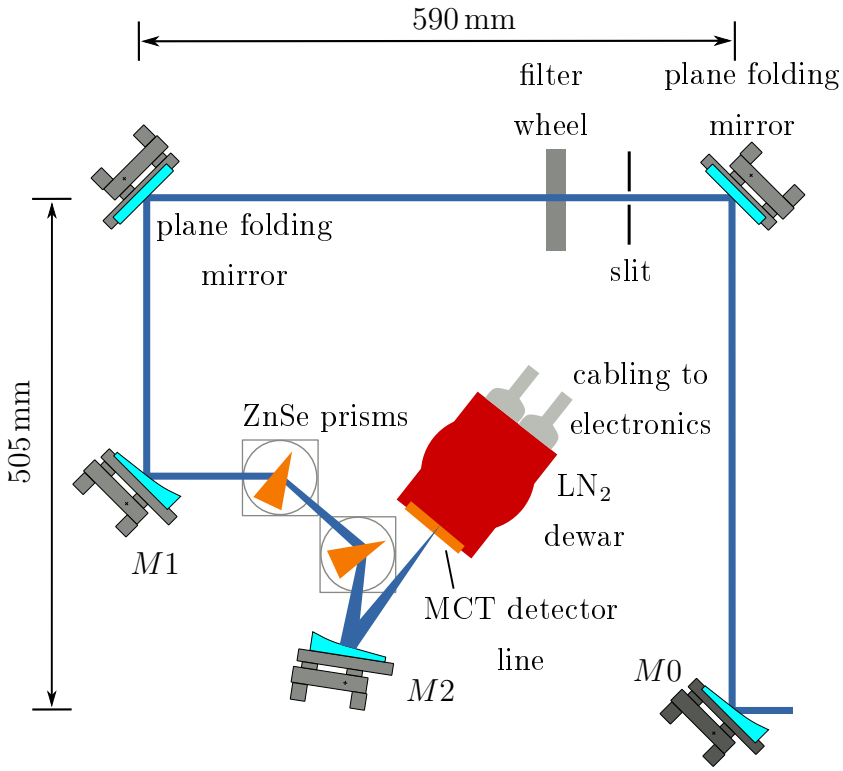

Figure 4.15: Sketch of the double-prism spectrometer setup on an optical breadboard with a footprint of (0.9 x 0.9) m.

Table 4.5: Synopsis of the optical elements of the spectrometer setup.

element	type	dimension (mm)	focal length (mm)	material	supplier
M0	OAP to focus	⌀ 76.2	610	Al-coated aluminium	LT-Ultra [124]
slit	rectangular aperture	(1 x 5)	-	blades: aluminium	in-house
M1	OAP from focus	⌀ 76.2	762	Al-coated aluminium	LT-Ultra [124]
prisms	two isosceles prisms	(60 x 60)	-	ZnSe	Korth Kristalle [125]
M2	OAP to focus	⌀ 76.2	163	Au-coated aluminium	Edmund Optics [126]

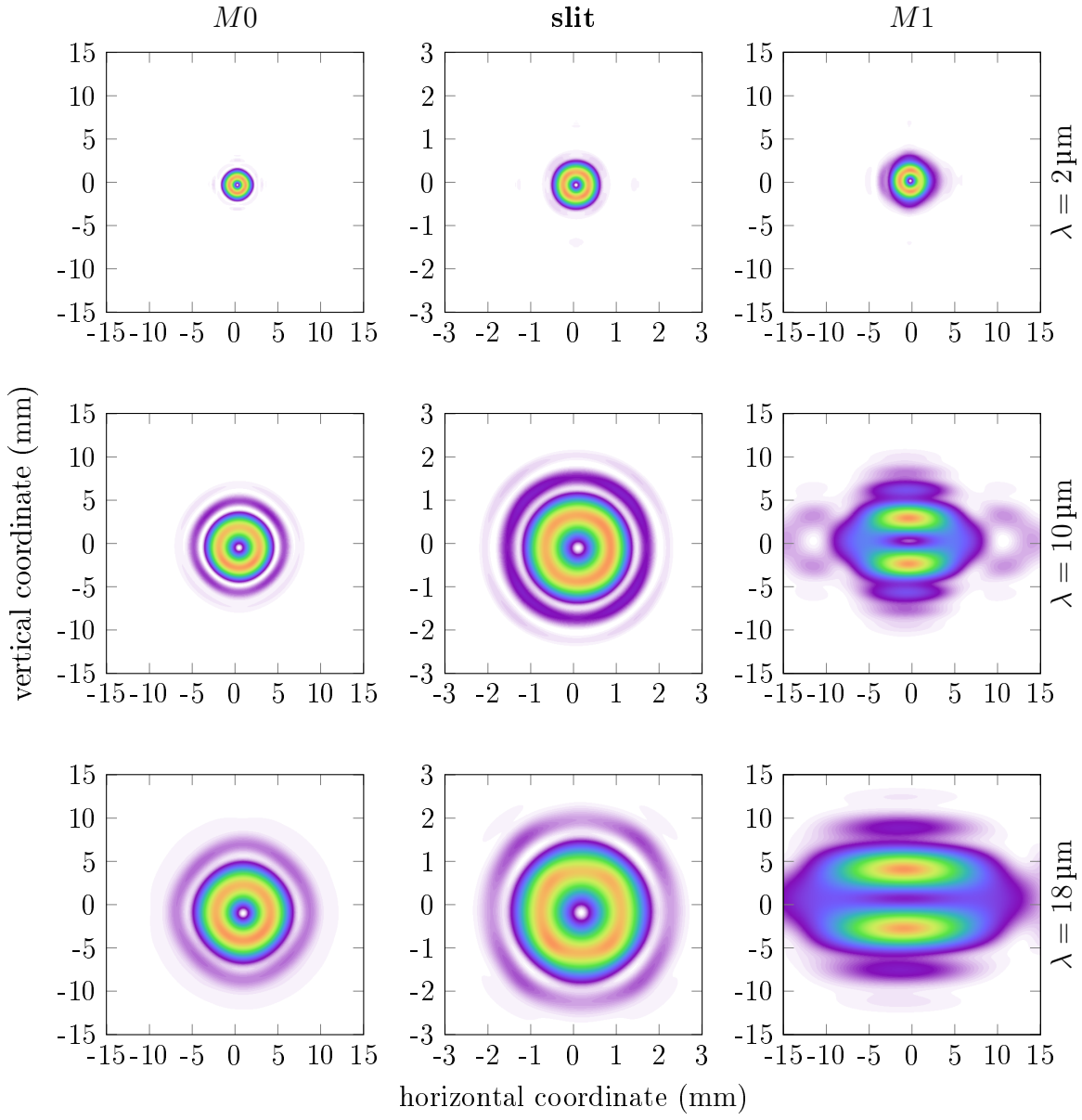

Figure 4.16: Transverse intensity distributions within the imaging system calculated with *THzTransport*. The columns correspond to the positions within the system, i. e. at the first focusing mirror, $M0$, the slit and the collimating mirror, $M1$. The assessment has been done for the wavelengths of 2 µm, 10 µm and 18 µm (*rows*). The intensities are individually scaled.

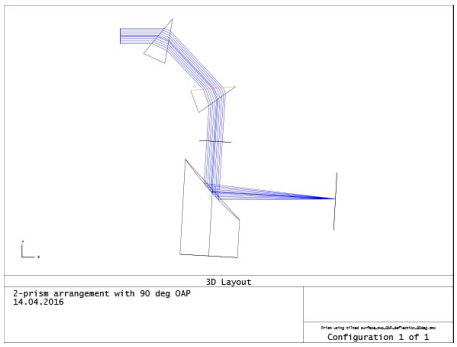

(a) layout with $\Psi = 90\,\mathrm{deg}$

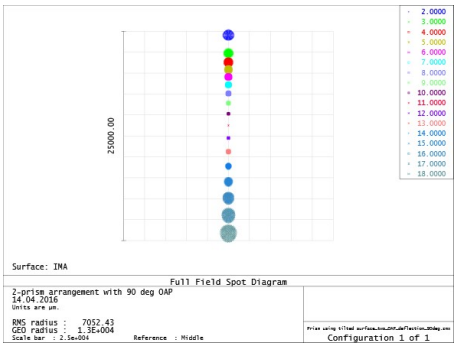

(b) distribution in the focal plane

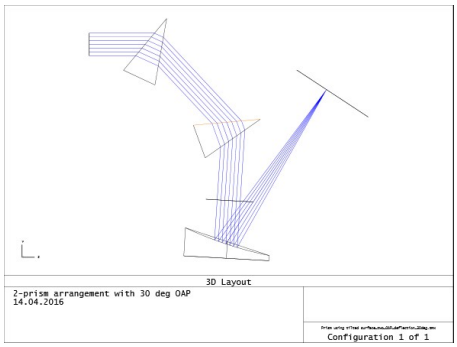

(c) layout with $\Psi = 30\,\mathrm{deg}$

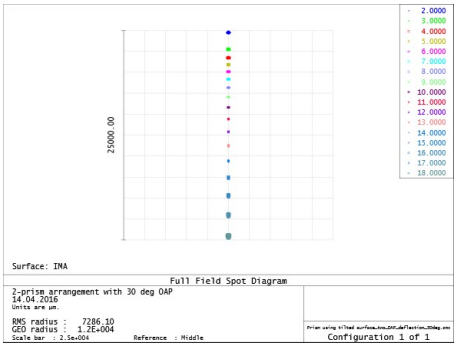

(d) distribution in the focal plane

Figure 4.17: Results of the ray-tracing simulations with ZEMAX OpticStudio [123]. The figures (a) and (c) show the layouts the simulations with deflection angles of the off-axis parabolic mirrors, $\Psi = 90\,\mathrm{deg}$ and $\Psi = 30\,\mathrm{deg}$ respectively. The transverse distribution of the rays are depicted in (b) and (d). The overall extension of the rectangular grids is 25 mm. The spot size in the focal plane is significantly smaller for $\Psi = 30\,\mathrm{deg}$.

5 Characterisation and Data Analysis

In order to determine the longitudinal form factor, F_{long}, of femtosecond electron bunches, the instrument must be aligned and characterised. The measured detector signals, which are voltage readings for each of the 128 detector elements, have to be calculated into spectral intensities at the centre wavelengths of the individual elements and corrected for the radiation transport from the transition radiation source to the spectrometer. These procedures, the characterisation and data analysis are introduced in this chapter, whereas results are presented in chapter 6.

The software MATHEMATICA [107] was used to perform the data analysis and the numerical operations as well as inter- and extrapolation, fitting and integration.

5.1 Initial alignment

The spectrometer setup, depicted in Figure 4.15, was pre-aligned in a two-step process. First, the mirrors were mounted according to a reference beam path set by an optical laser operated at $\lambda = 637\,\mathrm{nm}$. This was done without mounting the prisms, which do not bend the laser in accordance with the design wavelength range of the spectrometer. The laser beam path through the dispersive stage was bypassed by a plane mirror and guided onto the final focusing mirror, $M2$, and the detector. The prism angles were set by custom made prism mounts on commercial rotation bases, which allow the reproducible placement of the prisms after transportation of the system.

The final alignment of the spectrometer was carried out at the transition radiation source at the FLASH facility (section A.3 in appendix A). The tran-

sition radiation was centred on the optical elements and alignment markers with the help of a single-element pyroelectric detector.

The distance between the collimating mirror, $M1$, and the bisector of the apex angle of the first prism was measured to be (140 ± 5) mm and the distance from this point to the apex bisector of the second prism to be (105 ± 5) mm. The propagation length from the apex bisector of the second prism to the final focusing mirror, $M2$, is measured to be (180 ± 5) mm. The placement of the MCT detector line with respect to the final focusing mirror was adjusted to the position of the highest detector signal integrated over the 128 elements, which lead to the measured distance of (185 ± 5) mm.

Table 5.1: Overview of the distances between the optical elements in the spectrometer after the optical alignment. The error is estimated to be ± 5 mm.

distance	unit	value
$M0$ - slit	mm	610
slit - $M1$	mm	760
$M1$ - apex bisector prism 1	mm	140
apex bisector prism 1 - 2	mm	100
apex bisector prism 2 - $M2$	mm	170
$M2$ - detector line	mm	185

5.2 Wavelength calibration

The assignment of a wavelength interval to the spatially extended detector elements is ideally conducted with a well-understood tunable and pulsed IR source providing a narrow bandwidth, which scans through the complete wavelength span of the spectrometer. For the mid-infrared regimes, free-electron lasers like FELBE [127] and FELIX [128] are suitable light sources providing narrow spectral bandwidths of typically 1 % in a widely tunable wavelength range. These large-scale devices offer limited availability for beam time due to enormous technological and financial cost associated with their use. In addition, laser systems based optical parametric amplification and oscillators

provide pulses of tunable centre wavelengths in the mid-infrared regime [129, 130].

A simpler approach is the use of narrow bandwidth band pass filters [85] and a broadband source. Examples are thermal radiators [93] and transition radiation sources, where the first yield the disadvantage of the need for an optical chopper to transform the constant light flux into pulses. Transition radiation sources driven by sub-picosecond high-relativistic electron bunches offer intrinsically short pulses with a broad spectrum [79]. The width and accuracy of the transmission band of the filters limit the validity of the wavelength calibration, which thereby relies on the specifications provided by the manufacturer. However, this method enables a validation of an acquired calibration curve at each measurement shift.

5.2.1 Calibration with band pass filters

An initial calibration of the double-prism spectrometer was performed using band pass filters between 4 µm and 16 µm, this is cross-checked with measurements taken during a beam time at the FELIX infrared-FEL facility - cf. section 6.1.2.

The initial calibration was conducted with filters from Laser Components GmbH [131] covering the wavelength range between 4 µm and 16 µm. The characteristics of the filters are presented in Table 5.3. The filters are mounted in a motorised and remote-controllable filter wheel. The acquisition of filter spectra during every measurement shift confirms the validity of the calibration regarding possible errors by deviations in the incoupling angle of the transition radiation.

An example of spectra with band pass filters is depicted in Figure 5.1. The centres of the transmission lines of the filters are determined by approximating a Gaussian function for detector element # to the data points. The thereby calculated mean values are assigned to the filter centre wavelengths, λ_c. The amplitude, the mean, μ, and the width corresponding to the square root of the variance, σ, are calculated and averaged for a few hundred single spectra. The approximated functions for the 14 µm ($\lambda_c \mathrel{\widehat{=}} \mu = (81.4 \pm 0.1)$) and 16 µm ($\mu = (94.1 \pm 0.1)$) filters are included in Fig. 5.1 as examples. The raw signals of elements above no. 97 are affected by distortions due to the non-

linear dispersion and imaging errors, which are pronounced in comparison to short wavelength due to the larger transverse profile. These signals have been omitted in the calculation of the centre wavelength of the 16 µm-filter.

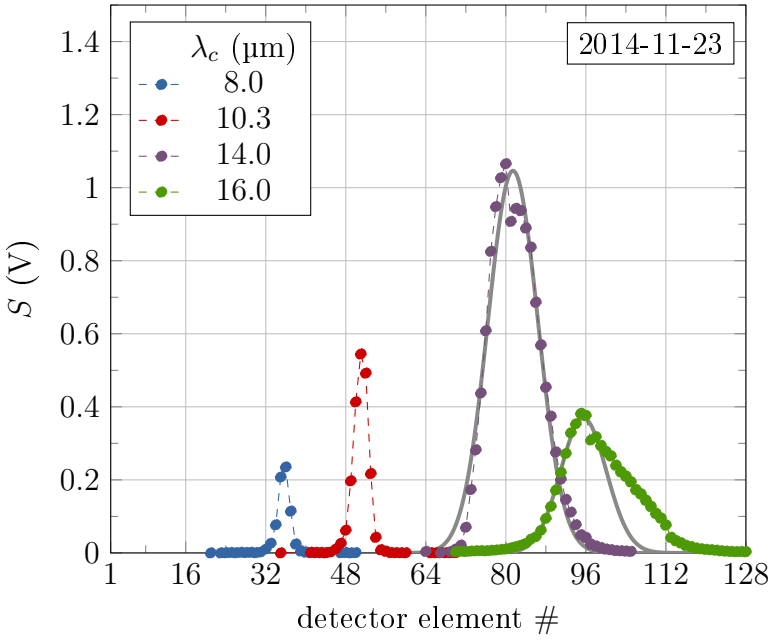

Figure 5.1: Spectra with band pass filters with centre wavelengths $\lambda_c = 8.0\,\mu m$, 10.3 µm, 14.0 µm and 16.0 µm. Please refer to Table 5.3 for details. The traces are the mean values of several hundreds of single-shot spectra, S, with negligible error bars (standard deviation of the mean of the detector voltage signals). A Gaussian fit function has been calculated for each filter to determine the wavelength calibration. Examples of the fit functions are exemplarily shown in *grey*. The dashed lines connect the data points for visual guidance.

The wavelength calibration of the system is described by a function which is based on the analytical dispersion formula for the double-prism arrangement (see Fig. 5.2). The analytical dispersion formula (cf. section D.3 in appendix D) depends, among other factors, on the angle of incidence, α_1, the inter-prism angle, Π, the focal length of the final focusing mirror, f_2, and a horizontal offset, Δx_{offset}.

Since the distribution of the wavelength assignments from the band pass filters does not match exactly the analytical function, the parameters α_1, Π, f_2 and Δx_{offset} are optimised by a weighted fit utilising the MATHEMATICA [107]

function `NonLinearModelFit` under consideration of the filter bandwidths. The range of allowed parameter values was restricted to mitigate non-physical results.

Figure 5.2 presents the results for the data set acquired on the 23rd of November 2014, including the locations of the centre wavelengths of the band pass filters, analytical dispersion function regarding the design values and the adjusted calibration function. The parameters of the fit are summarised in Table 5.2. Even though the parameters labelled with (*) approached the boundary of allowed values in the optimisation, the adjusted calibration function follows the positions of the band pass filters with a mean residual in the assigned filter centre wavelength of approx. two detector elements, which is, regarding the spectra in Fig. 5.2 in the acceptable range.

A comparison to a measurements acquired at the FELIX facility is depicted in section 6.1.2.

Table 5.2: Initial and optimised parameters in the dispersion function, which correspond to the *blue* and *red* curves in Figure 5.2 respectively.

parameter	unit	value	
		initial	optimised
angle of incidence α_1	deg	40	37.5*
inter-prism angle Π	deg	105	108*
focal length f_2	mm	163	166*
horizontal offset Δx_{offset}	mm	–	285.9

5.3 System performance

5.3.1 Spectral resolution

Apart from the wavelength calibration with the band pass filters, the spectral resolving power was studied by inserting a low density polyethylene (LDPE) foil of unknown thickness into the beam path. The measurements and a transmission model, which considers transmission oscillations due to interference of internally reflected fractions of the incident radiation [80, § 14.4 therein],

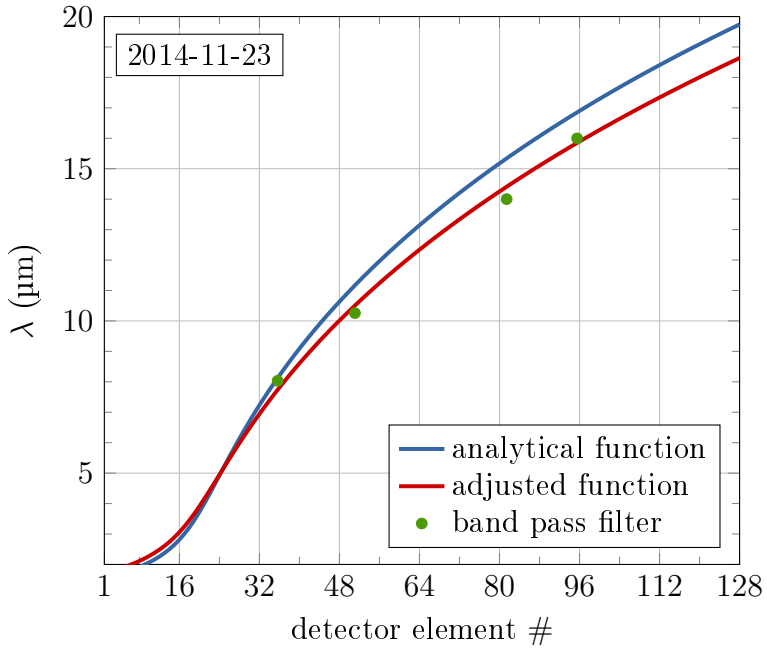

Figure 5.2: Analytical and adjusted calibration function acquired on 23rd of November 2014. The parameters in the analytical dispersion function (*blue*) are adjusted by a fit. The resulting calibration function is depicted in *red*. The abscissa of the data points (*green*) is the mean value calculated from several hundred single spectra. The standard deviation of the mean is below 3 ‰ with respect to the mean. The ordinate is the specification of the centre wavelength by the supplier [131]. These values are specified with respect to a tolerance of ± 3 ‰.

are depicted in Fig. 5.3. The model is valid for the polarisation parallel to the plane of incidence and a material thickness, d, which has been adjusted to $\approx 26\,\mu m$.

Please note that the transition radiation is radially polarised. The entrance slit of the spectrometer acts as a polarisation filter and transmits the s-polarisation, perpendicular to the plane of incidence (cf. section 4.2.3). Since the beam polarisation is rotated by $\pi / 2$ in the optical path between foil and slit, the model has been restricted to the polarisation parallel to the plane of incidence.

The depicted data, acquired at the FLASH facility, have been derived from

Table 5.3: Key data of the available band pass filters as specified by the supplier [131]. These filters are used for determining and validation of the calibration function at each measurement campaign.

centre wavelength λ_c (nm)	bandwidth (nm)	normalised peak transmission
3988	44 ± 12	0.74
8033	155 ± 24	0.83
10257	134 ± 31	0.72
14001	791 ± 42	0.84
15997	1627 ± 40	0.79

the mean of $>$ 1000 single-shot spectra, taken with LDPE foil, and have been divided by the mean of $>$ 1800 spectra without foil at the same electron beam parameters. The measured transmission at the two absorption lines $\lambda \approx 6.8\,\mu\text{m}$ and $\lambda \approx 13.7\,\mu\text{m}$ [132] does not reach the minimum close to zero transmission, which is predicted by the model. This indicates that the bandwidth covered by the detector elements is not small enough to resolve the absorption lines entirely. A possible explanation is that the actual transverse size of the focus in the detector plane is larger than expected. A future improvement may be achieved by confirming the optimal detector position in the focus of the final focusing mirror.

Nonetheless, the figure depicts that the position of the two absorption lines of LDPE can be resolved clearly. In addition, also the oscillations are visible in the transmission signal.

5.3.2 Signal-to-noise ratio

The signal-to-noise ratio, $r_{S/N}$, has been defined as the detector signal amplitude, S, divided by the sample root mean square (r.m.s.) noise, σ_{bg}, of the detector without being exposed to transition radiation, i. e. of the background radiation level.

$$r_{S/N} = \frac{S}{\sigma_{\text{bg}}}. \tag{5.1}$$

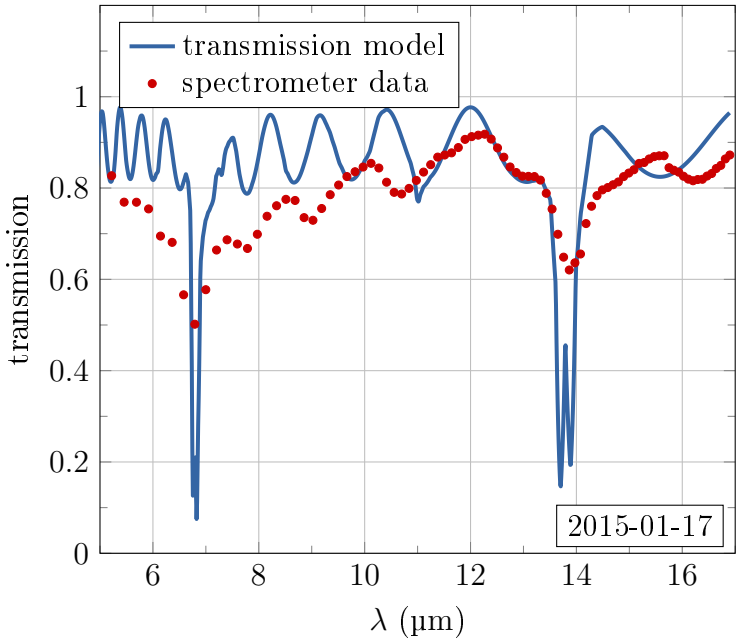

Figure 5.3: Measured transmission data and model for a LDPE foil. The model (*blue*) is valid for the polarisation parallel to plane of incidence. The parameter of the material thickness has been adjusted to $d = 25.5\,\mu\text{m}$.

The signal-to-noise ratio also enables the comparison of different detector systems under the condition of adequate imaging properties. As depicted in section 3.5.3, the power of an incident radiation pulse, which invokes a detector signal equal to the noise level, is called the noise-equivalent power, P_{NEP}, and hence, $r_{S/N}$ is unity.

In addition, $r_{S/N}$ is an important measure to evaluate the significance of a detector measurement, e. g. by defining a threshold of a multiple of $r_{S/N}$, below which a measured signal is rejected. The section 5.5 presents further details on the data analysis.

Figure 5.4 presents the charge dependency of the signal-to-noise ratio for data acquired on the 18th of January 2015. Here, the ratio $r_{S/N}$ has been calculated for the mean of more than 1300 single-shot spectra for each charge setting. Accordingly, σ_{bg} is replaced by the r.m.s. value of the mean of a certain number of background spectra, $\overline{\sigma_{\text{bg}}}$. Details on the definitions of the statistical measures can be found in section D.2.

The measure $\overline{r_{S/N}}$ is the average of the 128 detector elements. The charge

was measured with a RF resonator-based dark current monitor [133]. Since the direct assignment of a single-shot charge measurement to a single-shot spectrum was not possible at that time due to different read-out systems (cf. section 4.2.1), the mean values of the charge measurements and the spectra are calculated and shown in Fig. 5.4. At the setting with $Q = 15.6\,\mathrm{pC}$, the standard deviation was calculated to be approx. 15 fC. The error bars for $\overline{r_{S/N}}$ denote the standard deviation of the mean value of the 128 detector elements.

The spectrometer shows an average signal-to-noise of $\approx$ 2000 at a bunch charge of 4.9 pC and a value $\overline{r_{S/N}} \approx 750$ was observed for $Q \approx 3.8\,\mathrm{pC}$, which is close to the background noise level of the dark current monitor. The dashed curve is a fit function $\overline{r_{S/N}}(Q) = C_1\,Q^2 + C_2\,Q$ which expresses the nature of the emission of incoherent ($\propto Q$) and coherent ($\propto Q^2\,|F|^2$) transition radiation introduced in formula (2.11). The constants C_1 and C_2 have been determined to $C_1 = 36.8\,\mathrm{pC}^{-2}$ and $C_2 = 125.6\,\mathrm{pC}^{-1}$.

An extrapolation of the curve, $\overline{r_{S/N}}(Q)$, indicates an average signal-to-noise of 10 at $Q \approx 80\,\mathrm{fC}$. Referring to section 6.2.1, the detection limit of the dark current monitor was estimated from the background noise level to $Q \approx 3.7\,\mathrm{pC}$.

The reader should be aware that the CTR signal is, as introduced by formula (2.11), not only dependent on Q^2 but also on the bunch duration encoded in $|F|^2$. Although the RF parameters of the accelerator have been kept constant during the measurements, charge-dependent effects may also affect the bunch compression regime. An in-depth treatment of these effects can be found in the literature, e. g. in [134] and the reference cited therein.

In conclusion, the spectrometer is able to diagnose low-charge electron bunches at sufficient signal-to-noise ratios. The charge sensitivity of the spectrometer is higher than the sensitivity of the standard charge diagnostics of the FLASH facility. An illustration of the maximum detectable electron bunch length can be found in section 6.2.3.

5.3.3 Linearity

In the ideal case of a perfect linearity, the voltage signal of the spectrometer, S, scales linear with the power of the incident transition radiation. In order to confirm the linearity, the spectrometer signal has been investigated with varying incident transition radiation intensity. The TR pulses have been at-

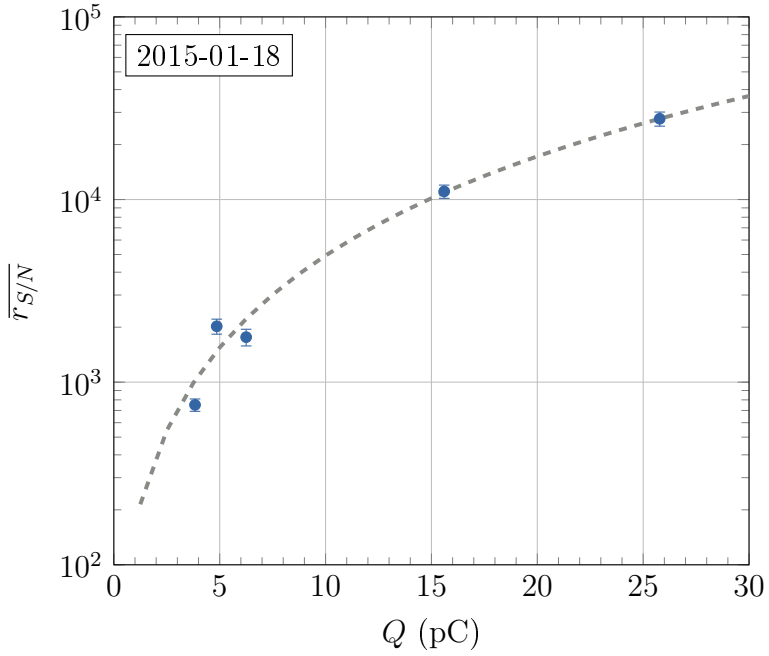

Figure 5.4: Mean of the signal-to-noise ratio, $\overline{r_{S/N}}$, for different charge settings at constant RF parameters (*blue dots*). For each charge setting, the mean of several hundreds of spectra and charge measurements was calculated. The signal-to-noise ratios of the 128 detector elements, covering the wavelength range of approx. 2 µm to 18 µm, have been averaged. The dashed curve represents the fit function $\overline{r_{S/N}}(Q) = C_1\,Q^2 + C_2\,Q$ with $C_1 = 36.8\,\mathrm{pC}^{-2}$ and $C_2 = 125.6\,\mathrm{pC}^{-1}$. The electronic gain factor for the measurements was $G = 16$ (cf. section 5.4.1).

tenuated with a set of two infrared polarisers [85, 135, model P03]. Within the wavelength range of the spectrometer, the polarisers are specified to yield an attenuation of 10^4 for the polarisation perpendicular to the optical axis of the polariser and a sufficiently flat transmission for light polarised in parallel to the optical axis.

The first polariser ensures the transmission of only one polarisation, whereas the second attenuates the incident light pulses following *Malus' Law* [85]. The transmitted intensity scales with $\cos^2(\chi)$, where χ denotes the angle between the electric field vector of the linearly polarised light and the optical axis of the polariser.

The set of polarisers was characterised with a broadband pyroelectric detector for the non-dispersed transition radiation. The integral of the signals from the 128 MCT detector elements was calculated for different polariser angles, χ. The results, normalised to their respective maxima, are presented in Figure 5.5a. The solid line corresponds to the transmission reference acquired with the pyroelectric detector. Fig. 5.5b depicts accordingly the transmission measured with the MCT system with respect to the reference transmission. The peak signal of the MCT detector was approximately 1.9 V, which corresponds to $\approx$ 40 % of the dynamic range at the maximum electronic gain, $G = 16$. The comparison strongly depends on the quality of the polarisers and the linearity of the pyroelectric detector, which have been considered to be optimal [66, 136].

Under these preconditions, the behaviour presented in Figure 5.5 indicates that the spectrometer signal is sufficiently linear with the incident radiation intensity.

5.3.4 Electronic gains

The remotely-selectable capacitance of the integrator introduces the possibility to scale the integrator output signal of the detector readout system (cf. section 4.2.1). This feature allows the adjustment of the integrator outputs to the dynamic range of the analogue-to-digital converter (ADC).

The output voltage, u_{out}, of an integrator can be modelled by

$$u_{\mathrm{out}}(t) \propto \frac{1}{R_{\Omega}\, C} \int_0^t u_{\mathrm{in}}(t)\, \mathrm{d}\, t + \text{const.},$$

with the input voltage, u_{in}. In a standard operational amplifier-based integrator, the resistance, R_{Ω}, and capacitance, C, are connected in parallel [95].

In order to verify the linear dependency of u_{out} with C^{-1}, a comparison of the r.m.s. noise of the mean of several hundreds of single-shot spectra has been prepared for all gain settings of the *high-gain mode*. The data for the spectral region between 12 µm and 14 µm have been averaged.

The gain factor, G, (see chapter 4) has been defined as a measure which is relative to the lowest possible gain setting. Therefore, only the treatment of gain factor ratios, $G_x \,/\, G_y$, for various gain settings, x and y, is qualified for a comparison. The Table 5.4a presents the expected ratio, as derived from

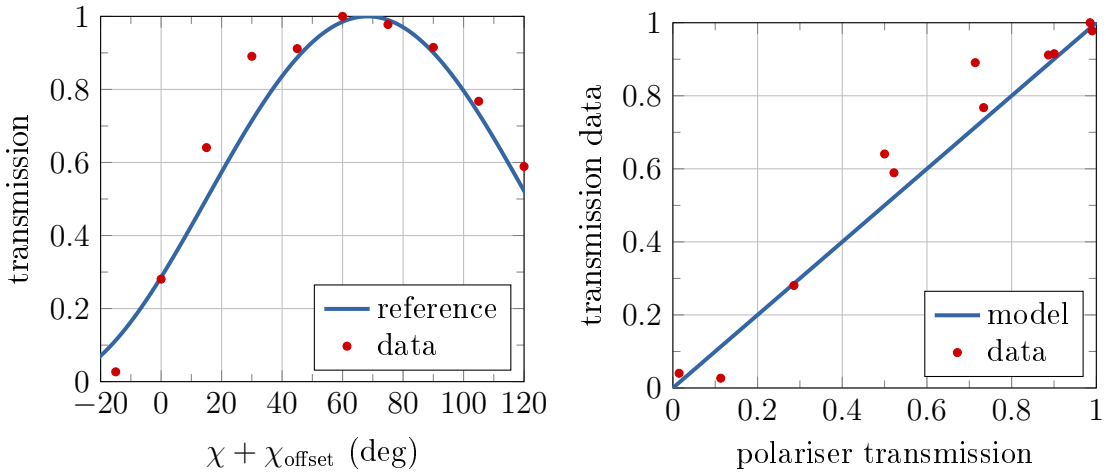

(a) scan of the polariser angle

(b) correlation between reference and data

Figure 5.5: Investigation of the linearity of the spectrometer signal with the incident radiation power. (*Left*) Measured and expected transmission in dependency of the polariser angle, χ. The reference (*blue line*) was recorded with a pyroelectric detector. The *red dots* correspond to the measurements with the MCT system. The angle offset of the polariser, χ_{offset}, was determined to 68.3 deg. (*Right*) Correlation between expected polariser transmission and measured transmission. Both plots show averaged data with negligible statistical fluctuations.

Table 4.2b, for the gain settings specified in the column and row headers. As an example, the quotient 8 in the eighth column of the first row is the result of

$$\frac{G_{\text{setting 7}}}{G_{\text{setting 0}}} = 8.$$

The measured ratios, taken under the same beam parameters, are presented accordingly in Table 5.4b. The statistical uncertainty of the last digits, the standard deviation of the mean of the elements which cover $\lambda = (12 - 14)\,\mu\text{m}$, is given in brackets. The measured ratios follow the expected values fairly well.

Table 5.4: Expected and measured gain factor ratios for the gain settings in the *high-gain mode*. The statistical uncertainty of the last digits of the measured ratio is given in brackets.

(a) expected ratios

setting	0	1	2	3	4	5	6	7
0	1	1.14	1.33	1.60	2	2.67	4	8
1		1	1.17	1.40	1.75	2.33	3.50	7
2			1	1.20	1.50	2	3	6
3				1	1.25	1.67	2.50	5
4					1	1.33	2	4
5						1	1.50	3
6							1	2
7								1

(b) measured ratios

setting	0	1	2	3	4	5	6	7
0	1.00 (2)	1.13 (3)	0.97 (3)	1.32 (4)	1.80 (5)	2.08 (7)	3.40 (9)	8.07 (18)
1		1.00 (3)	0.86 (3)	1.17 (4)	1.59 (5)	1.85 (7)	3.02 (9)	7.16 (19)
2			1.00 (3)	1.36 (5)	1.86 (6)	2.15 (8)	3.52 (11)	8.35 (23)
3				1.00 (3)	1.36 (4)	1.58 (6)	2.58 (8)	6.13 (17)
4					1.00 (3)	1.16 (4)	1.89 (5)	4.49 (11)
5						1.00 (4)	1.64 (6)	3.88 (12)
6							1.00 (3)	2.37 (6)
7								1.00 (2)

5.4 The response function, or, the way from a raw signal to the form factor

The modulus of the longitudinal form factor, $|F_{\mathrm{long}}|$, which was introduced in chapter 2.3, can only be derived from the detector signal with the knowledge of the total charge per electron bunch, Q, the emission of TR from a single electron, the properties of the optical system which images the TR source onto the detector plane and the intensity calibration of the detector system.

The first has to be measured using, for example, a dark current monitor [133], an integrated current transformer (ICT) [137] or a calibrated scintillation screen [59]. The single-particle transition radiation emission as the second contribution can be calculated analytically [79], whereas the optical transport of the radiation has to be calculated numerically. The code *THzTransport* [79, 106] is an appropriate tool for this application due to the consideration of near-field diffraction effects.

The coherently emitted spectral energy density, $\frac{\mathrm{d}U}{\mathrm{d}\lambda}$, after the propagation through an optical system of limited acceptance angle, Ω_a, can be represented by modifying Equation (2.11) following [66]

$$\left(\frac{\mathrm{d}\,U}{\mathrm{d}\,\lambda}\right)_{\mathrm{det}} = N^2\,|F_{\mathrm{long}}|^2 \int_{\Omega_a} |F_{\mathrm{trans}}|^2 \left(\frac{\mathrm{d}^2\,U}{\mathrm{d}\,\lambda\,\mathrm{d}\,\Omega}\right)_{1,\,\mathrm{det}} \mathrm{d}\,\Omega, \tag{5.2}$$

with the contributions of the number of radiating particles, $N = Q\,q_e^{-1}$, the transverse form factor, $|F_{\mathrm{trans}}|^2$, and the expected single-particle fraction at the detector plane, $\left(\frac{\mathrm{d}^2 U}{\mathrm{d}\,\lambda\,\mathrm{d}\,\Omega}\right)_{1,\,\mathrm{det}}$. The longitudinal component of the form factor is only weakly dependent on the observation angle with respect to the direction of propagation of TR, that is generated by electrons at highly relativistic velocities. Therefore, $|F_{\mathrm{long}}|^2$ is moved to the front of the integral.

The calculation of $|F_{\mathrm{long}}|^2$ from $\left(\frac{\mathrm{d}U}{\mathrm{d}\lambda}\right)_{\mathrm{det}}$ is facilitated with the system response function, R. The system response function is the connection between the expected voltage signal of the detector system, S, which corresponds to $\left(\frac{\mathrm{d}U}{\mathrm{d}\lambda}\right)_{\mathrm{det}}$, and the spectral energy of transition radiation generated by an electron bunch of a certain charge and transverse shape. The unit of R is $\mathrm{V\,C^{-2}}$. As depicted in [66], a transversally Gaussian shaped bunch with $\sigma_{\mathrm{trans}} = 200\,\mu\mathrm{m}$ and a bunch charge $Q = 1\,\mathrm{nC}$ has been chosen as normalisation of R.

Re-interpreting Formula (5.2) yields for the spectral energy at the detector plane, U_{det},

$$\begin{aligned} U_{\mathrm{det}}(\#) &= \int_{\lambda_{\min}(\#)}^{\lambda_{\max}(\#)} \int_{\Omega_d} \left(\frac{\mathrm{d}^2 U}{\mathrm{d}\,\lambda\,\mathrm{d}\,\Omega} \right)_{\mathrm{det}} \mathrm{d}\,\Omega\,\mathrm{d}\,\lambda \\ &= N^2\ |F_{\mathrm{long}}|^2 \int_{\lambda_{\min}(\#)}^{\lambda_{\max}(\#)} \int_{\Omega_d} |F_{\mathrm{trans}}|^2 \left(\frac{\mathrm{d}^2 U}{\mathrm{d}\,\lambda\,\mathrm{d}\,\Omega} \right)_{1,\ \mathrm{det}} \mathrm{d}\,\Omega\,\mathrm{d}\,\lambda \\ &= Q^2\,q_e^{-2}\ |F_{\mathrm{long}}|^2 \int_{\lambda_{\min}(\#)}^{\lambda_{\max}(\#)} \int_{\Omega_d} |F_{\mathrm{trans}}|^2\ C_R \left(\frac{\mathrm{d}^2 U}{\mathrm{d}\,\lambda\,\mathrm{d}\,\Omega} \right)_{1} \mathrm{d}\,\Omega\,\mathrm{d}\,\lambda \\ &= Q^2\ |F_{\mathrm{long}}|^2\ R^*, \end{aligned} \tag{5.3}$$

with the elementary charge, q_e, the single-electron spectral energy at the detector plane, $\left(\frac{\mathrm{d}^2 U}{\mathrm{d}\,\lambda\,\mathrm{d}\,\Omega}\right)_{1,\ \mathrm{det}}$, and at the source, $\left(\frac{\mathrm{d}^2 U}{\mathrm{d}\,\lambda\,\mathrm{d}\,\Omega}\right)_{1}$. The correct treatment of the spatially extended detector elements is ensured with the integration over the solid angle imposed by the detector elements and the imaging system, Ω_d. The wavelength integral covers the bandwidth intervals of the detector element spanning $\Delta\lambda = \lambda_{\max}(\#) - \lambda_{\min}(\#)$, which is determined from the calibration function of the spectrometer. The integrals represent the appropriate conversion of the detector signals into spectral intensities. The factor $C_R = C_R(\#)$ accounts for wavelength dependencies in the optical system and is discussed in section 5.4.1.

The partial response

$$R^* = R^*(\#) = q_e^{-2} \int_{\lambda_{\min}(\#)}^{\lambda_{\max}(\#)} \int_{\Omega_d} |F_{\mathrm{trans}}|^2\ C_R \left(\frac{\mathrm{d}^2 U}{\mathrm{d}\,\lambda\,\mathrm{d}\,\Omega} \right)_{1} \mathrm{d}\,\Omega\,\mathrm{d}\,\lambda \tag{5.4}$$

with the unit

$$[R^*] = \mathrm{J\,C^{-2}}$$

now expresses the spectral energy at the source, which is emitted coherently by a single electron of charge q_e.

In order to derive the connection to the voltage signal, S, Formula (5.4) has to be extended by the absolute intensity calibration of the detector, R_{abs}, and

a unitless factor accounting for the variable electronic gain, G (cf. chapter 4). This step allows the definition the system response function, R, where the two additional factors are concentrated in C_F.

$$\begin{aligned} R &= R_{\text{abs}}\, G\, R^* \\ &= C_F\, R^* \end{aligned} \tag{5.5}$$

Applied to Formula 5.3, the extension leads the left-hand side to become

$$\begin{aligned} S &:= U_{\text{det}}\, G\, R_{\text{abs}} \\ &= U_{\text{det}}\, C_F \end{aligned} \tag{5.6}$$

and the right-hand side to become

$$\begin{aligned} &= Q^2\, |F_{\text{long}}|^2\, C_F\, R^* \\ &= Q^2\, |F_{\text{long}}|^2\, R, \end{aligned} \tag{5.7}$$

which immediately allows the response function to be used to calculate the form factor:

$$\boxed{|F_{\text{long}}|^2 = \frac{1}{Q^2}\,\frac{S}{R}.} \tag{5.8}$$

Since the absolute intensity response of the elements cannot, so far, be treated as known, the evaluation of the data taken with the double-prism spectrometer is qualified to deliver a value

$$|F^*|^2 \;=\; C_F\; |F_{\text{long}}|^2 \tag{5.9}$$

with the unit

$$[|F^*|] \;=\; \sqrt{\text{V J}^{-1}},$$

until the intensity calibration, R_{abs}, is sufficiently known or a cross-calibration with respect to a calibrated spectrometer is conducted. As presented later, the well-understood multi-stage grating spectrometer *CRISP4* [66, 73] has been used to perform comparative measurements.

Referring to section 2.2, the measurement of the spectral distribution of the longitudinal form factor, $|F_{\text{long}}(\lambda)|$, also enables a quantitative assessment of the electron bunch length, even though the absolute value of $|F_{\text{long}}|$ is unknown.

Figure 5.6 shows the partial response function, R^*, as calculated with the code *THzTransport*. Although the underlying model is based on the parameters presented in Table 5.1, measurements during the calibration campaign at the FELIX facility suggested to modify the distance of the detector to the final focusing mirror, $M2$, by an offset of +20 mm. Please refer to section 6.1.4 for details.

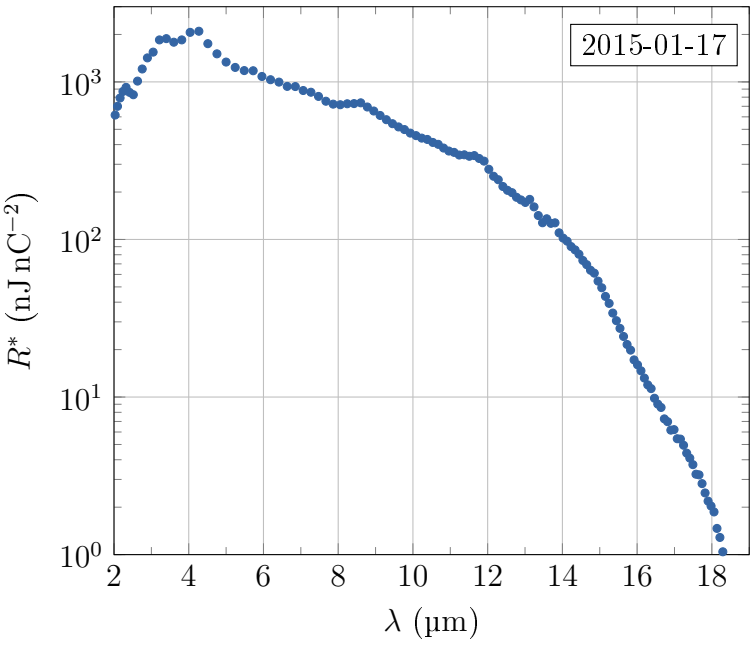

Figure 5.6: Calculated partial response function R^* for the setup at the FLASH facility.

5.4.1 Contributions to the response function

The quantity

$$C_R = T_{\mathrm{HITRAN}}(\lambda)\, T_{\mathrm{W}}(\lambda)\, T_{\mathrm{P}}(\lambda)\, T_{\mathrm{mirrors}}(\lambda)\, R_{\mathrm{relative}}(\lambda) \tag{5.10}$$

in the partial response function accounts for several corrections for transmissive and reflective losses of the optical elements between the CTR source and the detector. The Table 5.5 presents a synopsis of the correction factors, whereas the factors T_{W} and T_{P} combine the contributions of reflective losses at the material interfaces and transmissive losses due to absorption in the material.

The calculation of the factors is presented in the following.

$$\begin{aligned} T_{\mathrm{W}}(\lambda) &= T_{\mathrm{window}}(\lambda)\, \mathfrak{T}_{\mathrm{window,\ front}}(\lambda)\, \mathfrak{T}_{\mathrm{window,\ back}}(\lambda) \\ T_{\mathrm{P}}(\lambda) &= T_{\mathrm{prism\ 1}}(\lambda)\, \mathfrak{T}_{\mathrm{prism\ 1,\ front}}(\lambda)\, \mathfrak{T}_{\mathrm{prism\ 1,\ back}}(\lambda) \\ & \quad\ T_{\mathrm{prism\ 2}}(\lambda)\, \mathfrak{T}_{\mathrm{prism\ 2,\ front}}(\lambda)\, \mathfrak{T}_{\mathrm{prism\ 2,\ back}}(\lambda) \end{aligned} \tag{5.11}$$

Table 5.5: Overview on the contributions in the response function, which all yield values in the domain $\mathbb{R}$, $[0, 1]$.

factor	description
T_{HITRAN}	transmission, ambient air, $d = 3.1$ m
T_{window}	transmission (bulk) ZnSe of the vacuum window, $d = 3$ mm
$T_{\mathrm{prism\ 1,2}}$	transmission (bulk) ZnSe of the prisms, $d = 2 \cdot 15.5$ mm
$\mathfrak{T}_{\mathrm{front}}$	transmission (Fresnel) at the transition air/vacuum - ZnSe
$\mathfrak{T}_{\mathrm{back}}$	transmission (Fresnel) at the transition ZnSe - air/vacuum
T_{mirrors}	reflectance, losses at the mirrors

IR absorption in air, T_{HITRAN}. In the case of the setup at the FLASH facility, the optical path from the transition radiation source to the detector head includes 3.1 m of ambient air with a wavelength-dependent absorption. The *HITRAN* (High Resolution Transmission) database [138] has been used to model the transmission of mid-IR radiation through air. The data according to the model "IAO, mean latitude, summer, H=0" [139] for the temperature of 295 K and optical path length of 1 m was accessed on the 2nd of July 2014 via [140]. Figure 5.7 depicts the transmission spectrum.

ZnSe absorption, $T_{\mathrm{prism\ 1,2}}$ and T_{window}. The reference [141] summarises an investigation of the absorption coefficient of zinc selenide in the spectral range between 2 µm and 20 µm. The authors state that at wavelengths below approx. 10 µm, surface effects, which strongly depend on the surface treatment, dominate the absorption processes and cannot be adequately described by a generally valid model. Above approx. 10 µm, the bulk absorption dominates and allows modelling using a polynomial fit. The polynomial [141, Equation

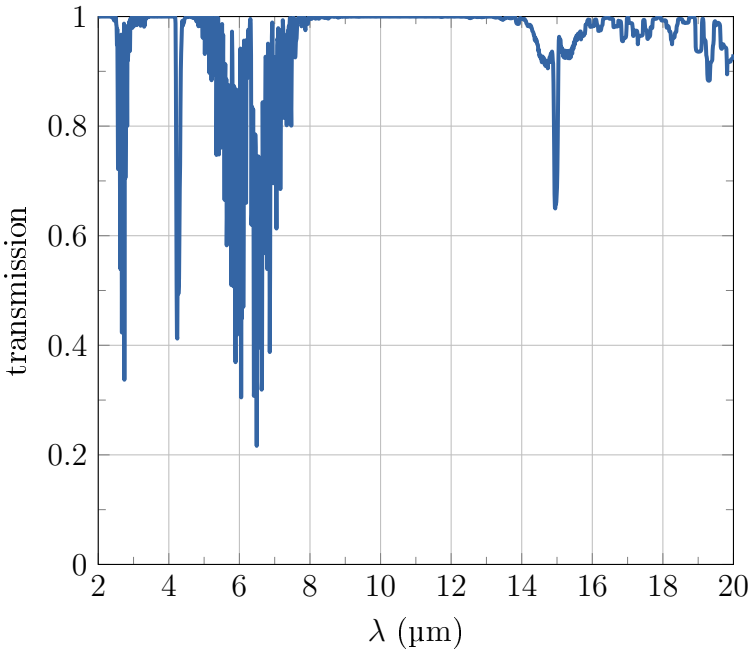

Figure 5.7: Relative transmission of mid-infrared radiation through 1 m of air according to the *HITRAN* database.

(13)] and the corresponding parameters are employed in the bulk transmission correction factors $T_{\text{prism1,2}}$ and T_{window} in the partial response function R^*.

Figure 5.8 presents the modelled bulk transmission for a material thickness, $d = 5\,\text{mm}$, and the total correction including the reflective losses following the Fresnel formulae (eqn. (3.15)) at the entrance and exit surface of the material. The vertically extended spectrometer slit acts as a spatial polarisation filter of the transition radiation with a wavelength-dependent efficiency. The wavelength-dependent transmission of the vertical polarisation, perpendicular to the plane of incidence, and the polarisation parallel to the plane of incidence have been taken into account.

In addition, example transmission data available from *Korth Kristalle GmbH* [125, with permission, web page accessed on 9th of April 2015] are included in the depiction. The data points (*green*) originate from an example measurement where no further details are available on the procedures and light polarisation. Therefore, the comparison of the model to the measurement is considered as a verification of the characteristics in the transmission distribution only. Only the characterisation of the installed ZnSe samples in a dedicated calibration

campaign can satisfy the requirement of an accurate treatment of the transmission. Until the campaign, the uncertainties can be regarded as an addendum to the factor C_F, which accounts for the unknown absolute intensity calibration.

Despite these limitations, the modelled transmission is in good agreement with the distribution indicated by the data points.

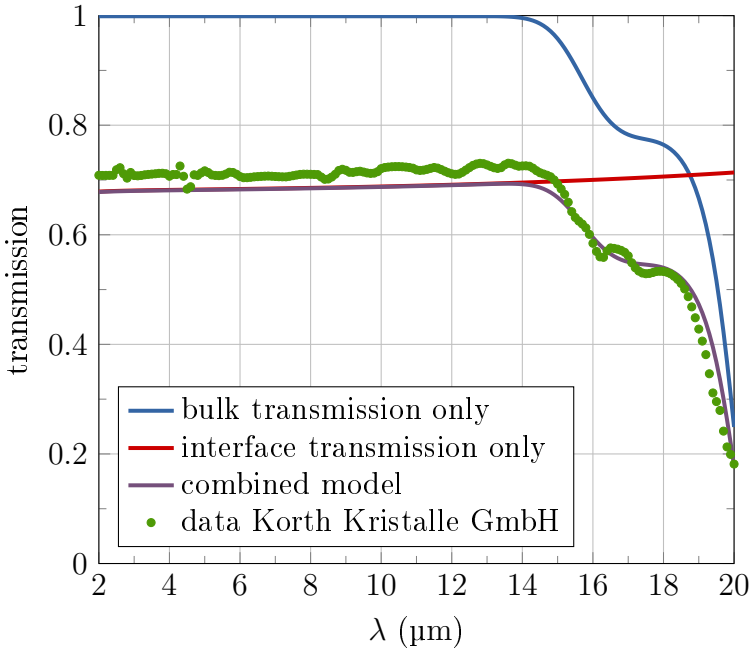

Figure 5.8: The utilised model following [141] for the bulk transmission of zinc selenide with optical length $d = 5\,\mathrm{mm}$ (*purple*). The *blue* trace represents the bulk absorption only, whereas the reflective losses at the two surfaces, for the polarisation perpendicular to the plane of incidence, are included in the *red* distribution. In addition, data provided by *Korth Kristalle GmbH* are depicted in *green*.

Reflective losses at the ZnSe surfaces, $\mathfrak{T}$. In addition to the medium itself, the electro-magnetic wave of the transition radiation pulse has to propagate through the boundaries between the vacuum system and a zinc selenide window (see appendices A and B for details) and the transitions air-ZnSe-air for the two prisms. A fraction of the electric field and thus, of the intensity, is reflected. The results, depicted in exemplary Figure 5.8, are derived from the formulae (3.13), (3.14) and (3.15), which are introduced in section 3.4. Since

the transverse extension of the transition radiation beam on the slit depends on the wavelength, the transmission efficiency of the polarisations s and s was determined with an assessment using *THzTransport* [106].

Reflective losses at the mirrors, T_{mirrors}. The transport of the transition radiation from the source to the double-prism spectrometer involves several plane and focusing mirrors. Whereas Table 4.5 gives an overview of the mirrors utilised in the spectrometer, the arrangements at the FLASH facility and at the ASTRA-GEMINI laser facility are depicted in the appendices A.3 and B.

Accounting for the losses due to the limited reflectance of the mirror depends on the material of the mirror substrate and coating, but also on the surface quality regarding roughness and defects. Since reflectance measurements for each mirror are not available, the following values, which are based on examples provided by [126], have been used in the data analysis.

Table 5.6: Overview of the mirror reflectance used in the response function.

substrate	coating	reflectance
aluminium	protected aluminium	0.97
aluminium	protected gold	0.98

Electronic gain factor, G. As introduced in chapter 4, the integrator in the detector electronics allows the selection of 16 gain settings by remotely-selectable capacitors [95]. Table 4.2 in chapter 4 presents the available settings of the integrator capacitor and the electronic gain factor, G. The measurements presented in this thesis are, if not otherwise specified, acquired in the *high-gain mode*.

Relative detector response, R_{relative}. The treatment of the wavelength dependent response of the detector system is currently only possible on the basis of data provided by the manufacturer [110]. Normalised data for 17 detector elements are available, which are depicted in Figure 4.4 in chapter 4. The wavelength-dependent mean is used as the relative wavelength response of the detector , $R_{\text{relative}}(\lambda)$. An estimation of the relative and absolute response

of the spectrometer was found from results from the calibration campaign at FELIX (see section 6.1).

5.5 Data treatment and analysis

The detector voltage signal can be transferred, with the calculated response function R^*, into a quantity $C_F\ |F_{\mathrm{long}}|^2$. The raw data, sets of 128 voltage values for each single shot, are evaluated in a process described below in order to account for baseline offsets, background level fluctuations (noise) and statistical significance. A synopsis of the procedure is depicted in the flow chart in Figure 5.10.

The single-shot spectra, $S = S(\#)$ with the unit $[S] = \mathrm{Volt}$, are corrected for offsets introduced by the readout system and thermal background radiation. This is facilitated with subtracting the baseline, $\overline{S_{\mathrm{bg}}}$, which is the mean of several hundreds of spectra acquired with the closed spectrometer slit. The amplitude of the baseline is approx. 151 mV, whereas the dynamic range of the data acquisition system is $(0-5)\mathrm{V}$.

The square modulus of the form factor, $C_F\ |F_{\mathrm{long}}|^2$, is calculated following formula (5.8) for the mean of the detector element signals as well as for the r.m.s. of the mean value of the baseline, $\overline{\sigma_{\mathrm{bg}}}$.

The latter is used in a significance test of the detector signals. The mean signal of a single detector element is considered to be significant and valid for the further evaluation, if it exceeds the noise-equivalent form factor (NEF), which corresponds to $6\,\overline{\sigma_{\mathrm{bg}}}$. Detector elements providing mean signals below this threshold are omitted.

By convention, the results are presented in the form $\sqrt{C_F}\ |F_{\mathrm{long}}|$.

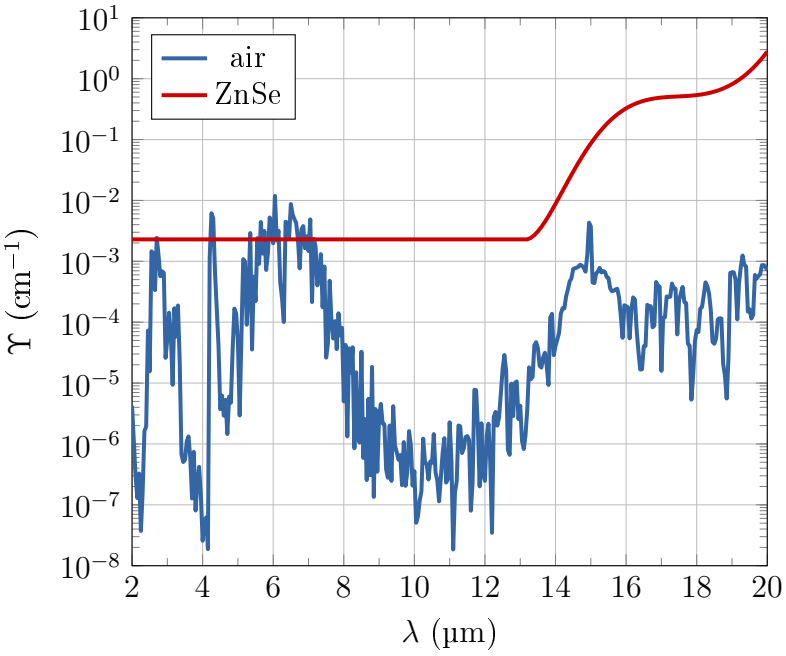

Figure 5.9: Absorption coefficient, Υ, for air and zinc selenide. Please refer to the text for details.

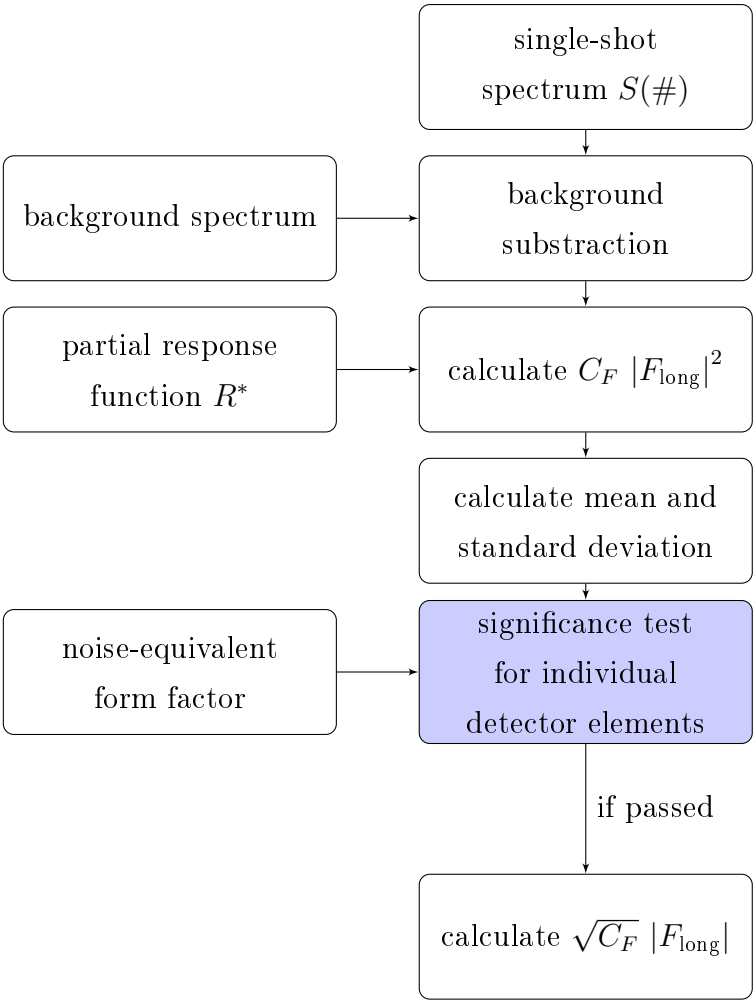

Figure 5.10: Flow chart of the data analysis.

6 Measurements

After the introduction of the design and the characterisation, as well as the procedure of the data analysis, in the previous chapters, the chapter at hand presents measurements with the double-prism spectrometer. First, the results of a calibration campaign at the free-electron laser facility FELIX are discussed. Second, measurements taken at the transition radiation source at the FLASH facility are depicted in detail, assessed and compared to another diagnostic device. Finally, a discussion addresses uncertainties and errors of the measurements.

As indicated in chapter 5, the scientific software MATHEMATICA [107] and MATLAB [142] were used for the data analysis.

6.1 Calibration campaign

The calculation of the distribution and moreover, the absolute value of the longitudinal form factor, $|F_{\mathrm{long}}|$, requires a detailed knowledge of the partial response function, R^*, and the absolute voltage response, $R = C_F\, R^*$.

In order to confirm the calculated partial response function (cf. section 5.4) and to determine the intensity calibration of the double-prism spectrometer, a measurement campaign was conducted at the infrared FEL facility FELIX (The Free Electron Laser for Infrared eXperiments) in Nijmegen (The Netherlands) [128].

6.1.1 The FELIX facility

The free-electron laser facility FELIX delivers bursts of radiation pulses with wavelengths from approx. 6 µm to 150 µm. A normal-conducting linear accelerator delivers electron bunches of up to 45 MeV, which drive two free-electron laser oscillators (FELO) for wavelengths in the ranges from approx. 6 µm to 45 µm

and 35 µm to 150 µm respectively. The centre wavelength can be remotely tuned by altering the undulator parameter, K, via the undulator gap height [128, 143].

The light is extracted from the optical cavity via an aperture in one of the folding mirrors. A diagnostic station with an online grating spectrometer, a pyroelectric detector and a set of remotely selectable attenuators with strengths from 0 dB to 38 dB, is followed by an evacuated beam transport system to the user station. The attenuators are based on free-standing transmission gratings and are commercially available from Lasnix [144, mod. 102 and 224]. A caesium iodide (CsI) window separates the user station from the beam transport system, that is sealed towards the accelerator vacuum by a diamond window.

During the beam time in August 2015, a dedicated setup was installed at the user station - Figure 6.1. An additional set of attenuators increased the total range in available attenuation to 72 dB. A subsequent arrangement of movable mirrors distributed the infrared beam either to the grating spectrometer *CRISP4*, to the double-prism spectrometer *2-PRISM* or to a thermal radiation power sensor (mod. Ophir Optronics 3A-P-THz). With the exception of the double-prism spectrometer, which is operated behind a zinc selenide window, the attenuator and beam distribution setup were able to be operated in vacuum [145].

The facility provided bursts of radiation pulses with a spacing of 1 ns and a burst length of approx. 6 µs. The burst repetition rate was $f_{\mathrm{burst}} = 10\,\mathrm{Hz}$.

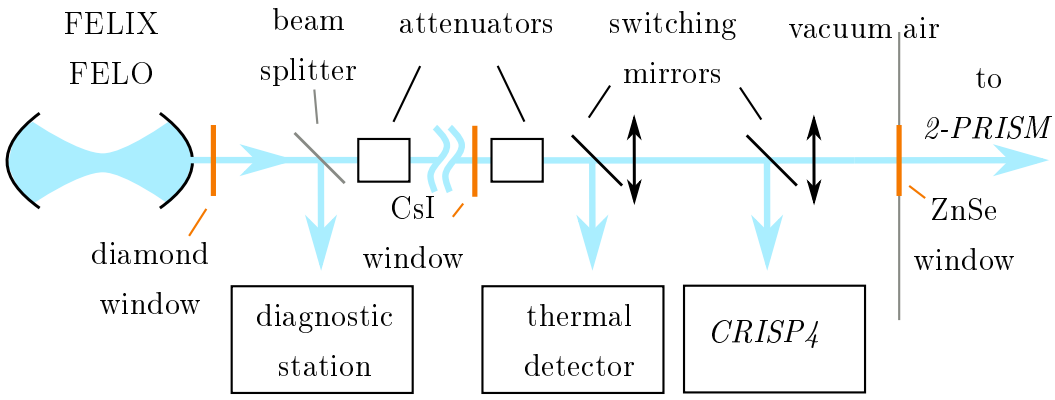

Figure 6.1: Simplified schematic of the setup during the calibration campaign. The diagnostic station, the attenuators and the switching mirrors on motorised stages are remotely controlled.

6.1.2 Wavelength calibration

The wavelength calibration of the spectrometer for operation at the FLASH facility is, as shown in section 5.2.1, conducted with band pass filters. At the FELIX facility, a scan of the FELO wavelength enabled the investigation of the validity of the procedure with band pass filters.

Figure 6.2a presents, as an example, the MCT detector signal, S, for the FELO wavelengths $\lambda_j = 10.2\,\mu m$ and $14.6\,\mu m$. The traces were acquired with the electronic gain $G = 8/3$ and rescaled to the maximum gain, $G = 16$ (cf. Tables 4.2 and 5.4), which will also be used as a convention for the following depiction. The element number corresponding to the FELO wavelength set point was determined by approximating Gaussian functions to the detector readings of each wavelength step.

Figure 6.2b compares the results from this assessment to a calibration function calculated from the positions of the band pass filters taken on the 23rd of November 2014.

A fit, performed according to section 5.2.1, yielded the parameters presented in Table 6.1. The values show differences compared to the measurements with band pass filters (see Table 5.2 in section 5.2.1), since the four supporting points used in the band pass filter procedure are insufficient for an accurate calculation.

Table 6.1: Optimised parameters in the dispersion function for the data acquired with band pass filters (cf. Table 5.2) and at the FELIX facility (Figure 6.2b).

parameter	unit	value	
		band pass filter	FELIX measurements
angle of incidence α_1	deg	37.5	35
inter-prism angle Π	deg	108	110.5
focal length f_2	mm	166	150
horizontal offset Δx_{offset}	mm	285.9	263.9

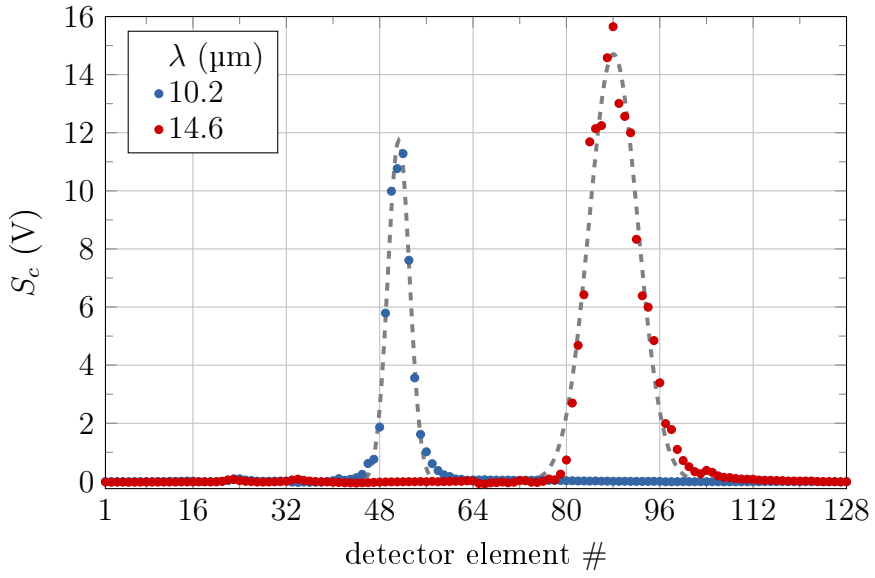

(a) scaled mean detector voltage signal

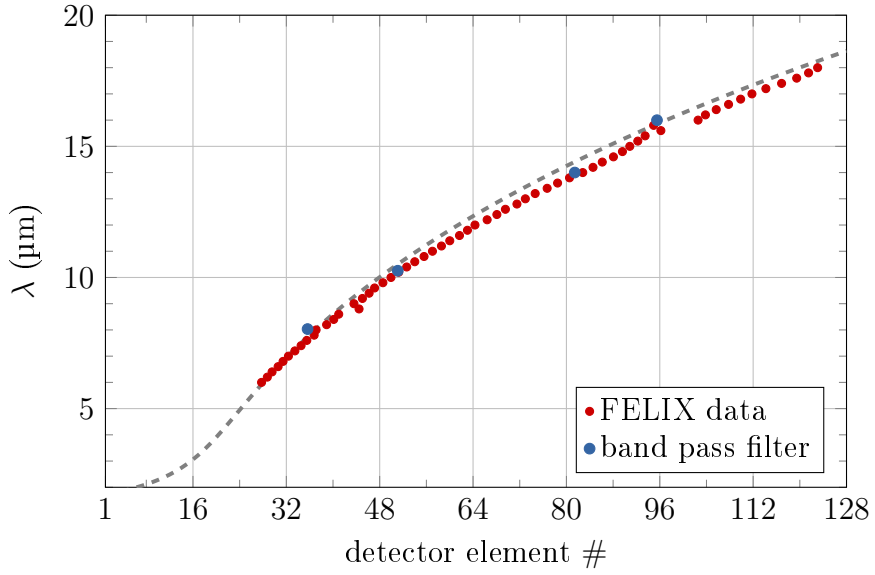

(b) wavelength calibration

Figure 6.2: (a) Examples of detector voltage signals for two FELO wavelengths. The signal amplitudes are scaled to the maximum electronic gain. Gaussian functions (*dashed*) are calculated for each wavelength step to determine the detector element which corresponds to the FELO wavelength. The attenuation of the FELO light was 51 dB. (b) Results of the measurements of the FELO wavelength scan (*red dots*) in comparison to a calibration function (*dashed line*) acquired with band pass filters (*blue dots*).

6.1.3 Intensity calibration

The assignment of a detector signal of an individual element to an irradiated pulse energy can be derived from the comparison of the pulse energy measured at the spectrometer entrance and the evoked voltage signal of the MCT detector, which have to be acquired in two consecutive wavelength scans.

The radiation energy of one burst, $U_{\mathrm{burst}}(\lambda_j)$, was determined from the power measurement with the thermal power detector (Ophir Optronics 3A-P-THz), that was closely placed after the focusing mirror $M0$ (cf. Figure 4.15):

$$U_{\mathrm{burst}}(\lambda_j) = P_{\mathrm{burst}}(\lambda_j)\, f_{\mathrm{burst}}^{-1} \;=\; \frac{\mathrm{d}\,U}{\mathrm{d}\,\lambda}\,\Delta\lambda_{\mathrm{FELO}}, \tag{6.1}$$

where P_{burst} is the power measurement from the detector head at the FELO centre wavelength, λ_j, and the corresponding spectral bandwidth, $\Delta\lambda_{\mathrm{FELO}}$. The spectra taken with the online spectrometer of the FELIX diagnostic station show that the spectral bandwidth of the FELO is below 1 % and thus, smaller than the expected spectral bandwidth of the individual MCT detector elements.

The scan of the FELO wavelength in the range from 5.5 µm to 19 µm and the respective pulse energies are depicted in the blue trace in Figure 6.3a. Here, the readings of the thermal power sensors were recorded by hand. The statistical uncertainty of the measurements was estimated via a dedicated wavelength scan, where a digitised data acquisition was available. Regarding 50 shots on average for the individual wavelength steps, the single-shot r.m.s. deviation from the mean is estimated to be 0.5 mJ.

At electronic gain setting $G = 8/3$, the radiation power needed to generate signals of the MCT detector close to saturation was lower by the factor $\approx$ 6300 (38 dB) than the level needed for the power measurements with the thermal detector.

For the further analysis, the pulse energy measurements are corrected for the fact that the temporal width of the integrator gate of the MCT electronics is shorter than one radiation burst of the FELO. The temporal power build-up of one radiation burst was monitored with a pyroelectric detector in the diagnostic station. The fraction of the burst that was covered by the integrator gate of 2.5 µs length was determined to be 22 %.

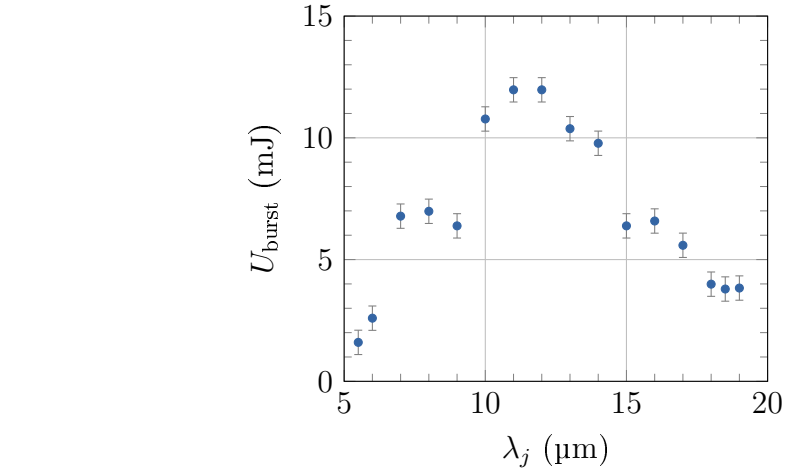

(a) pulse energy

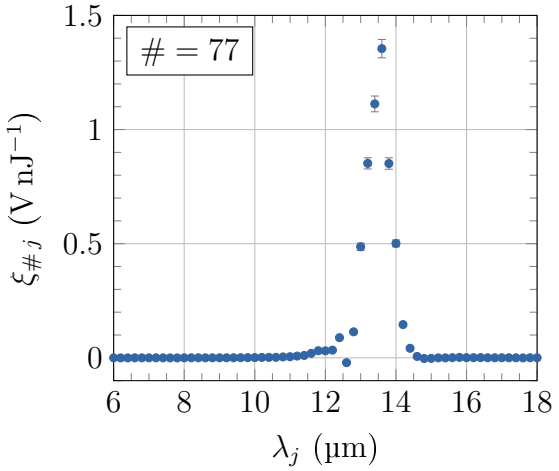

(b) entries of the row for element 77 of matrix Ξ

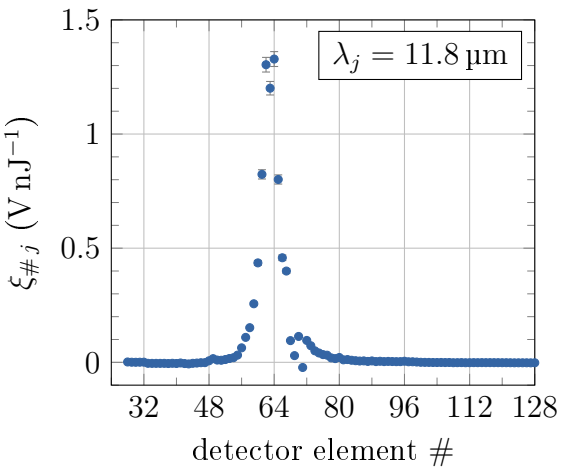

(c) column 30 of matrix Ξ

Figure 6.3: (a) Scan of the pulse energy of the FELIX FELO acquired with a power detector. Whereas the measurements were taken at attenuator settings of 10 dB and 13 dB, the depicted values are scaled to zero attenuation. The statistical uncertainty of the measurements was estimated to 0.5 mJ. This data set is used for the data analysis. (b) Entries of the row of response the matrix, $\Xi = (\xi_{\#\,j})$, that correspond to detector element 77. (c) Matrix entries of column 30. These entries represent the step response of the spectrometer for an incident spectrum consisting of a single narrow line at $\lambda_j = 11.8\,\mu\mathrm{m}$.

Response matrix

As depicted in Figure 6.2a, the spectral distribution of the FELO pulse is translated into a voltage signal distribution on the MCT detector which involves more than one detector element. Since the spectral bandwidth of the FELO is small compared to the spectral bandwidth covered by one detector element, this behaviour can be explained by a transverse beam profile that covers the area of more than one detector element.

In consequence, the spectrometer response is expressed as a transformation matrix, $\Xi = (\xi_{\#\,j})$, which translates an incident energy spectrum, $U(\lambda)$, into a signal distribution of the detector elements, $S(\#)$:

$$\vec{S} = \Xi\,\vec{U}, \tag{6.2}$$

where $\vec{S}$ and $\vec{U}$ represent the entities of the considered detector elements and discrete wavelength positions within the incident radiation spectrum respectively.

The matrix elements, $(\xi_{\#\,j})$, are column-wisely populated with data from the calibration campaign as follows:

The vector, $\vec{U}$, consists of only one non-zero element equalling the measured pulse energy, $U_{\mathrm{burst}}(\lambda_j)$, for each FELO wavelength step, λ_j. The vector, $\vec{S}$, is the distribution of the voltage signals of the individual elements, #. Hence, the matrix elements of the j^{th} column can be calculated for each detector element via

$$\xi_{\#\,j} = \frac{S_c(\#)}{U_{\mathrm{burst}}(\lambda_j)}, \tag{6.3}$$

where the detector signals, $S(\#)$, that were acquired at gain setting $G = 8/3$ are scaled to the maximum electronic gain, $G = 16$, $S_c(\#) = 6\,S(\#)$.

During the calibration campaign, 61 FELO wavelength steps, λ_j, with $\lambda_1 = 6\,\mu\mathrm{m}$, $\lambda_{61} = 18\,\mu\mathrm{m}$ and $\lambda_{j+1} - \lambda_j = 0.2\,\mu\mathrm{m}$, were acquired. The range of interest in detector elements was restricted to the interval $\# \in [28, 128]$, since the wavelength range of the spectrometer begins at approx. $2\,\mu\mathrm{m}$.

The resulting matrix yields the dimensions $(\# \times j) = (101 \times 61)$. Figure 6.4 visualises the matrix entries, whereas Figures 6.3b and 6.3c show the row 50, that corresponds to element 77, and column 30 ($\lambda_{30} = 11.8\,\mu\mathrm{m}$) of the matrix.

The matrix now reflects the response of the spectrometer for 61 narrow spectral lines according to the FELO wavelength scan. A correspondent matrix exists for the uncertainties of the entries of Ξ.

The expected signal of the spectrometer for a flat spectrum consisting of spectral lines $U\,\delta(\lambda - \lambda_j)$ with $U = 1\,\mathrm{nJ}$ at the wavelengths of the FELIX wavelength scan, λ_j, can be found in Figure 6.6a.

The number of supporting points is given by the number of columns in the response matrix, Ξ. In order to treat a non-constant continuous spectrum correctly, the number of supporting points is increased by a row-wise interpolation of Ξ with the software MATHEMATICA. In the case of an incident continuous spectral energy density, $\frac{\mathrm{d}\,U}{\mathrm{d}\,\lambda}$, the sampling interval of Ξ, $\Delta\,\lambda$, has to be taken into account such that $U = \frac{\mathrm{d}\,U}{\mathrm{d}\,\lambda}\,\Delta\,\lambda$.

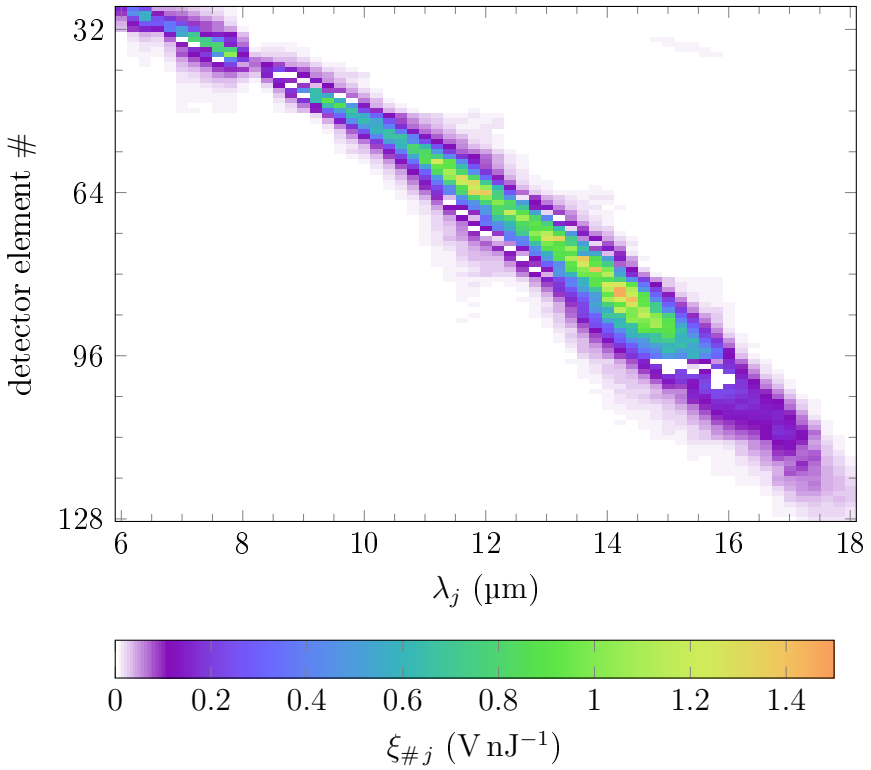

Figure 6.4: Visualisation of the elements of the transformation matrix, $\Xi = (\xi_{\#\,j})$, that were calculated from the voltage distributions of the MCT detector and energy measurements of the incident radiation pulses as measured at FELIX.

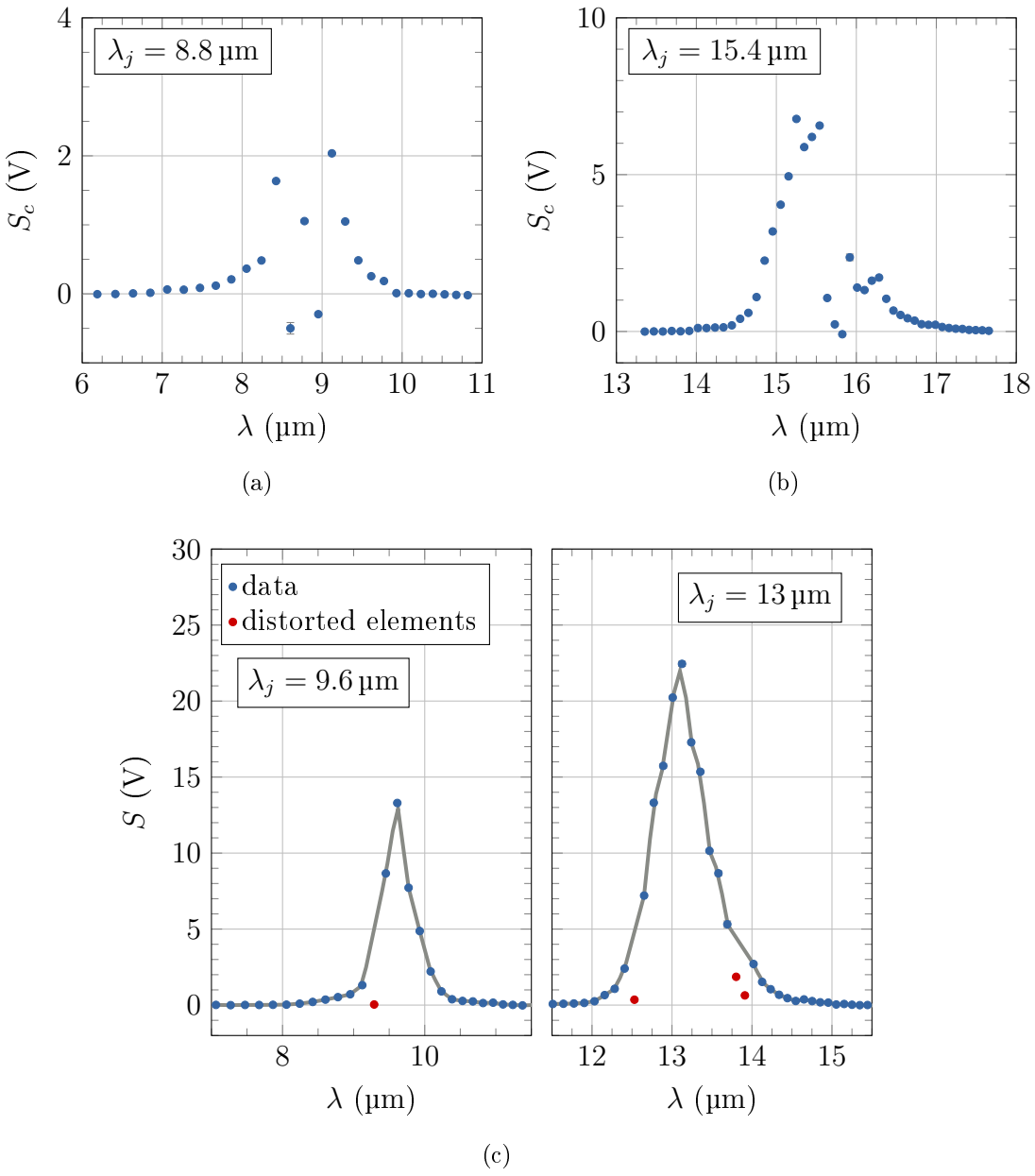

Figure 6.5: Detector element signal distributions for two FELO wavelength steps. (a) and (b): The affected elements disqualify the determination of a justifiable distribution shape. (c): For λ_j between 9.6 µm and 13 µm, the omission of distorted signals (*red points*) does not affect the specification of the distribution shape. The solid lines correspond to linear interpolations as calculated with the software MATHEMATICA with omitting the distorted signals.

Distorted detector signals

However, the voltage signal distributions, $S(\#)$, yield a number of detector elements that show a distorted signal. The voltage reading of the affected elements are reduced and drop out of a smooth distribution. The amplitude is partially below the baseline, i. e. the voltage level when no radiation is exposed to the detector. Figure 6.5 presents two examples of distorted signals, which are also visible in the matrix, Ξ (Figure 6.4), as *white points*. The location of affected elements is not constant. This circumstance partly prohibits a reliable determination of the evoked detector signal for the calculation of the response function. An insufficient electrical connection to the ground and optical cross talk of elements in the 16-element groups were identified before the calibration campaign, where the former could be improved by the manufacturer in early 2015 via additional grounding. The optical cross talk is a feature of the detector [146]. Albeit further studies and countermeasures on this behaviour are required, the dispersive properties of the spectrometer are not affected.

Nonetheless, the measurements taken at the FELIX facility can be used for a further analysis, where affected single elements can clearly be identified to be distorted by the detector system and an omission does not change the shape of the distribution. Whereas the distortions shown in Figure 6.5a and 6.5b do not allow the determination of a justifiable shape or integral of the distribution, the range of λ_j between 9.6 µm and 13 µm is still eligible for the analysis of data taken at FELIX. An omission of the affected elements does not change the shape of the distribution - cf. Figure 6.5c. Interpolated voltage amplitudes at the affected element positions following the *grey traces* in Figure 6.5c were used as substitutes. The deviation in the integrals of the distributions with and without omission of the affected elements is $\lesssim 12\,\%$ for $\lambda_j \in [9.6\mu\text{m}, 13\mu\text{m}]$. Not more than four elements were omitted in the particular distributions for FELO wavelength positions in the given interval. The Figure 6.6 indicates the effect of the omission of distorted elements in the range between 9.6 µm and 13 µm. The distinct discontinuities between 8 µm and 9 µm and above 14 µm are related to this issue.

Data acquired at the FLASH facility, that is depicted in the next section, was taken before the calibration campaign and does not show such a pronounced behaviour. The data has still to be assessed under this constraint.

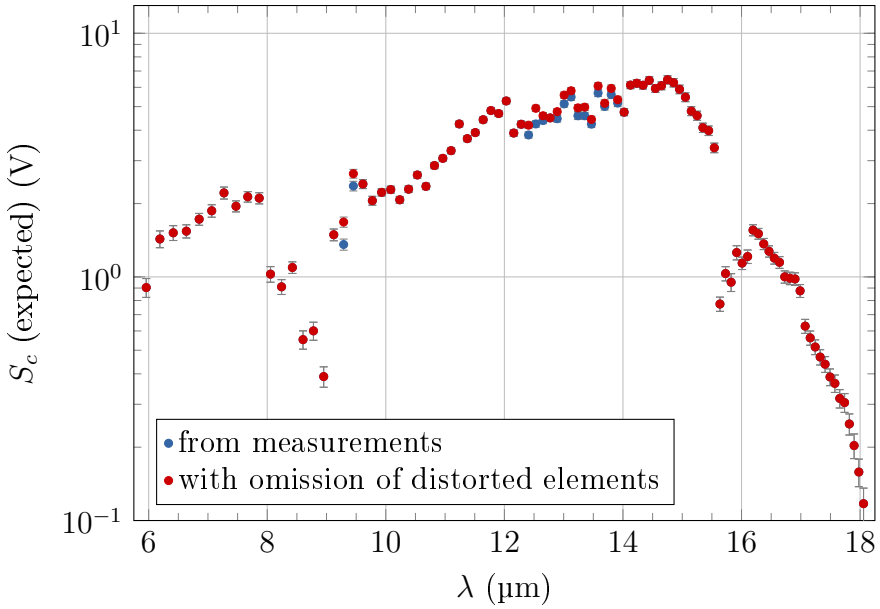

(a) artificial flat spectrum response

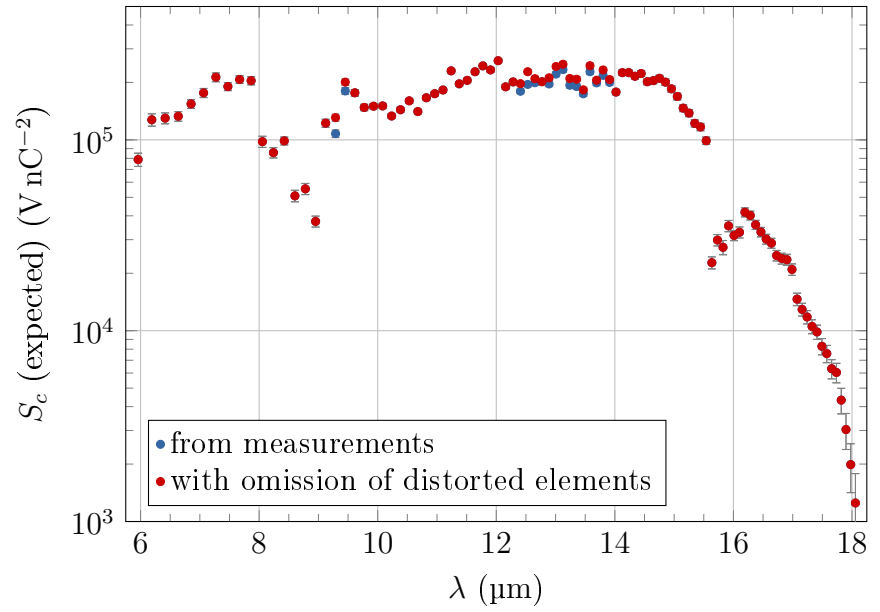

(b) response for a transition radiation with $F_{\text{long}} = 1$

Figure 6.6: (a) Expected voltage signals, S_c, for a flat spectrum, as calculated from the matrix, Ξ. (b) Expected voltage signals for transition radiation. Distorted element signals (see text for details) were omitted in the interval $\lambda_j \in [9.6\text{µm}, 13\text{µm}]$ for the calculation of the *red traces*, whereas the *blue traces* contain these elements.

Application at the FLASH facility

For the application at the FLASH facility and transition radiation, the expected spectral energy density of transition radiation that is exposed to the spectrometer entrance aperture, $\frac{\mathrm{d}U}{\mathrm{d}\lambda}\big|_{\mathrm{slit}}$ was calculated with the code *THz-Transport* [106] for a transversally Gaussian shaped bunch with $\sigma_{\mathrm{trans}} = 200\,\mu\mathrm{m}$ and $|F_{\mathrm{long}}(\lambda)| = 1$ in analogy with the treatment in section 5.4. The transmission of the ZnSe vacuum window and the additional beam path in ambient air (1140 mm, cf. section 5.4.1), denoted by T_{W} and T_{HITRAN} respectively, are considered.

The matrix, Ξ, was interpolated to the dimensions $(\# \times j) = (101 \times 1201)$ for wavelengths between 6 µm and 18 µm and $\Delta\,\lambda = 0.01\,\mu\mathrm{m}$ bin width. The resulting voltage signal distribution as calculated with eqn. (6.2) is shown in Figure 6.6b.

The discussion of the obtained results follows in section 6.2.3 after the depiction of the measurements taken at the FLASH facility.

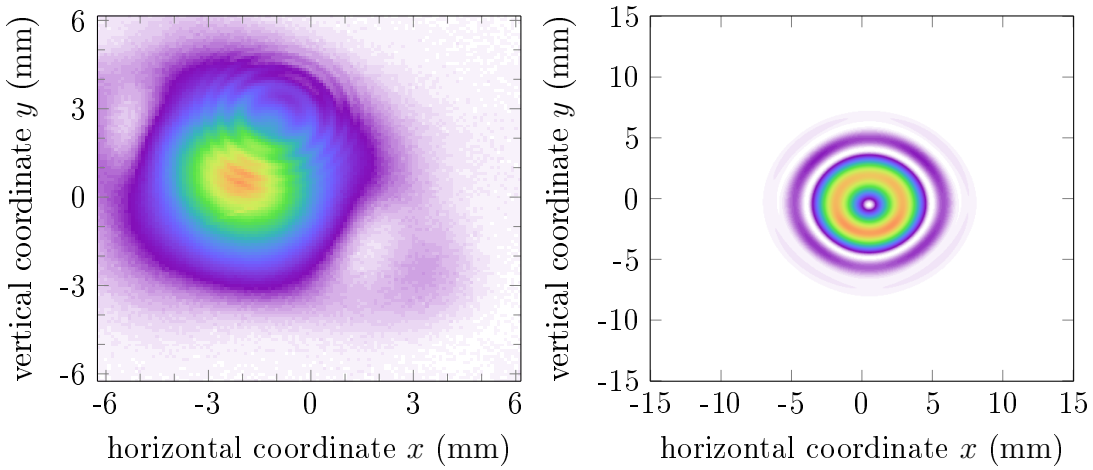

(a) measured transverse profile (b) simulated profile of transition radiation

Figure 6.7: (a): Transverse profile of the FELIX FELO beam ($\lambda = 10\,\mu m$) close to the mirror $M0$ of the double-prism spectrometer, acquired with the camera Ophir Optronics PyroCam III. The distortions of the beam profile predominantly originate from diffraction in the beam transport system and the optical setup. The corresponding simulated profile of transition radiation (b) is cited from Figure 4.16.

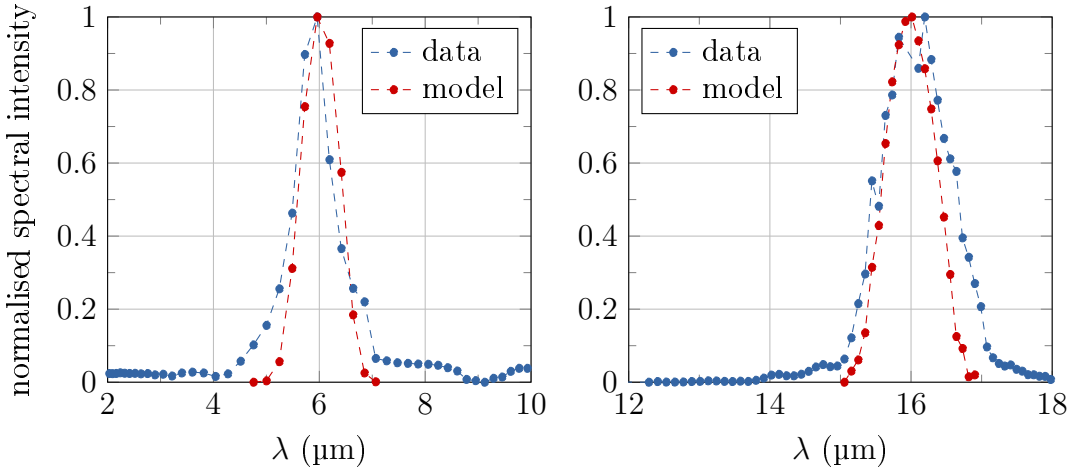

(a) $\lambda_j = 6\,\mu m$ (b) $\lambda_j = 16\,\mu m$

Figure 6.8: Comparison of the measured intensity distributions at two FELO wavelengths at FELIX (*blue*) to profiles that were calculated with *THzTransport* (*red*).

6.1.4 Assessment of the partial response function

The partial response function, R^*, that was introduced in section 5.4, is based on analytical and numerical calculations with the code *THzTransport* [106]. The results depend on a variety of input parameters, such as the spectrometer setup, and on the agreement of the modelled beam path and imaging properties with the actual conditions in the spectrometer.

The narrow-bandwidth FELO beam at FELIX also enabled the investigation of the validity of the modelled radiation transport using *THzTransport*. The measured impulse response, that correspond to the columns of transformation matrix, Ξ, is compared to the calculated spectral distributions. The model was adapted to account for the respective transverse intensity profiles and spot sizes. In contrast to the ring-shaped profile of transition radiation (see section 4.2.3), the profile of the FELO beam is expected to be dominated by the lowest-order Gauss-Hermite mode, which essentially corresponds to a transverse Gaussian profile [15]. A measurement of the intensity profile acquired with a far-infrared camera, that was placed close to the spectrometer mirror $M0$ (cf. chapter 4) is depicted in Figure 6.7.

Comparisons of individually normalised distributions at two FELO wavelengths are presented in Figure 6.8.

The model is based on the geometry depicted in Table 5.1 in section 5.1. However, the distance of the detector to the final focusing mirror, $M2$, had to be increased by 20 mm in order to adjust the modelled intensity distributions in the detector plane to match the measured distributions. Possible unexpected distortions introduced by diffraction of the entrance aperture of the spectrometer could be excluded via studies using a black body source and a thermal imaging camera Infratec VarioCam, but the origin of the offset could not be found during the investigations. Since the dispersed beam after the prisms yields a reduced spatial intensity density, a direct investigation with the thermal imaging camera was not possible. Further studies are advisable, but are beyond the scope of this work.

Nonetheless, the results shown in Figure 6.8 sufficiently match the measured intensity distributions and hereby confirm the validity of the model for the partial response function, R^*.

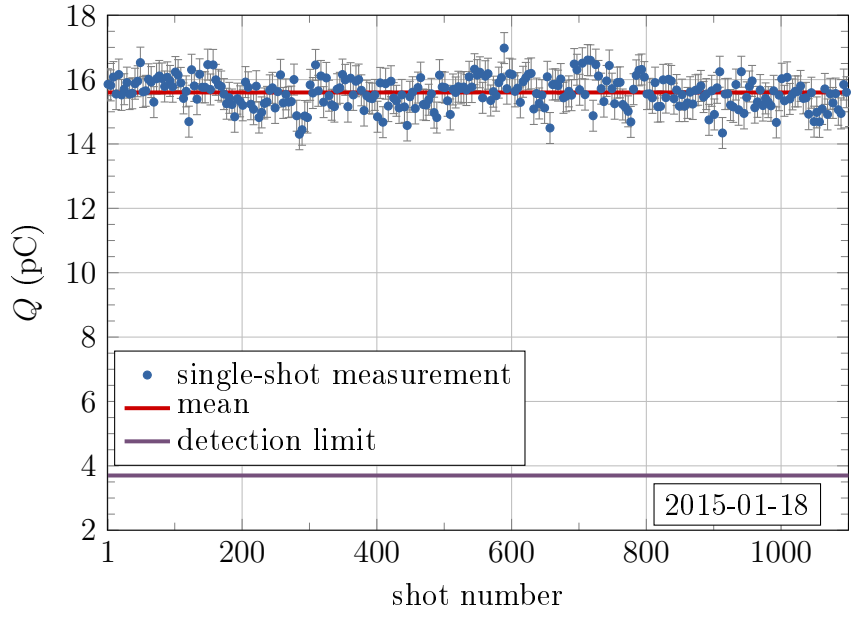

(a) dark current monitor 7DBC2

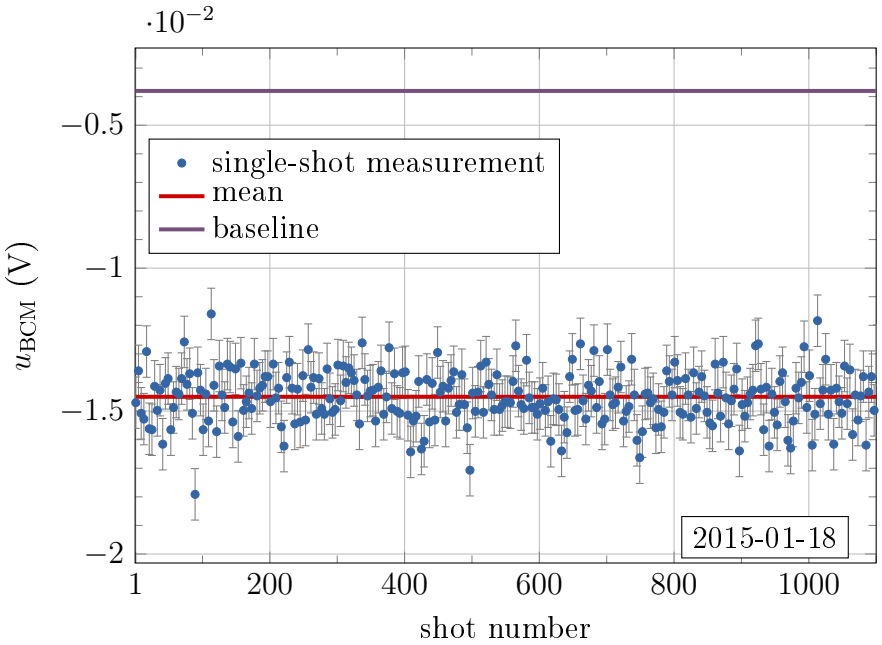

(b) bunch compression monitor 4DBC3.2

Figure 6.9: Readings of the dark current monitor 7DBC2 (a) and the bunch compression monitor (BCM) 4DBC3.2 (b) for 1100 electron bunches. The r.m.s. deviations of the mean are 0.02 pC and 0.03 mV respectively.

6.2 Measurements at the FLASH facility

6.2.1 Prerequisites

The data acquisition system of the double-prism spectrometer does not allow, so far, the direct assignment of a single spectrum to a specific electron bunch (cf. chapter 4). The question of the validity of averaging, say, 1000 spectra shall be answered in these introductory remarks.

The stability of the transition radiation pulses in spectrum and intensity is predominantly determined by the stability of the bunch charge and the compression of the electron bunches that is conducted by RF-induced energy chirps and magnetic chicanes (cf. Equation 2.11 in chapter 2). Figures 6.9a and 6.9b present the total charge per electron bunch, Q, measured with a dark current monitor [133] and the signal of the bunch compression monitor (BCM) 4DBC3.2 [66], located downstream of the second electron bunch compressor. The error bars of the data points correspond to the sample r.m.s. deviation according to formula (D.2).

The results of the statistical evaluation are depicted in Table 6.2. The root mean square deviation of the mean values of the charge measurement and compression monitor are calculated from the entity of 1100 single measurements to be 1 ‰ and 2 ‰ respectively. The short pulse injector laser [147] was used for the measurements.

Thus, the electron bunch charge and compression are considered to be stable for averaging the data of several hundreds of consecutive single-shot measurements.

Table 6.2: Overview of the statistical measures of the dark current monitor and bunch compression monitor readings (Figure 6.9). The evaluation involved 1100 single measurements.

parameter	unit	mean	sample r.m.s.	mean r.m.s.
charge Q	pC	15.6	0.5 (32 ‰)	0.02 (1 ‰)
compression u_{BCM}	mV	−14.5	0.9 (62 ‰)	0.03 (2 ‰)

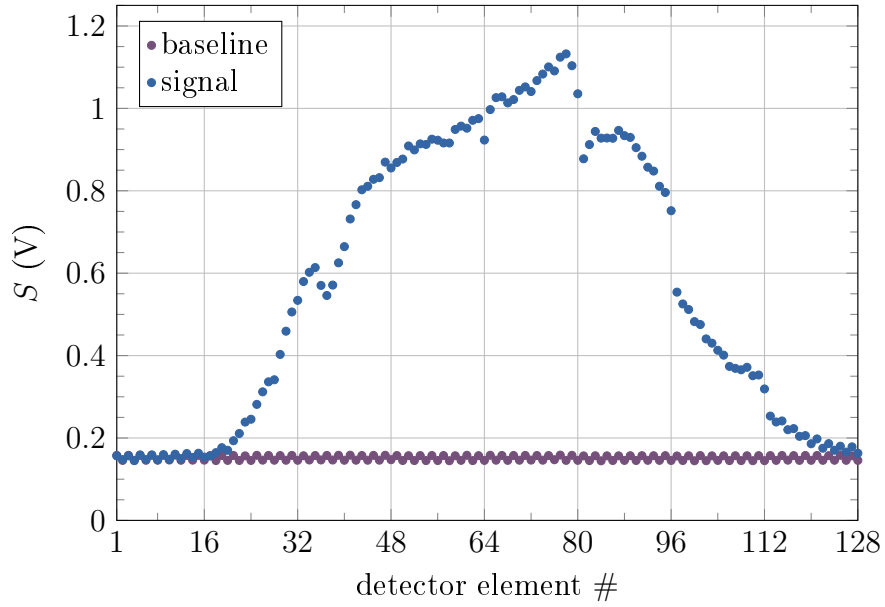

(a) detector raw signal (*blue*) and baseline (*purple*)

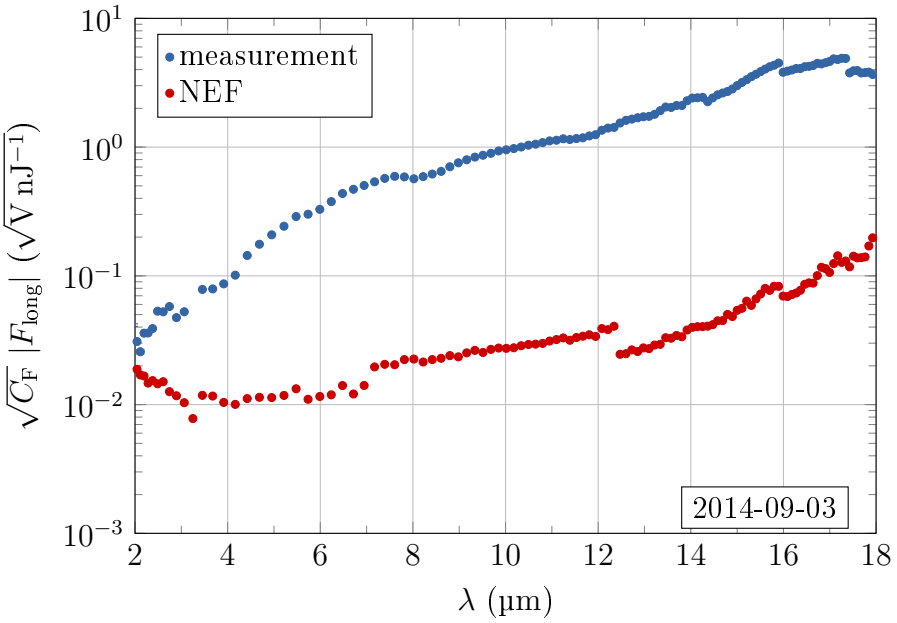

(b) form factor

Figure 6.10: The raw signals (a) are subject to correction for the spectral response and width of the detector elements as well as transmission, that are summarised in the response function, R^*. (b): The form factor, $\sqrt{C_\mathrm{F}}\,|F_\mathrm{long}|$, and the noise equivalent (NEF) are determined via the calculated response function, R^*. The figures show the mean values of 654 single-shot measurements with negligible error bars representing the r.m.s. deviation of the mean.

6.2.2 Raw spectra and form factor measurements

The evaluation of the detector raw spectra, that are voltage readings for the individual MCT detector elements, $S(\#)$, follows the procedure introduced in the chart 5.10 in chapter 5.

Figure 6.10a depicts the mean of 654 single spectra and the corresponding baseline. The overall shape of the voltage signal versus detector element follows the distribution of the partial response function, R^* (cf. section 5.4). In addition, the trace shows distinct discontinuities at elements 80, 96 and 112, which coincide with the arrangement of the detector line in eight groups of 16 elements (please refer to chapter 4). The distortions are related to the insufficient grounding that was mentioned beforehand.

The correction for the spectral response and width of the detector elements as well as for the transmission of the optical system are included in the partial response function, R^*. The adjacent graph (Fig. 6.10b) shows the resulting form factor, $\sqrt{C_\mathrm{F}}\,|F_\mathrm{long}|$, together with the corresponding noise-equivalent form factor (NEF). The NEF is related to the detection limit of the double-prism spectrometer: at a fixed bunch charge, the NEF corresponds to an upper limit in the detectable electron bunch length. This measure is defined as the sixth multiple of the r.m.s. deviation of the mean detector baseline, $6\,\overline{\sigma_\mathrm{bg}}$. Detector signals below this levels are omitted (cf. section 5.5).

The discontinuities in the NEF are also caused by the insufficient grounding, which leads to different noise levels of the eight groups of 16 elements. The bunch charge for this data set was $Q = 41\,\mathrm{pC}$.

The form factor measurements at different accelerator settings are depicted in Figure 6.11. The change in accelerator settings, in this case the electron bunch charge and the settings of the RF system (cf. Table 6.3), lead to a change in the bunch compression, final length and shape.

The comparison of accelerator setting A (*blue*) and B (*red*) in Figure 6.11 shows that a reduction in the bunch charge leads to a lower transition radiation intensity and mean signal-to-noise ratio (see Table 6.3), but can, as depicted, result in a higher form factor, thereby indicating a decrease in electron bunch length.

A measurement at a third accelerator setting is shown in *purple*. The trace yields, in particular between 6.5 µm and 14 µm, a different slope and, compared

to the two others, a distinct feature at $\lambda \approx 8.22\,\mu\text{m}$. Both may signify a change in the bunch shape.

These statements are verified with Figure 6.12, which shows temporal profiles that were calculated from *CRISP4* data for the three data sets mentioned beforehand. The algorithm, that was provided by [148], is based on consecutive Fourier transformations between time and frequency domain (cf. references [70, 72] and section 2.2).

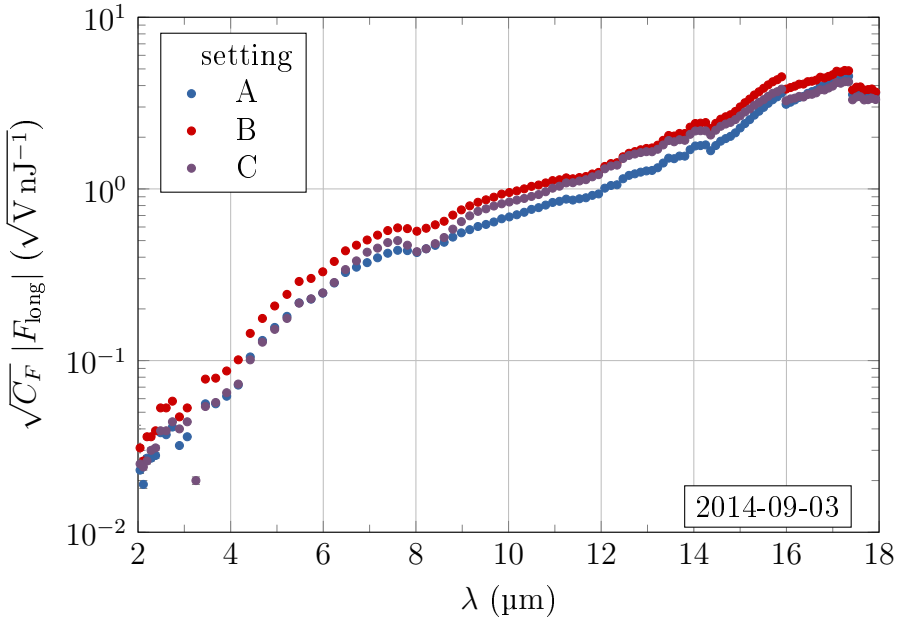

Figure 6.11: Comparison of form factors for three accelerator settings. See text and Table 6.3 for details.

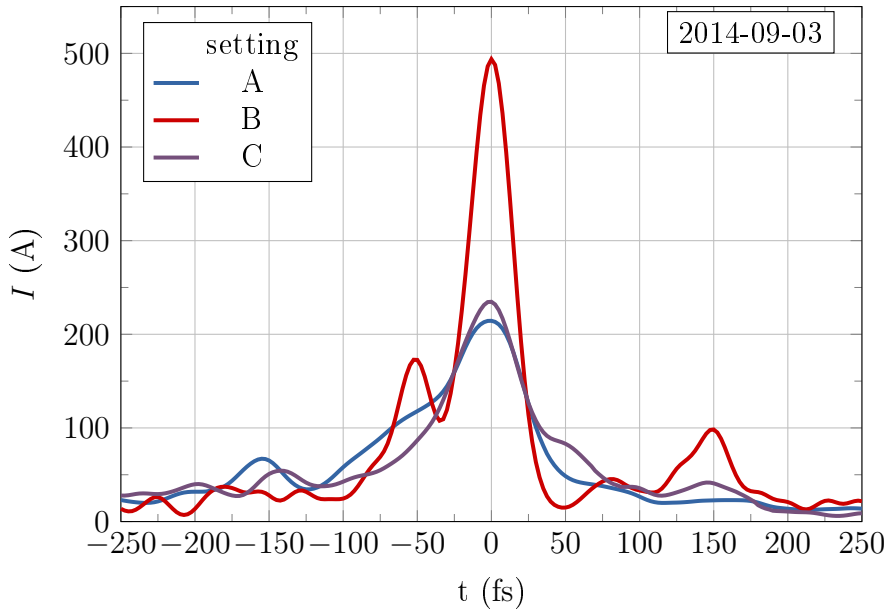

Figure 6.12: Retrieved temporal profiles of *CRISP4* data using an algorithm provided by [148]. The algorithm was used in the "hybrid output-output" configuration with feedback constant $\beta = 0.6$ [70]. The traces correspond to the means of 100 cycles, where each consisted of 100 iterations.

Table 6.3: Overview of the bunch charge, Q, mean signal-to-noise ratio, $\overline{r_{S/N}}$, and phase settings of the accelerating modules for the measurements depicted in Figure 6.11. The r.m.s. deviation of the charge measurements is below 0.1 pC. The signal-to-noise ratio was calculated according to section 5.3.2. The amplitude of the electric field in the accelerating modules was constant.

setting	Q (pC)	$\overline{r_{S/N}}$	ψ_{ACC1} (deg)	ψ_{ACC39} (deg)	ψ_{ACC23} (deg)
A	56	9832 ± 723	3.84	−14.93	18.13
B	41	9172 ± 712	3.83	−14.92	18.13
C	37	6508 ± 543	3.83	−14.88	18.03

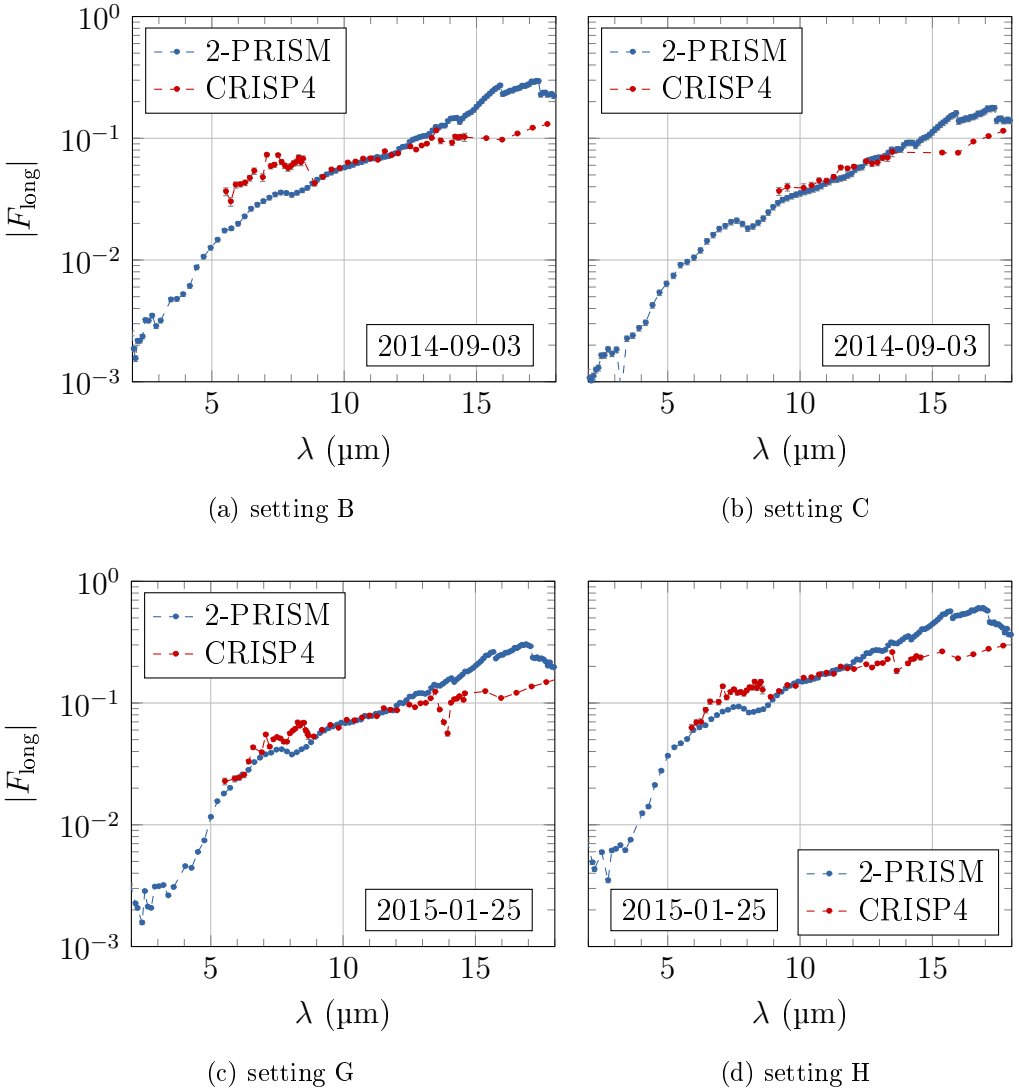

(a) setting B

(b) setting C

(c) setting G

(d) setting H

Figure 6.13: Comparison of the form factor measurements of the double-prism spectrometer, *2-PRISM*, to measurements of *CRISP4*. The traces of the first diagnostic have been scaled to the *CRISP4* data via the scaling constant, C_F. The values of C_F are summarised in Table 6.4.

6.2.3 Comparative measurements

Form factors

The partial response function, R^*, enables the investigation of the form factor evolution with wavelength, which still offers a possibility for the bunch length measurement (cf. section 5.4), but does not, so far, allow the determination of the absolute value of the longitudinal form factor, $|F_{\mathrm{long}}|$. In order to show the validity of the data from the double-prism spectrometer, a comparative assessment with measurements of the four-stage grating spectrometer, *CRISP4* [9], is shown in Figure 6.13. A similar comparison can also be found in [149], whereas reference [73] compares results obtained from *CRISP4* data to measurements with the transverse deflecting structure (TDS) at the FLASH facility.

The scaling constant, C_F, in the measurements of the double-prism spectrometer, $C_F\ |F_{\mathrm{long}}(\lambda)|^2$, was determined via the quotient to the *CRISP4* measurement in the spectral region from approx. 6 µm to 14 µm, where both devices show a high signal-to-noise ratio. The scaling constants for the individual settings are summarised in Table 6.4 and Figure 6.15. The weighted mean according to [68, p. 787] was calculated to be $(351.23 \pm 104.66)\,\mathrm{V\,nJ^{-1}}$. The inverse and squared r.m.s. uncertainties of the values for each setting were used as weight factors.

The comparisons in Figure 6.13 show apparent differences in the form factors of the two spectrometers.

For wavelengths below 9 µm, the trace of the *CRISP4* spectrometer yields a discontinuity, that reoccurs at the same position in several comparative data sets (e. g. Fig. 6.13a and 6.13d). Since the traces of the double-prism spectrometer (*2-PRISM*) do not indicate such a discontinuity, an explanation is seen in a transition between grating stages of *CRISP4*, that is located at approx. $\lambda = 8.7$ µm [9]. As exemplarily indicated in Figure 6.14, the signal-to-noise ratio with respect to the mean value of the *CRISP4* data for wavelengths below $\lambda = 8.7$ µm is just on the order of 10. The trace exhibits visible fluctuations between the data points that correspond to single detector elements. Therefore, the validity of the *CRISP4* data below $\lambda = 8.7$ µm is questionable.

Differences between data of *2-PRISM* and *CRISP4* also occur at wavelengths above $\lambda = 14$ µm. The comparison of the scaled partial response

function, $C_F\, R^*$, to results acquired at the FELIX facility, that is presented in the next section, also indicates a discrepancy in this wavelength range. Since the model for R^* delivers transverse profiles that sufficiently match the measurements at FELIX (see Figure 6.8 in section 6.1.4), an inaccurate description of the spectrometer via the calculated partial response function, R^*, for the setup at the FLASH facility is suspected. A similar behaviour was observed in measurements with band pass filters at the FLASH facility with transition radiation that are mentioned in section 5.2.1. Imaging errors and distortions are pronounced at these wavelengths in comparison to short wavelengths.

The issue of distorted single element signals in the FELIX data adds an additional uncertainty. Although distortions due to insufficient electrical grounding of the detector elements exist, the striking behaviour described in section 6.1.3 was not observed in the data shown here.

The comparison clearly illustrates that the general slope of the form factors derived from the data of the double-prism spectrometer is in agreement with *CRISP4* measurements.

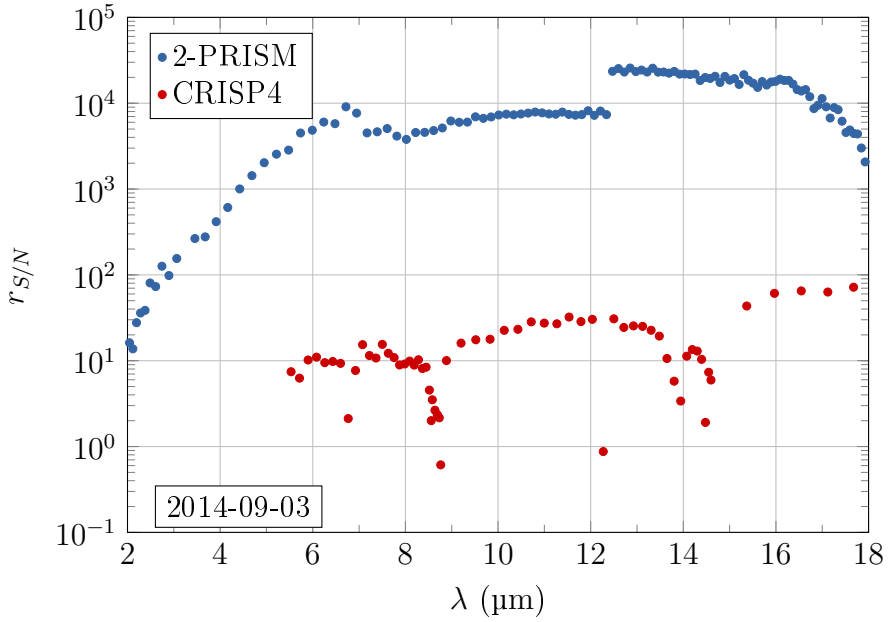

Figure 6.14: Comparison of signal-to-noise ratios of the prism spectrometer (*2-PRISM*) to *CRISP4* with respect to mean vale corresponding to accelerator setting B.

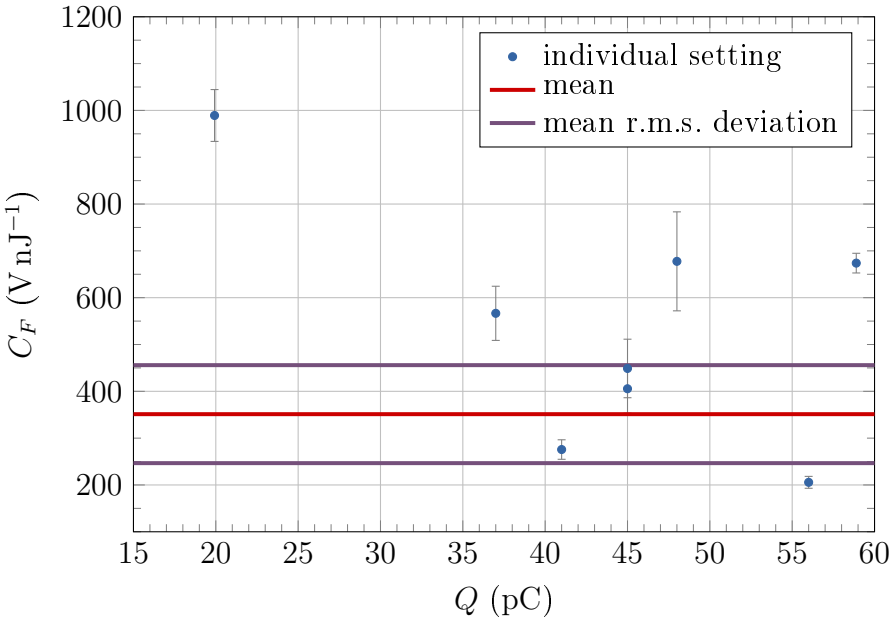

Figure 6.15: Visualisation of the scaling constants, C_F, as summarised in Table 6.4. The weighted mean according to [68, p. 787] of the depicted data points is $(351.23 \pm 104.66)\,\mathrm{V\,nJ^{-1}}$.

Table 6.4: Summary of the scaling constant, C_F, the electron bunch charge, Q, and the S/N ratio quotient of the two spectrometers for the measurements depicted in Figure 6.13. The definiton of C_F can be found in section 5.4. The r.m.s. deviation of the charge measurements is below 0.1 pC. The signal-to-noise ratio quotient corresponds to $\overline{r_{S/N}}$(2-PRISM)/$\overline{r_{S/N}}$(CRISP4)

setting	C_F (V nJ^{-1})	Q (pC)	$\overline{r_{S/N}}$ quotient
A	205.62 ± 12.7	56	326.5 ± 52.9
B	275.66 ± 20.83	41	456.3 ± 67.1
C	566.60 ± 57.85	37	681.2 ± 118
D	405.51 ± 52.13	45	525.8 ± 79.8
E	448.84 ± 62.51	45	411.5 ± 69.5
F	677.62 ± 105.72	48	1289.5 ± 248.9
G	673.82 ± 21.02	59	236.5 ± 37.6
H	989.17 ± 55.37	20	353.5 ± 54.4

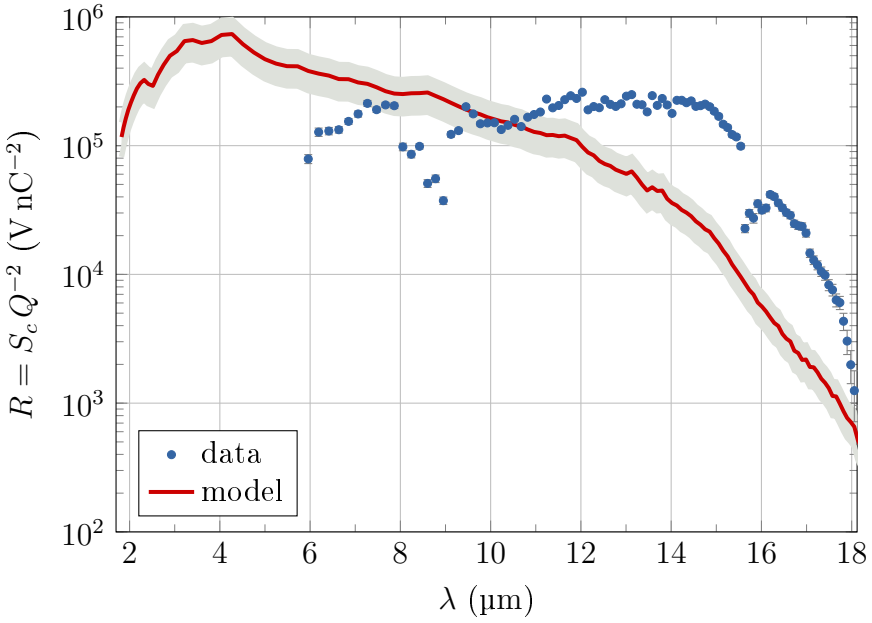

Figure 6.16: Response of the double-prism spectrometer, $R(\#)$, as derived from the measurements at the FELIX facility (*blue*) in comparison to the calculated response function, $C_F\,R^*$ (cf. section 5.4), with $C_F = (351.23 \pm 104.66)\,\mathrm{V\,nJ^{-1}}$ (*red*). The grey area denotes the uncertainty introduced by C_F. The *blue trace* includes the correction for distorted elements (cf. section 6.1.3).

Comparison of the scaled partial response function to FELIX data

The obtained value for the scaling constant, $C_F = (351.23 \pm 104.66)\,\mathrm{V\,nJ^{-1}}$, enables the assessment of the scaled partial response function, $C_F\,R^*$, with respect to the results from measurements at the FELIX facility (cf. section 6.1.3).

The Figure 6.16 presents the expected detector response for a transition radiation spectrum of a bunch with $Q = 1\,\mathrm{nC}$, $\sigma_{\mathrm{trans}} = 200\,\mu\mathrm{m}$ and $|F_{\mathrm{long}}(\lambda)| = 1$, that was derived from measurements at FELIX (*blue dots*, cited from Fig. 6.6b). The data includes corrections for distorted signals (cf. section 6.1.3). The modelled partial response function (*red trace*) was scaled with the obtained scaling constant, C_F.

The two traces yield apparent differences for wavelengths above $\lambda \approx 11\,\mu\mathrm{m}$. Since discrepancies in this wavelength range are also observed in the comparison to *CRISP4* data, this recurring feature is suspected to be connected with imaging errors and distortions of the transverse profile in the detector plane. The result derived from measurements at FELIX, i. e. the blue points in Figure 6.16, were recorded with an approximately Gaussian-shaped transverse profile, whereas the calculated response for the setup at the FLASH facility involves the ring-structure of transition radiation (compare Fig. 6.7). Since the extension of the transverse profiles increases with wavelength, the effect of distortions and deviations in the transverse intensity profile is increasingly noticeable. Please refer also to the form factor comparison above. The result has to be assessed under the constraint of the distorted single element signals in the FELIX data, which add, except in the interval $\lambda_j \in [9.6\mu\mathrm{m}, 13\mu\mathrm{m}]$, an additional uncertainty. The feature in the measured trace between 8 µm and 9 µm is associated with this issue. Please refer to section 6.1.3. The data acquired at the FLASH facility was taken before the calibration campaign and before the grounding improvement by the manufacturer in early 2015 [146].

However, the absolute value of the result from FELIX measurements coincides with the scaled partial response function, whose scaling constant, C_F, was independently determined by the comparison to *CRISP4* data. This circumstance strongly indicates the validity of the estimated scaling constant, albeit exhibiting distinct features at wavelengths between 8 µm and 9 µm and above $\lambda \approx 11\,\mu\mathrm{m}$.

Detection limit

The noise behaviour and thus, the detection limit for increasing bunch length is another important property in the comparison of the double-prism spectrometer and *CRISP4*. Figure 6.17 presents the noise equivalent of the form factor measurement of setting B (Fig. 6.13a). Regarding the mean in the wavelength range between 6 µm and 17 µm, the NEF of the double-prism spectrometer, *2-PRISM*, is lower by a factor of 28.1 ± 2.6 compared to *CRISP4* for the electron bunch charge of $Q = 41$ pC.

The figure also shows the calculated longitudinal form factors of Gaussian current profiles (*grey traces*). Considering purely Gaussian profiles without substructures, the longest detectable bunch length is expected to be on the order of $\sigma_l = 8.5$ µm at $Q = 41$ pC. Substructures may result in an enhancement of short-wavelength components. The upper bunch length limit will increase with increasing bunch charge.

Signal-to-noise ratios

The quotients of the mean signal-to-noise ratios of the double-prism spectrometer and *CRISP4*, $\overline{r_{S/N}}$(2-PRISM)/$\overline{r_{S/N}}$(CRISP4), for the comparisons are given in Table 6.4 and in Figure 6.14. The double-prism spectrometer exhibits signal-to-noise ratios that are, depending on the bunch charge and compression setting, higher by a factor of $10^2 - 10^3$ compared to the *CRISP4* spectrometer. Referring to the detectivity comparison in chapter 3 (Fig. **??**), the expected difference of factor $> 10^2$ for MCT detectors with respect to pyroelectric detectors could herewith be experimentally confirmed.

6.3 Note on uncertainties and error sources

The depiction above and in chapter 5 includes the statistical uncertainty of the mean of the measured quantities. For instance, several hundred spectra taken with the MCT detector were averaged and plotted together with the related r.m.s. deviation of the mean as error bars. The latter measure reduces with the square root of the number of single-shot measurements, $\sqrt{N}$, [150], and is not visible in many graphs. In the form factor measurement of setting

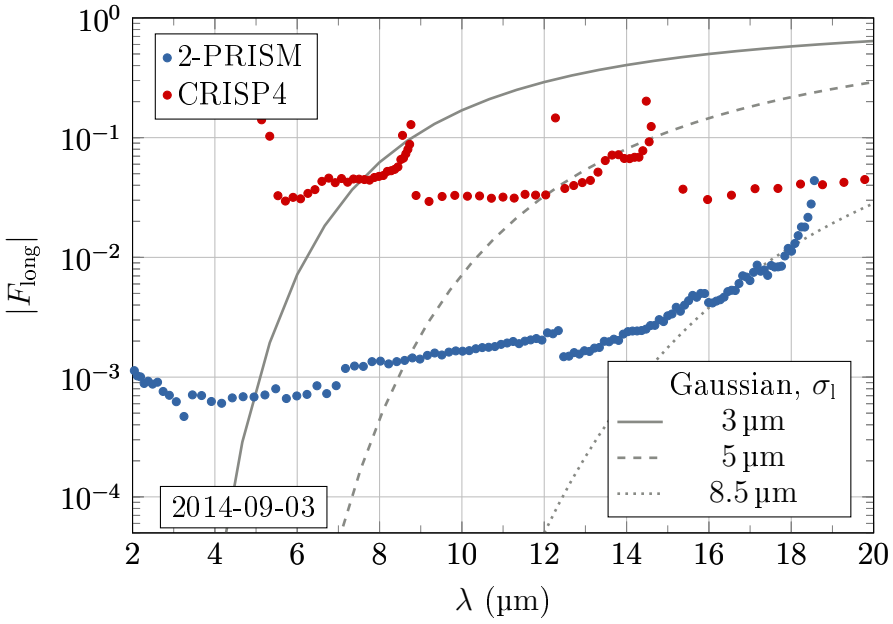

Figure 6.17: Comparison of the noise-equivalent form factor (NEF) of the grating spectrometer *CRISP4* and the double-prism spectrometer for the data set depicted in Fig. 6.13b, where the data of the latter have been scaled with the constant $C_F = 275.66\,\mathrm{V\,nJ^{-1}}$. The electron bunch charge was 41 pC. The *grey* traces indicate calculated form factors for Gaussian current profiles with given longitudinal widths.

B (Fig. 6.13a), detector element 60 shows a sample r.m.s. deviation of $\sigma_S \approx 41\,\mathrm{mV}$, whereas the mean r.m.s. deviation is just $\overline{\sigma_S} \approx 2\,\mathrm{mV}$. The underlying equations are mentioned in section D.2.

The exact determination of the systematic uncertainties and measurement errors is a non-trivial task and involves a comprehensive knowledge of the entire apparatus. In the case of the accuracy of the voltage readings of the MCT detector, constant offsets are overcome by baseline substraction and measurement errors that scale linearly with the signal are incorporated in the response function, R. As long as the systematic errors are persistent in characteristic and amplitude, the calculated form factors are correct with respect to the accuracy of the response function. The error of the charge measurement, that is further required to determine the form factor, are estimated to be below 10 % for the dark current monitor [133, 151].

The accuracy of the intensity measurement with the thermal power sensor during the calibration campaign relies on the cross-calibration of the device that was facilitated by the manufacturer, Ophir Optronics. A comparison to another thermal power head of the same type showed a relative deviation on the order of 25 %. The FELO wavelength set point at FELIX, λ_j, is set by FEL parameters, such as the undulator parameter. The wavelength was monitored and adjusted according to an online grating spectrometer. The typical deviation between set point and spectrometer reading, that also relies on the calibration of the device, was $\lesssim 0.05\,\mu\text{m}$.

In conclusion, all measurements have to be regarded with respect to observational errors such as statistical uncertainties and the systematic errors due to imperfect instruments and their calibration. Whereas the statistical uncertainties are given with the measured values, the exact determination of the latter was not possible, e. g. due to missing calibration normals for the power sensors and charge monitors. These errors were estimated to the values stated above.

6.4 Discussion

The detailed knowledge of the properties of transition radiation and the spectrometer, which includes the radiation source, the transport to the spectrometer and the detector, is essential for the determination of the spectral distribution and the absolute value of the longitudinal form factor by spectroscopy.

A campaign at the FELIX FEL facility was performed in order to measure the response function, R, of the double-prism spectrometer and the spectrometer *CRISP4* [145]. The spectral response of the spectrometer setup, i. e. the detector voltage reading for an incident FELO beam intensity, can be determined only in regard to the specific properties of the FELO beam, such as bandwidth and transverse profile. The application of these results for another radiation source, to be specific, transition radiation, requires the consideration of several key differences.

First, the spectrum of transition radiation is broad compared to the FELO beam, which yields spectral line widths smaller than the spectral resolution of the spectrometer. For transition radiation, a continuous spectral distribu-

tion is mapped to a specific detector element instead a single spectral line. Second, the transverse beam profile of transition radiation yields a ring structure, whereas the FELO delivers a Gaussian-like profile. The distortions in the detector voltage distributions add an additional uncertainty in the FELIX data. In addition, the band pass filter measurements and form factor comparisons indicate deviations of the actual imaging properties to the spectrometer model in the upper half of the wavelength range that is covered by the prism spectrometer. These circumstances lead to the presented deviations in the comparisons of FELIX measurements to the calculated response function and the form factors with respect to *CRISP4*. Further studies and appropriate countermeasures on these issues are advisable, but the validity of the key conclusions, that are depicted below, are not impaired:

- The dispersion of the spectrometer setup and the double-prism arrangement follows the expected distribution.
- The model of the partial response function was proven via measurements at FELIX to be appropriate for the given problem.
- The value of the scaling constant, C_F, that was determined by comparative measurements with the *CRISP4* spectrometer, is on the same scale of the value estimated from the data taken during the calibration campaign.
- Albeit exhibiting differences, the form factor comparisons for various charge and compression settings clearly show a coincidence in the slope of the spectral distribution and thus, in electron bunch length.
- The double-prism spectrometer shows high signal-to-noise ratios and low detection limits with respect to *CRISP4*. For specific beam conditions, the device is more sensitive than the bunch charge diagnostic devices at the FLASH facility (confer chapter 5). Its capability for single-shot measurements can mitigate uncertainties due to shot-to-shot fluctuations.

In summary, the spectrometer setup and the model for the underlying partial response function, R^*, were confirmed to be suitable and valid for the given problem.

Summary and Outlook

The investigation of the longitudinal extension and the longitudinal current profile of electron bunches driving free-electron lasers or delivered from plasma wakefield-based accelerators is of high importance for the investigation of the FEL process and the acceleration method respectively. These electron bunches are required to yield lengths on the micron scale and charges of well below 30 pC.

During this work, the diagnostic method of investigating the spectral composition of the radial, but longitudinally compressed Coulomb field of relativistic electron bunches was studied. Transition radiation as a secondary radiation emitted by the electrons was investigated in the mid-infrared wavelength regime, that is of particular interest for electron bunches with lengths below 10 µm or durations shorter approx. 33 fs. A further constraint was given by the total charge per electron bunch. Established diagnostic devices at the FLASH FEL facility, e. g. the spectrometer *CRISP4*, approach their detection limit for mid-infrared wavelengths for charges less than $\approx$ 20 pC.

Subsequent to preparatory numerical studies of transition radiation and spectroscopic methods, a spectrometer with an arrangement of two consecutive zinc selenide prisms was developed, assembled and commissioned. The double-prism design allows for the imaging of the spectral band between 2 µm and 18 µm onto a line array of MCT detector elements that is capable of single-shot operation. The commissioning show high signal-to-noise rations for bunch charges. At $Q = 4.9$ pC, a signal-to-noise ratio of ≈ 2000 was observed, whereas a detector signal was still present at 3.8 pC. The sensitivity of the spectrometer is higher than the bunch charge diagnostic devices at the FLASH facility.

A numerical model describing the spectrometer was developed in order to derive the longitudinal form factor of the electron bunches from measured tran-

sition radiation spectra. Furthermore, a calibration campaign at the FELIX FEL facility was conducted to investigate the spectral and intensity response characteristics of the double-prism spectrometer. Comparative measurements taken at the FLASH facility confirmed the validity of the results with respect to the well-understood grating spectrometer, whose accuracy was confirmed via a transverse deflecting structure as a third longitudinal diagnostic. The intensity calibration of the double-prism spectrometer found with comparative measurements is on the same scale as the value estimated from results of the calibration campaign. However, the comparative assessment of the spectrometers revealed differences in the derived form factors. Further studies on these differences are advisable, but do not affect the validity of the developed setup, the obtained measurements and conclusions.

The double-prism concept in combination with sensitive MCT detectors was proved to be appropriate for the given problem. The spectrometer allows the determination of form factors which coincide with measurements taken with established diagnostic devices. In combination with high signal-to-noise ratios, the setup that was developed within this work is particularly suited for low-charge and short electron bunches. In a future step, the form factor measurements can be used with *phase retrieval* algorithms in order to estimate a likely time-domain current profile of the bunches in extension to further spectrometers as well as a stand-alone and single-shot diagnostic.

Part III

Appendix

A The free-electron laser facility FLASH

The facility FLASH consists of a linear accelerator and two independently operable undulator beam lines. The facility arose from a test facility for the TESLA project, where a TeV-linear collider was planned to be operated together with a free-electron laser [152] .

The TESLA Test Facility (TTF) for superconducting acceleration modules and a free-electron laser [153, 154] demonstrated first lasing at 109 nm in SASE mode in 2000 [155]. After upgrades in design and electron beam energy, lasing at 32 nm was shown in 2005 and the FEL officially started the operation for users in the same year [102]. Renamed to FLASH, the acronym for free-electron laser in Hamburg, the linear accelerator received its last major upgrade in 2009/2010 and now delivers electron energies up to approx. 1.25 GeV for photon wavelengths between $(4.1 - 45)$ nm.

A second undulator beam line, FLASH2, was recently built and first lasing was observed in 2014 at approximately $\lambda = 40$ nm [156]. A third beam line for plasma-wake field experiments, FLASHForward, is currently under construction [157].

A.1 The linear accelerator

The electron source of the linear accelerator is a normal-conducting RF-driven photo injector. UV laser pulses expel photoelectrons from a thin layer of $CsTe_2$ on a molybdenum plug. A 1.5-cell RF resonator that is operated at 1.3 GHz catches the expelled cloud, or bunch of electrons, and accelerates it to approx. 5 MeV ($\gamma \approx 10$). The immediate acceleration to relativistic energies is required to counteract repulsive space charge effects, that are proportional

to γ^{-2} [2, 102].

A superconducting (SC) module made of eight nine-cell TESLA-type cavities [34] increases the electron bunch energy to approx. 150 MeV and imprints a position-energy dependency onto the bunch. Due to the momentum-dependent deflection by dipole magnets, this energy chirp is converted into a longitudinal rearrangement of the electrons while passing a c-shaped magnetic chicane (cf. Figure A.1), that follows the first accelerating module [158].

Two subsequent SC accelerating modules are followed by a second bunch compressor which differs from the first in its s-shaped design. The finally compressed electron bunches, yielding durations on the sub-picosecond scale, are further accelerated by four superconducting modules to a final energy of up to 1.25 GeV [102].

After a truncation of the transverse and energy profile for cleaning, a pulsed dipole magnet in combination with a septum magnet separates the bunches for the two undulator beam lines FLASH1 and FLASH2 as well as to FLASH-Forward by a subsequent magnet [156].

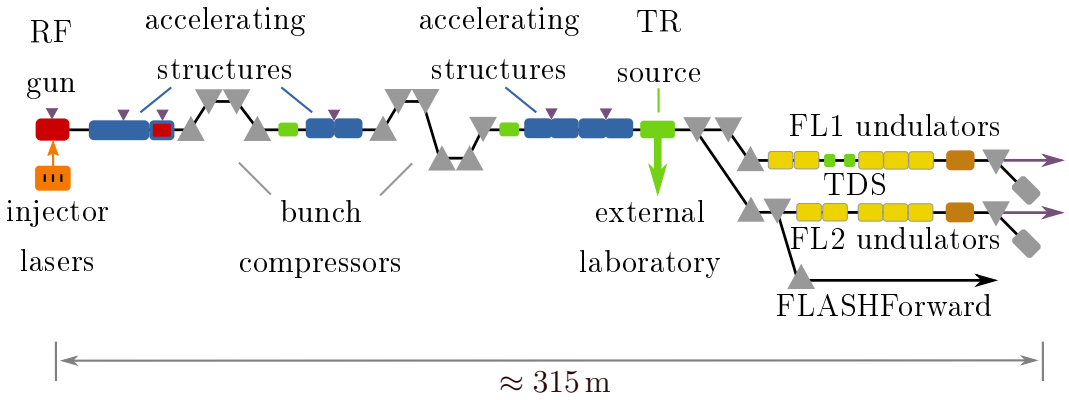

Figure A.1: Overview of the FLASH facility. The schematic is not to scale and is adapted from [159].

A.2 Timing structure

The superconducting linear accelerator enables the amplitude of the RF field to be held and stabilised for acceleration for up to 800 µs. In standard operation mode, a train of up to 800 electron bunches with a spacing down to 1 µs

(1 MHz) can be accelerated. The repetition rate of the RF pulses and thus the pulse train repetition rate is 10 Hz. Special modes allow an intra-train spacing of $0.\overline{3}$ µs at a reduced train repetition rate of 5 Hz [53, 159, 160].

A.3 Longitudinal electron beam diagnostics

A detailed depiction of the devices for the longitudinal diagnosis at the FLASH facility can be found e. g. in [4, 50, 66], whereas the transition radiation source, that is of particular importance for this work, is introduced below.

Transition radiation source

The transition radiation source is located behind the last accelerating module and consists of a Al-coated silicon screen of (15 x 25) mm transverse extension and a thickness of 380 µm. Horizontally displaced by 10 mm with respect to the electron beam axis, the 45 deg-angled screen guides the transition radiation towards a transfer line. A pulsed dipole magnet deflects a selectable single electron bunch from the bunch train onto the TR emitter [66, 161].

The transfer line, that is separated from the vacuum of the accelerator beam pipe by a diamond window, is evacuated to better than 0.1 mbar and guides the radiation into an external laboratory via focusing and plane mirrors (confer Table C.3). A switching mirror allows the radiation to be directed either to the double-prism spectrometer or to the grating spectrometer *CRISP4*. [66, 161]

CRISP4

The grating spectrometer *CRISP4* consists of two sets of five diffraction gratings, that are arranged in a low-pass configuration – see Fig. A.3. For the polarisation perpendicular to the grating grooves, a defined wavelength band is dispersed and wavelengths above a sharp threshold are reflected with high efficiency. Disregarding a stage for spectral filtering, four line arrays of pyroelectric detectors and two sets of four gratings examine the spectral distribution between 5 µm and 44 µm as well as from 45 µm to 435 µm in single shots respectively [9, 66, 162].

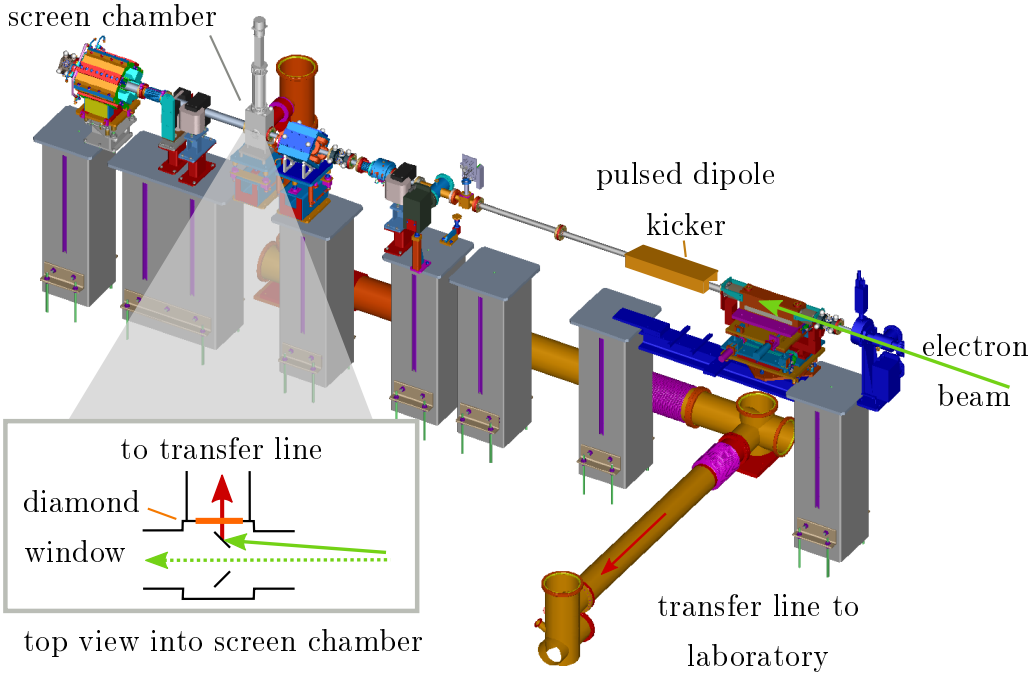

Figure A.2: Technical drawing (not complete) of the accelerator section behind the last accelerating module, ACC7. The pulsed dipole kicker deflects the electron bunches (*green*) onto the off-axis screen acting as the TR emitter. The transition radiation (*red*) is guided through a diamond window and an evacuated transfer line into an external laboratory. Adapted from a drawing that was kindly provided by Kai Ludwig (DESY).

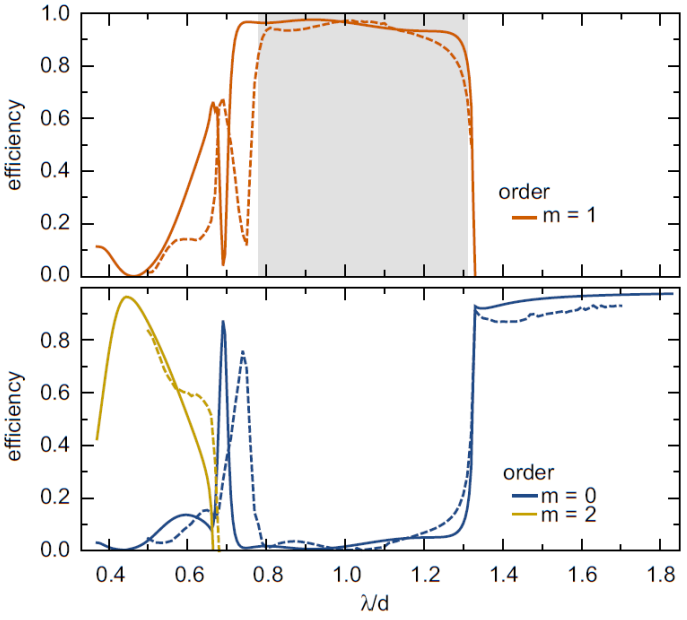

Fig. 2. Efficiency curves of a gold-plated reflection grating for radiation polarized perpendicular to the grooves, computed with the codes *PCGrate* (solid curves) and *GSolver* (dashed curves). Top graph: first-order diffraction $m=1$. The wavelength range $0.78 < \lambda/d < 1.31$ marked by the shaded area is used as a basis for the spectrometer layout providing an almost flat efficiency. Bottom graph: diffraction orders $m=0$ and $m=2$. Above $\lambda_0/d = 1.33$ all radiation is directed into the zeroth order which simply means that the grating acts as a plane mirror. For small wavelengths ($\lambda/d < 0.78$) all three orders $m = 0, 1, 2$ contribute to the diffraction pattern. In order to avoid ambiguities this wavelength range must be removed by filtering the incident radiation.

(a) principle of grating staging

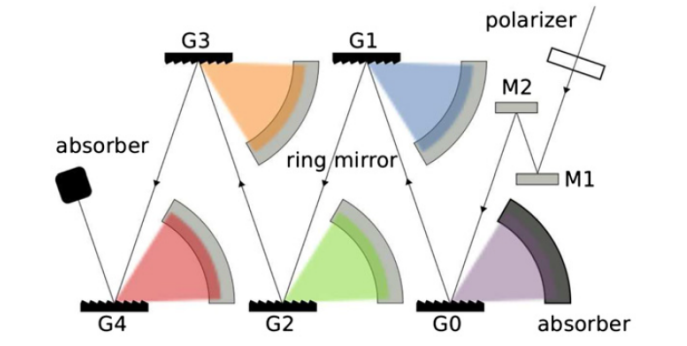

Fig. 3. Principle of the staged spectrometer equipped with five reflection gratings. Explanations are given in the text. To avoid FIR absorption in humid air, the spectrometer is mounted in a vacuum vessel (not shown). The detector arrays mounted above the focusing mirrors are not displayed.

(b) optical setup

Figure A.3: Operation principle (a) and schematic of the optical setup (b) of the grating spectrometer *CRISP4*. The figures and captions are cited from [9].

B Setup at the experiment on laser-wakefield acceleration at the ASTRA-GEMINI laser facility

The double-prism spectrometer and the imaging system in particular were designed for an experiment investigating laser-wakefield acceleration (LWFA) utilising the ASTRA-GEMINI laser system. The system is located at the Rutherford Appleton Laboratory, Harwell Oxford, UK, and is operated by the Central Laser Facility (CLF) of the Science and Technology Facilities Council (STFC). Details on the experiment and the involved persons can be found in [163].

The laser system can provide two separate laser beams of pulses with a peak power of 15 J within 40 fs [103]. During the experiment in early 2014 which was conducted in collaboration with Oxford University, a pair of beams with independently tunable intensity and temporal delay was derived from one beam of ASTRA-GEMINI in order to study a controlled injection technique for electrons into a wakefield in gas targets [164]. An aluminium tape (thickness 100 µm) was used as transition radiation emitter and an optical system guided the radiation to an arrangement of spectrometers for near-UV up to near-IR wavelengths as well as to the double-prism spectrometer. A $f/20$-spherical mirror picked up the divergent transition radiation after passing through an optical delay line. The spectral components in the mid-IR regime were separated from the TR beam via an ITO-coated glass plate [165, 166] and reflected to the double-prism spectrometer.

The imaging system is schematically depicted in Figure B.1. The optical

elements are summarised with their properties in Table C.2. The principal design of the optical imaging system of the double-prism spectrometer is based on this setup, whereas the subsequent use at the FLASH facility was already considered. Reference [163] mentions example spectra taken with the spectrometers introduced above.

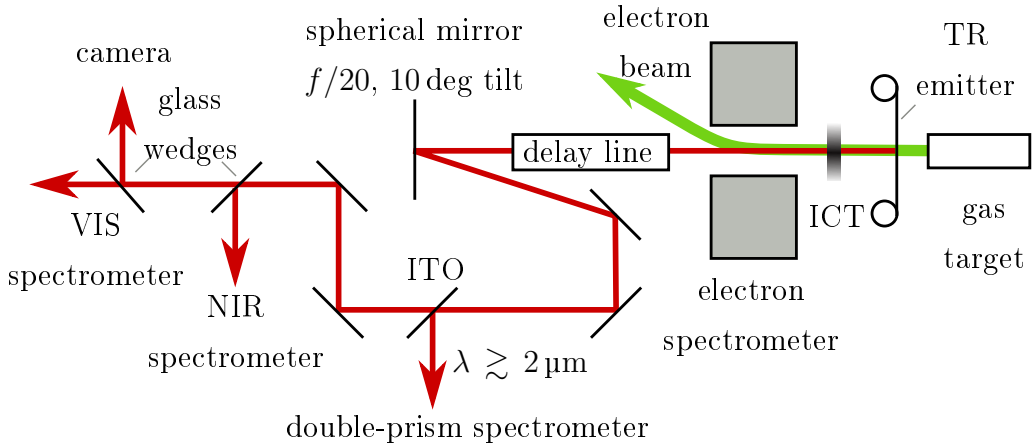

Figure B.1: Schematic of the optical setup at the ASTRA-GEMINI laser facility. Two laser beams were focused into the gas target and generated an electron beam. The electron bunches passed the TR screen, a 100 µm-thick aluminium tape. The hereby generated transition radiation (*red*) was guided to two commercial grating spectrometers, a camera and the double-prism spectrometer.

C THzTransport

C.1 Details on simulated optical systems

The following tables summarise the simulation parameters used within this work. The values for the double-prism spectrometer can be found in Table 4.5.

Table C.1: Sample optical system for the estimation of CTR intensity in section 4.1.2

no.	distance (mm)		element name	parameters
	from source	from preceding element		
0	–	–	TR source	transverse Gaussian electron beam with $\sigma = 100\,\mu m$, quadratic screen with 5 mm edge length, $\gamma = 978$ ($\approx 500\,MeV$)
1	1302	1302	focusing mirror	$f = 1016\,mm$, diameter 50.8 mm
2	3802	2500	focusing mirror	$f = 200\,mm$, diameter 50.8 mm
3	4002	200	detector plane	

Table C.2: Setup at the LWFA experiment at GEMINI (cf. section 4.2.3)

no.	distance (mm)		element name	parameters
	from source	from preceding element		
0	–	–	TR source	transverse Gaussian electron beam with $\sigma =$ 100 µm, quadratic screen with 5 mm edge length, $\gamma = 1000$ (≈ 500 MeV)
1	523	523	aperture (plane mirror)	diameter 25.4 mm
2	603	80	aperture (plane mirror)	diameter 25.4 mm
3	888	285	aperture (plane mirror)	diameter 50.8 mm
4	1302	414	spherical mirror	$f = 1016$ mm, diameter 50.8 mm
5	3015	1713	aperture (ZnSe window)	diameter 32 mm, thickness 3 mm
6-12	4852	1837	double-prism spectrometer	cf. Table 4.5 and Fig. 4.12

Table C.3: Setup at the FLASH FEL facility.

no.	distance (mm)		element name	parameters
	from source	from preceding element		
0	–	–	TR source	transverse Gaussian electron beam with $\sigma = 200\,\mu m$, rectangular screen with $(7.5\,x\,12.5)\,mm$[1]edge length, tilted by 45 deg, $\gamma = 1957$ (1 GeV)
1	45.5	45.4	wedged diamond window	diameter 20 mm, vertical wedge angle 1 deg, thickness 0.5 mm
2	519.4	474	toroidal mirror	$f = 376$ mm, diameter 140 mm
3	2060	1540.6	toroidal mirror	$f = 651$ mm, diameter 180 mm
4	5958	3898	toroidal mirror	$f = 3698$ mm, diameter 180 mm
5	8978	3020	toroidal mirror	$f = 4500$ mm, diameter 180 mm
6	17978	9000	toroidal mirror	$f = 3500$ mm, diameter 180 mm
7	20188	2210	toroidal mirror	$f = 3000$ mm, diameter 140 mm
8	20928	740	aperture (ZnSe window)	diameter 32 mm, thickness 3 mm
9-15	22068	1140	double-prism spectrometer	cf. Table 5.1 and Fig. 4.12

[1]The size of the actual TR screen is $(15\,x\,25)\,mm$. In the simulations, the screen size was reduced by the factor of 2 due to numerical reasons.

D Supplementary Information

D.1 Funding

This work has been supported by the German Federal Ministry of Education and Research (Bundesministerium für Bildung und Forschung) under contract 05K10GU2 & FS FLASH 301.

D.2 Statistics

The measurement of a quantity has always to be regarded with respect to systematic errors, for example imperfect measurement devices, and the uncertainty due to statistical fluctuations. A discussion of these errors and uncertainties is inevitable to judge the validity of measurements. This note addresses the statistical uncertainties and follows the treatment in [150].

Figuratively speaking, the mean value, $\overline{S}$, represents a "best" value of a measured quantity of interest, say, S. The mean is determined by N single measurements or samples, S_i, with $i \in [1, N]$, according to

$$\overline{S} = \frac{\sum_{i=1}^{N} S_i}{N}. \tag{D.1}$$

However, the expression

$$\sigma_S = \sqrt{\frac{1}{N-1} \sum_{i=1}^{N} (S_i - \overline{S})^2} \tag{D.2}$$

just gives the root mean square (r.m.s.) deviation, or standard deviation, of the *sample*. The appropriate uncertainty of the *mean*, is described by the formula

$$\overline{\sigma_S} = \frac{\sigma_S}{\sqrt{N}} = \sqrt{\frac{1}{N(N-1)} \sum_{i=1}^{N} (S_i - \overline{S})^2}, \tag{D.3}$$

that is also denoted as the r.m.s. deviation of the mean.

In this monograph, the mean values for quantities that are measured or derived from measurements, as well as the error bars in plots, are specified in the form

$$\overline{S} \pm \overline{\sigma_S}. \tag{D.4}$$

D.3 Dispersion formulae

The description of the dispersion of the double-prism arrangement, that is introduced in chapter 4, is based on the fundamental formulas (3.4) and (3.5). The particular formulas for the double-prism case is depicted here.

The total deflection angle, $\theta = \theta_1 + \theta_2$, of an incident ray is composed by the contributions of the two prisms, θ_1 and θ_2 respectively. These are given by

$$\begin{aligned} \theta_1(\lambda) &= \alpha_1 + \alpha_2(\lambda) - \epsilon_1 && \text{(D.5)} \\ &= \alpha_1 - \epsilon_1 \\ &\quad - \arcsin\left(\sin(\epsilon_1)\sqrt{n(\lambda)^2 - \sin^2(\alpha_1)} - \cos(\epsilon_1)\sin(\alpha_1)\right) && \text{(D.6)} \end{aligned}$$

and

$$\theta_2(\lambda) = \gamma_1(\lambda) + \gamma_2(\lambda) - \epsilon_2. \tag{D.7}$$

The angle of incidence of the second prism, $\gamma_1(\lambda)$, depends on the wavelength, the exit angle of the first prism, $\alpha_2(\lambda)$ and the inter-prism angle, Π, as well as on the wavelength:

$$\gamma_1(\lambda) = \pi - \alpha_2(\lambda) - \Pi. \tag{D.8}$$

The treatment of the deflection of the second prism, θ_2, corresponds to eqn. D.6 with the replacements $\theta_1 \to \theta_2$, $\alpha_1 \to \gamma_1$ and $\epsilon_1 \to \epsilon_2$.

D.4 Further tools and software

Apart from the scientific software mentioned earlier in the thesis, a number of further tools and software were used. Table D.1 summarises tools and their respective application.

Table D.1: Further tools

purpose	name
typesetting	LaTeX and the KOMA-Script as well as contained packages
typesetting	TeXStudio
typesetting	"DissOnlineLatex" [167]
typesetting	colour definitions of the TangoDesktopProject
bibliography management	Mendeley Desktop [168]
image processing	GIMP
image processing	Inkscape
image processing	Plot Digitizer, `http://plotdigitizer.sourceforge.net`
data visualisation	MATLAB extension "matlab2tikz" [169]
data visualisation	MATLAB extension "Perceptually improved colormaps" [170]

D.5 ZEMAX simulations

Ray-tracing simulations with the software *ZEMAX* [123] were conducted in order to study the aberrations that originate from the angular spread of the dispersed light (cf. section 4.2.3). The most important simulation parameters for a off-axis parabolic mirror with a deflection angle of 30 deg can be found below.

```
System/Prescription Data
[...]
GENERAL LENS DATA:
Surfaces                 :                  17
Stop                     :                   1
System Aperture          :   Entrance Pupil Diameter =   20
[...]
Effective Focal Length   :             152.4  (in air at system temperature and pressure)
Effective Focal Length   :             152.4  (in image space)
Back Focal Length        :             148.6
Total Track              :               262
Image Space F/#          :              7.62
Paraxial Working F/#     :              7.62
Working F/#              :          6.460041
Image Space NA           :        0.06547599
Object Space NA          :             1e-009
Stop Radius              :                10
Paraxial Image Height    :                 0
Paraxial Magnification   :                 0
Entrance Pupil Diameter  :                20
Entrance Pupil Position  :                 0
Exit Pupil Diameter      :          21.25535
Exit Pupil Position      :         -117.0431
Field Type               :   Angle in degrees
Maximum Radial Field     :                 0
Primary Wavelength [microm] :                10
Angular Magnification    :                 0
Lens Units               :    Millimeters

[...]

Wavelengths      : 17
Units: \si{\micro\metre}
 #         Value          Weight
 1         2.000000       1.000000
[...]
17        18.000000       1.000000

SURFACE DATA SUMMARY:

Surf        Type          Radius          Thickness             Glass          Diameter          Conic          Comment
 OBJ    STANDARD        Infinity        Infinity                                    0              0
 STO    STANDARD        Infinity              50                                   20              0
```

```
   2   COORDBRK              –              0                      –              –  Element Tilt
   3   TILTSURF              –           15.5                   ZNSE             58  –  Prism front
   4   TILTSURF              –             80                      –             58  –  Prism back
   5   COORDBRK              –              0                      –              –
   6   COORDBRK              –              0                      –              –  Element Tilt
   7   TILTSURF              –           15.5                   ZNSE             58  –  Prism front
   8   TILTSURF              –             51                      –             58  –  Prism back
   9   COORDBRK              –              0                      –              –  decenter
  10   COORDBRK              –              0                      –              –  tilt
  11   COORDBRK              –              0                      –              –
  12   STANDARD       Infinity             50                      –       54.11658  0  drift
  13   STANDARD         −304.8              0                 MIRROR           76.2  −1  parab #1
  14   COORDBRK              –         −150.5                      –              –  distance
  15   COORDBRK              –              0                      –              –  tilt/decenter
  16   COORDBRK              –              0                      –              –  add. tilt
 IMA   STANDARD       Infinity                                     –           76.4  0

SURFACE DATA DETAIL:

Surface   2 COORDBRK Element Tilt
[...]
Tilt About X          :                25
[...]
Order                 : Decenter then tilt

Surface   3 TILTSURF Prism front
X Tangent             :                 0
Y Tangent             :             0.267
Aperture              : Rectangular Aperture
X Half Width          :                30
Y Half Width          :                29

Surface   4 TILTSURF Prism back
X Tangent             :                 0
Y Tangent             :            −0.267
Aperture              : Rectangular Aperture, Pickup From Surface 3
X Half Width          :                30
Y Half Width          :                29

Surface   5 COORDBRK
Decenter X            :                 0
Decenter Y            :        −31.994894
[...]
```

```
87  Order                    : Decenter then tilt
88
89  Surface   6 COORDBRK Element Tilt
90  [...]
91  Tilt About X             :                45
92  [...]
93  Order                    : Decenter then tilt
94
95  Surface   7 TILTSURF Prism front
96  X Tangent                :                 0
97  Y Tangent                :             0.267
98  Aperture                 : Rectangular Aperture
99  X Half Width             :                30
100 Y Half Width             :                29
101
102 Surface   8 TILTSURF Prism back
103 X Tangent                :                 0
104 Y Tangent                :            -0.267
105 Aperture                 : Rectangular Aperture, Pickup From Surface 3
106 X Half Width             :                30
107 Y Half Width             :                29
108
109 Surface   9 COORDBRK decenter
110 Decenter X               :                 0
111 Decenter Y               :        -7.9164084
112 [...]
113 Order                    : Decenter then tilt
114
115 Surface  10 COORDBRK tilt
116 [...]
117 Tilt About X             :         10.670722
118 [...]
119 Order                    : Decenter then tilt
120
121 Surface  11 COORDBRK
122 Decenter X               :                 0
123 Decenter Y               :                 0
124 Tilt About X             :                 0
125 Tilt About Y             :                 0
126 Tilt About Z             :               180
127 Order                    : Decenter then tilt
128
129 Surface  12 STANDARD drift
```

```
130
131 Surface  13 STANDARD parab #1
132 Mirror Substrate          : Flat, Thickness = 1.52400E+000
133 Tilt/Decenter             :      Decenter X      Decenter Y          Tilt X          Tilt Y          Tilt Z           Order
134 Before surface            :              0         -81.66               0               0               0 Decenter, Tilt
135 After surface             :             -0          81.66              -0              -0              -0 Tilt, Decenter
136 Aperture                  : Circular Aperture
137 Minimum Radius            :              0
138 Maximum Radius            :           38.1
139 X- Decenter               :              0
140 Y- Decenter               :          81.66
141
142 Surface  14 COORDBRK distance
143 [...]
144 Order                     : Decenter then tilt
145
146 Surface  15 COORDBRK tilt/decenter
147 Decenter X                :              0
148 Decenter Y                :      -85.163984
149 Tilt About X              :             -30
150 [...]
151 Order                     : Decenter then tilt
152
153 Surface  16 COORDBRK add. tilt
154 [...]
155 Order                     : Decenter then tilt
156
157 Surface IMA STANDARD
158
159 [...]
160
161 GLOBAL Surface CENTER OF CURVATURE POINTS:
162
163 Reference Surface: 1
164
165 Surf             X             Y             Z
166   1             -             -             -
167   2             -             -             -   Element Tilt
168   3             -             -             -   Prism front
169   4             -             -             -   Prism back
170   5             -             -             -
171   6             -             -             -   Element Tilt
172   7             -             -             -   Prism front
```

```
173   8                 -                 -                 -   Prism back
174   9                 -                 -                 -   decenter
175  10                 -                 -                 -   tilt
176  11                 -                 -                 -
177  12                 -                 -                 -   drift
178  13     0.0000000000   109.1899566957   227.3778215593   parab #1
179  14                 -                 -                 -   distance
180  15                 -                 -                 -   tilt/decenter
181  16                 -                 -                 -   add. tilt
182  17                 -                 -                 -
183 [...]
```

List of abbreviations

Table D.2: List of abbreviations

AOI	angle of incidence
App.	appendix
BLIP	background limited infrared photodetector
cf.	confer
CsI	caesium iodide
deg	degree
DESY	Deutsches Elektronen Synchtrotron
EO	electro-optic
eqn.	equation
FEL	free-electron laser
FELO	free-electron laser oscillator
FLASH	Free-electron laser in Hamburg
FIR	far-infrared
FT	Fourier transform
FWHM	full width at half maximum
KRS-5	thallium bromodiodide
ICT	integrated current transformer
IR	infrared
ITO	indium tin oxide
LCLS	Linac Coherent Light Source
linac	linear accelerator
LWFA	laser-wakefield acceleration
MCT	mercury cadmium telluride
mod.	model

continued on next page

List of abbreviations (*continued*)

NaCl	sodium chloride
NEF	noise-equivalent form factor
NEP	noise-equivalent power
NC	normal-conducting
NIR	near-infrared
OAP	off-axis parabolic (mirror)
RF	radio frequency
r.m.s.	root mean square
PEM	photoelectromagnetic
PC	photoconductive
PV	photovoltaic
PWFA	plasma-wakefield acceleration
SASE	self-amplified spontaneous emission
SC	superconducting
Sec.	section
SLAC	Stanford Linear Accelerator Center
UV	ultraviolet
w.r.t.	with respect to
w/o	without
ZnSe	zinc selenide

List of symbols

Table D.3: List of symbols

$\#$	detector element number
A	active area of one detector element
a	prism front surface width in the dispersive plane
a_{lim}	clear aperture of the dispersive stage of a spectrometer
a_{b}	diameter of a parallel beam
$\alpha_{1,2}$	angles towards the prism surface normal in air
b	slit width in the dispersive plane
$\beta_{1,2}$	angles towards the prism surface normal in the prism material
β_c	ratio of the velocity of a particle to the speed of the light
β_{crit}	critical angle of total reflection of $\beta_{1,2}$
C	capacitance
C_F	scaling constant of the form factor to accommodate the absolute system calibration
C_R	transmissive and reflective corrections in the partial response function
c	speed of light in vacuum
$\Delta\lambda$	spectral bandwidth of a MCT detector element
$\Delta\lambda_{\mathrm{FELO}}$	spectral bandwidth of the FELO
D^*	specific detectivity
d	optical path length
d_{g}	groove spacing of a grating
d_{ref}	distance between a reference point and the observer
δ	(w/o subscript:) Dirac delta function
$\delta_{1,2}$	equivalent to $\beta_{1,2}$ for the second prism

continued on next page

List of symbols (*continued*)

e	Euler's number
η	quantum efficiency
ϵ	prism apex angle
ε_0	vacuum permittivity
$\vec{E},\ E$	electric field vector and amplitude, $E = \lvert\vec{E}\rvert$
F	$3D$ form factor
F_{long}	longitudinal component of the form factor
F^*	partial longitudinal form factor
f	frequency
Δf	electronic bandwidth
$f_{0,1,2}$	focal lengths of the mirrors $M0, M1$ and $M2$
f_{burst}	repetition rate of radiation bursts
f_c	chopping frequency
G	electronic gain factor
g	prism base length
Γ	Fourier transform of the emitted spectrum
γ	(w/o subscript:) Lorentz factor
$\gamma_{1,2}$	equivalent to $\alpha_{1,2}$ for the second prism
h	prism height from base g
I	current
i	complex number, $i = \sqrt{-1}$
$\vec{k},\ k$	wave vector and number, $k = \lvert\vec{k}\rvert$
κ	extinction coefficient
l	length, as specified in the text
l_{b}	bunch length
λ	light wavelength in vacuum
λ_j	centre wavelength of a step in a wavelength scan
M	optical magnification
m	dispersive order
m_e	electron mass
μ	mean of a Gaussian distribution

continued on next page

List of symbols (*continued*)

N	number of elements of a specified quantity
N_g	number of illuminated grating grooves
$\vec{n}$	normal vector
n	real part of the complex refractive index $\tilde{n}$
n_e	plasma electron density
$\tilde{n}$	complex refractive index
Ω	solid angle
Ω_lim	spectrometer acceptance angle
Ω_d	solid angle covered by one detector element
ω	angular frequency in vacuum
ω_p	plasma frequency
P	power
P_NEP	noise-equivalent power
P_pulse	peak power per pulse
Π	angle between the subtending surface normals of the two prisms
Ψ	deflection angle of the off-axis parabolic mirror $M2$
ψ	phase setting of the accelerating module specified in the subscript
φ	phase angle
Φ_bg	photon flux of the background radiation
ϕ	divergence induced by a focusing mirror
Q	total charge per electron bunch
q_e	elementary charge
ρ	distance between the centre of a circular plane and specified point
R	response function
R^*	partial response function
R_Ω	ohmic resistance
r_s	transition radiation screen radius
S	MCT detector signal
S_c	MCT detector signal, scaled to a specified gain setting
S_bg	baseline of the MCT detector

continued on next page

List of symbols (*continued*)

σ	width of a Gaussian function, square root of the variance of the normal distribution
σ_{bg}	sample root mean square deviation of the detector background spectra
$\overline{\sigma_{\mathrm{bg}}}$	root mean square deviation of the mean of detector background spectra
θ	total deflection angle w. r. t. the initial direction of propagation
$\mathrm{d}\theta/\mathrm{d}\lambda$	angular dispersion
Θ	observation angle
T, $\mathfrak{T}$	normalised transmission
t	time
t_i	electronic integration time
U	energy
u	voltage
v_p	phase velocity
w_2	transverse beam size in the detector plane
$\Xi = (\xi_{\#\,j})$	response matrix and their elements
x_2	transverse coordinate in the detector plane
Δx_2	linear dispersion in the detector plane
$\Delta x_{\mathrm{offset}}$	offset in the dispersive plane at the detector
Υ	absorption coefficient
z	longitudinal coordinate

Bibliography

[1]H. Wiedemann, *Particle Accelerator Physics*, Fourth ed., Graduate Texts in Physics (Springer International Publishing, 2015).

[2]P. Schmüser et al., *Free-Electron Lasers in the Ultraviolet and X-Ray Regime*, Second ed., Vol. 258, Springer Tracts in Modern Physics (Springer International Publishing, Cham, 2014).

[3]C. Behrens et al., "Few-femtosecond time-resolved measurements of X-ray free-electron lasers", Nature Communications **5**, 1–7 (2014).

[4]S. Düsterer et al., "Development of experimental techniques for the characterization of ultrashort photon pulses of extreme ultraviolet free-electron lasers", Physical Review Special Topics - Accelerators and Beams **17**, 120702 (2014).

[5]V. I. Veksler, "Coherent principle of acceleration of charged particles", CERN Symposium on High Energy Accelerators and Pion Physics **1**, 80 (1956).

[6]E. Esarey, C. Schroeder, and W. Leemans, "Physics of laser-driven plasma-based electron accelerators", Reviews of Modern Physics **81**, 1229–1285 (2009).

[7]C. Schroeder et al., "Physics considerations for laser-plasma linear colliders", Physical Review Special Topics - Accelerators and Beams **13**, 1–11 (2010).

[8]R. Lai and A. J. Sievers, "On using the coherent far IR radiation produced by a charged-particle bunch to determine its shape: I Analysis", Nuclear Instruments and Methods in Physics Research Section A: Accelerators, Spectrometers, Detectors and Associated Equipment **397**, 221–231 (1997).

[9] S. Wesch et al., "A multi-channel THz and infrared spectrometer for femtosecond electron bunch diagnostics by single-shot spectroscopy of coherent radiation", Nuclear Instruments and Methods in Physics Research Section A: Accelerators, Spectrometers, Detectors and Associated Equipment **665**, 40–47 (2011).

[10] R. W. Hamm and M. E. Hamm, *Industrial Accelerators and Their Applications* (World Scientific Publishing Company, 2012).

[11] J. P. Blewett, "Radiation Losses in the Induction Electron Accelerator", Physical Review **69**, 87–95 (1946).

[12] F. R. Elder et al., "Radiation from Electrons in a Synchrotron", Physical Review **71**, 829–830 (1947).

[13] J. D. Jackson, *Classical Electrodynamics*, Third ed. (John Wiley & Sons, Singapore, 1999).

[14] Anonymous, "Minutes of the Meeting of September 19-21, 1946 at New York", Physical Review **70**, 784–800 (1946).

[15] C. A. Brau, *Free-Electron Lasers*, Advances in electronics and electron physics: Supplement; 22 (Academic Press, 1990).

[16] Z. Huang and K.-J. Kim, "Review of x-ray free-electron laser theory", Physical Review Special Topics - Accelerators and Beams **10**, 1–26 (2007).

[17] G. Lambert et al., "Injection of harmonics generated in gas in a free-electron laser providing intense and coherent extreme-ultraviolet light", Nature Physics **4**, 296–300 (2008).

[18] M. Labat et al., "High-Gain Harmonic-Generation Free-Electron Laser Seeded by Harmonics Generated in Gas", Physical Review Letters **107**, 224801 (2011).

[19] E. Allaria et al., "Highly coherent and stable pulses from the FERMI seeded free-electron laser in the extreme ultraviolet", Nature Photonics **6**, 699–704 (2012).

[20] J. Amann et al., "Demonstration of self-seeding in a hard-X-ray free-electron laser", Nature Photonics **6**, 693–698 (2012).

[21]S. Ackermann et al., "Generation of coherent 19- and 38-nm radiation at a free-electron laser directly seeded at 38 nm", Physical Review Letters **111**, 1–5 (2013).

[22]K. Hacker et al., "First lasing of an HGHG seeded FEL at FLASH", in Proceedings of FEL2015, Daejeon, Korea (2015), pp. 646–649.

[23]H. N. Chapman et al., "Femtosecond diffractive imaging with a soft-X-ray free-electron laser", Nature Physics **2**, 839–843 (2006).

[24]H. N. Chapman et al., "Femtosecond time-delay X-ray holography", Nature **448**, 676–679 (2007).

[25]H. Ostrom et al., "Probing the transition state region in catalytic CO oxidation on Ru", Science **347**, 978–982 (2015).

[26]S. Wunderlich, "Electro-optic sampling of THz pulses at the CTR source at FLASH", Diploma Thesis, DESY-THESIS-2012-017 (Universität Hamburg, 2012).

[27]R. Wideröe, "Über ein neues Prinzip zur Herstellung hoher Spannungen", Archiv für Elektrotechnik **21**, 387–406 (1928).

[28]R. H. Varian and S. F. Varian, "A high frequency oscillator and amplifier", Journal of Applied Physics **10**, 321–327 (1939).

[29]D. W. Kerst, "The Acceleration of Electrons by Magnetic Induction", Phys. Rev. **60**, 47–53 (1941).

[30]E. M. McMillan, "The Synchrotron - A Proposed High Energy Particle Accelerator", Physical Review **68**, 143–144 (1945).

[31]E. L. Ginzton, W. W. Hansen, and W. R. Kennedy, "A Linear Electron Accelerator", Review of Scientific Instruments **19**, 89–108 (1948).

[32]M. Aicheler et al., eds., *A Multi-TeV linear collider based on CLIC technology: CLIC Conceptual Design Report* (2012).

[33]A. W. Chao and W. Chou, *Reviews of Accelerator Science and Technology: Volume 7: Colliders* (World Scientific Publishing Company, 2015).

[34]B. Aune et al., "Superconducting TESLA cavities", Physical Review Special Topics - Accelerators and Beams **3** (2000) 10.1103/PhysRevSTAB.3.092001.

[35]R. Abela et al., *XFEL: The European X-Ray Free-Electron Laser - Technical Design Report* (DESY, Hamburg, 2006).

[36]A. Navitski, A. Prudnikava, and Y. Tamashevich, "Progress of R & D on SRF cavities at DESY towards the ILC performance goal", in Proceedings of IPAC2014, Dresden, Germany (2014), pp. 2499–2501.

[37]L. Serafini and J. B. Rosenzweig, "Envelope analysis of intense relativistic quasilaminar beams in rf photoinjectors: mA theory of emittance compensation", Physical Review E **55**, 7565–7590 (1997).

[38]H. Edwards, C. Behrens, and E. Harms, "3.9 GHz cavity module for linear bunch compression at FLASH", in Proceedings of Linear Accelerator Conference LINAC2010, Tsukuba, Japan (2010).

[39]I. Zagorodnov and M. Dohlus, "Semianalytical modeling of multistage bunch compression with collective effects", Physical Review Special Topics - Accelerators and Beams **14**, 014403 (2011).

[40]A. Winter, "Fiber Laser Master Oscillators for Optical Synchronization Systems", PhD thesis, DESY-THESIS-2008-010 (Universität Hamburg, 2008).

[41]T. Tajima and J. M. Dawson, "Laser electron accelerator", Physical Review Letters **43**, 267–270 (1979).

[42]K. H. Spatschek, *Theoretische Plasmaphysik: Eine Einführung*, Teubner Studienbücher Physik (B. G. Teubner Stuttgart, 1990).

[43]I. Blumenfeld et al., "Energy doubling of 42 GeV electrons in a metre-scale plasma wakefield accelerator", Nature **445**, 741–744 (2007).

[44]O. Lundh et al., "Few femtosecond, few kiloampere electron bunch produced by a laser-plasma accelerator", Nature Physics **7**, 219–222 (2011).

[45]T. Mehrling, "Theoretical and numerical studies on the transport of transverse beam quality in plasma-based accelerators", PhD thesis, DESY-THESIS-2014-040 (Universität Hamburg, 2014).

[46]J. Faure et al., "Controlled injection and acceleration of electrons in plasma wakefields by colliding laser pulses.", Nature **444**, 737–739 (2006).

[47]W. P. Leemans et al., "GeV electron beams from a centimetre-scale accelerator", Nature Physics **2**, 696–699 (2006).

[48] W. Leemans et al., "Multi-GeV Electron Beams from Capillary-Discharge-Guided Subpetawatt Laser Pulses in the Self-Trapping Regime", Physical Review Letters **113**, 245002 (2014).

[49] J. Faure et al., "A laser-plasma accelerator producing monoenergetic electron beams", Nature **431**, 541–544 (2004).

[50] B. Schmidt, "Overview on diagnostics for X-and XUV-FEL", in Proceedings of FEL 2006, BESSY, Berlin, Germany (2006), pp. 761–768.

[51] A. W. Chao et al., *Handbook of Accelerator Physics and Engineering*, Second ed. (World Scientific Publishing Company, 2013).

[52] B. R. Steffen, "Electro-Optic Methods for Longitudinal Bunch Diagnostics at FLASH", PhD thesis, DESY-THESIS-2007-020 (Universität Hamburg, 2007).

[53] S. Schulz, "Implementation of the Laser-Based Femtosecond Precision Synchronization System at FLASH", PhD thesis, DESY-THESIS-2014-012 (Universität Hamburg, 2014).

[54] K. Kinoshita, M. Ito, and Y. Suzuki, "Femtosecond streak tube", Review of Scientific Instruments **58**, 932 (1987).

[55] A. Takahashi et al., "New femtosecond streak camera with temporal resolution of 180 fs", in Proc. SPIE, Vol. 2116, edited by R. P. Trebino and I. A. Walmsley (May 1994), pp. 275–284.

[56] R. Akre et al., "A transverse rf deflecting structure for bunch length and phase space diagnostics", in Proceedings of the 2001 Particle Accelerator Conference, Chicago, Vol. 3, June (2001), pp. 2353–2355.

[57] Y. Ding et al., "Femtosecond x-ray pulse temporal characterization in free-electron lasers using a transverse deflector", Physical Review Special Topics - Accelerators and Beams **14**, 120701 (2011).

[58] M. Röhrs et al., "Measurement of slice-emittance using a transverse deflecting structure", in Proceedings of the 27th International Free Electron Laser Conference, August (2005), pp. 541–544.

[59] T. Vinatier et al., "Measurement of low-charged electron beam with a scintillator screen", in Proceedings of IPAC2014, Dresden, Germany (2014), pp. 3456–3458.

[60]C. Behrens, C. Gerth, and I. Zagorodnov, "Numerical Performance Studies on the new Sliced-Beam-Parameter Measurement Section for FLASH", in Proceedings of FEL2009, Liverpool, UK (2009), pp. 599–602.

[61]P. Emma et al., "First lasing and operation of an ångstrom-wavelength free-electron laser", Nature Photonics **4**, 641–647 (2010).

[62]G. Gallot and D. Grischkowsky, "Electro-optic detection of terahertz radiation", Journal of the Optical Society of America B **16**, 1204 (1999).

[63]B. R. Steffen et al., "Electro-optic time profile monitors for femtosecond electron bunches at the soft x-ray free-electron laser FLASH", Physical Review Special Topics - Accelerators and Beams **12**, 032802 (2009).

[64]M. Helle et al., "Extending electro-optic detection to ultrashort electron beams", Physical Review Special Topics - Accelerators and Beams **15**, 1–11 (2012).

[65]J.-P. Schwinkendorf et al., "TADPOLE for longitudinal electron-bunch diagnostics based on electro-optic upconversion", Nuclear Instruments and Methods in Physics Research Section A: Accelerators, Spectrometers, Detectors and Associated Equipment **740**, 222–225 (2013).

[66]S. Wesch, "Echtzeitbestimmung longitudinaler Elektronenstrahlparameter mittels absoluter Intensitäts- und Spektralmessung einzelner kohärenter THz Strahlungspulse", PhD thesis, DESY-THESIS-2012-052 (Universität Hamburg, 2012).

[67]O. Grimm and P. Schmüser, "Principles of longitudinal beam diagnostics with coherent radiation", TESLA-FEL report 2006-03 (2006).

[68]I. Bronstein et al., *Taschenbuch der Mathematik*, Fourth ed., Taschenbuch der Mathematik (Verlag Harri Deutsch, 1999).

[69]E. J. Akutowicz, "On the determination of the phase of a Fourier integral. I", Transactions of the American Mathematical Society **83**, 179–179 (1956).

[70]J. R. Fienup, "Phase retrieval algorithms: a comparison", Applied Optics **21**, 2758–2769 (1982).

[71]S. Bajlekov et al., "Longitudinal electron bunch profile reconstruction by performing phase retrieval on coherent transition radiation spectra", Physical Review Special Topics - Accelerators and Beams **16**, 040701 (2013).

[72]D. Pelliccia and T. Sen, "A two-step method for retrieving the longitudinal profile of an electron bunch from its coherent radiation", Nuclear Instruments and Methods in Physics Research Section A: Accelerators, Spectrometers, Detectors and Associated Equipment **764**, 206–214 (2014).

[73]E. Hass et al., "Longitudinal bunch profile reconstruction using broadband coherent radiation at FLASH", in Proceedings of IBIC2013, Oxford, UK (2014), pp. 154–157.

[74]R. Trebino et al., "Measuring ultrashort laser pulses in the time-frequency domain using frequency-resolved optical gating", Review of Scientific Instruments **68**, 3277 (1997).

[75]M. Zolotorev and G. V. Stupakov, "Spectral fluctuations of incoherent radiation and measurement of longitudinal bunch profile", in Proceedings of the 1997 Particle Accelerator Conference, Vol. i (1997), pp. 2180–2182.

[76]P. Catravas et al., "Measurement of Electron-Beam Bunch Length and Emittance Using Shot-Noise-Driven Fluctuations in Incoherent Radiation", Physical Review Letters **82**, 5261–5264 (1999).

[77]B. Smit, "Analysis of Femtosecond Electron Bunches at the SwissFEL Injector Test Facility", PhD thesis (SB, Lausanne, 2015).

[78]V. L. Ginzburg and V. N. Tsytovich, *Transition Radiation and Transition Scattering,* Adam Hilger series on plasma physics (Taylor & Francis, 1990).

[79]S. Casalbuoni, B. Schmidt, and P. Schmüser, "Far-Infrared Transition and Diffraction Radiation Part I: Production, Diffraction Effects and Optical Propagation", TESLA Report **15**, 1–41 (2005).

[80]M. Born and E. Wolf, *Principles of Optics: Electromagnetic theory of propagation, interference and diffraction of light*, Seventh ed. (Cambridge University Press, 1999).

[81]M. Castellano et al., "Effects of diffraction and target finite size on coherent transition radiation spectra in bunch length measurements", Nuclear Instruments and Methods in Physics Research **435**, 297–307 (1999).

[82]H. Günzler and H. Böck, *IR-Spektroskopie: eine Einführung*, Second ed., Studienbücher der instrumentellen Analytik (Verlag Chemie, 1983).

[83]P. Temi et al., "The SOFIA Observatory at the Start of Routine Science Operations: Mission Capabilities and Performance", The Astrophysical Journal Supplement Series **212**, 24 (2014).

[84]N. Rangwala et al., "First Extragalactic Detection of Submillimeter Ch Rotational Lines From the Herschel Space Observatory", The Astrophysical Journal **147** (2014) 10.1088/0004-637X/788/2/147.

[85]E. Hecht, *Optics*, Fourth ed. (Addison-Wesley, 2002).

[86]W. Demtröder, *Laser Spectroscopy Volume 1*, Fourth ed., Laser Spectroscopy (Springer-Verlag, 2008).

[87]H. Delsim-Hashemi, "Infrared Single Shot Diagnostics for the Longitudinal Profile of the Electron Bunches at FLASH", PhD thesis, DESY-THESIS-2008-024 (Universität Hamburg, 2008).

[88]P. Jacquinot, "The Luminosity of Spectrometers with Prisms, Gratings, or Fabry-Perot Etalons", Journal of the Optical Society of America **44**, 761 (1954).

[89]T. Maxwell et al., "Coherent-Radiation Spectroscopy of Few-Femtosecond Electron Bunches Using a Middle-Infrared Prism Spectrometer", Physical Review Letters **111**, 184801 (2013).

[90]B. Tatian, "Fitting refractive-index data with the Sellmeier dispersion formula.", Applied Optics **23**, 4477 (1984).

[91]W. S. Rodney and I. H. Malitson, "Refraction and Dispersion of Thallium Bromide Iodide", Journal of the Optical Society of America **46**, 956 (1956).

[92]H. H. Li, "Refractive index of alkali halides and its wavelength and temperature derivatives", Journal of Physical and Chemical Reference Data **5**, 329–528 (1976).

[93]W. L. Wolfe and G. J. Zissis, *The Infrared Handbook*, Revised ed. (Environmental Research Institute of Michigan for the Office of Naval Research, Department of the Navy, Washington, DC, 1993).

[94]A. Rogalski et al., *Infrared photon detectors*, SPIE Press Monographs (SPIE - Optical Engineering Press, 1995).

[95]P. Horowitz and W. Hill, *The Art of Electronics*, 2nd ed. (Cambridge University Press, Cambridge, New York, 1989).

[96]Z. Celik-Butler et al., "Room-temperature operation of a YBaCuO microbolometer", in Proc. SPIE, Vol. 2999 (1997), pp. 348–356.

[97]Y. P. Gousev et al., "Broad-band coupling of THz radiation to an hot-electron bolometer mixer", Superconductor Science and Technology **9**, 779–787 (1999).

[98]M. J. E. Golay, "A pneumatic infra-red detector", Review of Scientific Instruments **18**, 357–362 (1947).

[99]S. W. Kurnick and R. N. Zitter, "Photoconductive and photoelectromagnetic effects in InSb", Journal of Applied Physics **27**, 278–285 (1956).

[100]Hamamatsu Photonics K.K. Solid State Division, *Technical Information SD-12: Characteristics and use of infrared detectors*, tech. rep. (2004).

[101]S. Nudelman, "The Detectivity of Infrared Photodetectors", Applied Optics **1**, 627 (1962).

[102]J. R. Schneider, "FLASH - from accelerator test facility to the first single-pass soft x-ray free-electron laser", Journal of Physics B: Atomic, Molecular and Optical Physics **43**, 194001 (2010).

[103]M. J. V. Streeter, "Ultrafast Dynamics of Relativistic Laser Plasma Interactions", PhD thesis (Imperial College London, 2013).

[104]C. Palmer, *Expected electron beam parameters for the LWFA experiment at ASTRA-GEMINI*, private communication, 2013.

[105]J. Rönsch-Schulenburg et al., "Operation of FLASH With Short SASE-FEL Radiation Pulses", in Proceedings of FEL2014, Basel, Switzerland, 6 (2014), pp. 342–345.

[106]B. Schmidt, *THzTransport*, private communication, 2014.

[107]Wolfram Research Inc., *Mathematica 9.0.1*, 2013.

[108]T. Ishikawa et al., "A compact X-ray free-electron laser emitting in the sub-ångström region", Nature Photonics **6**, 540–544 (2012).

[109]J.-C. Diels and W. Rudolph, *Ultrashort Laser Pulse Phenomena*, Second ed. (Academic Press, 2006).

[110]Infrared Systems Development Corp., Winter Park, FL, USA.

[111]InfraRed Associates Inc., *LN2-cooled MCT detectors*, http://irassociates.com/, online, accessed 26th of May 2015.

[112]National Instruments Corp., *LabView 13.0f2*, 2013.

[113]D. Ware and P. Mansfield, "High Stability "Boxcar" Integrator for Fast NMR Transients in Solids", Review of Scientific Instruments **37**, 1167 (1966).

[114]O. Zarini, "Entwicklung eines breitbandigen optischen Spektrometers zur Pulsdauermessung ultrakurzer Elektronenpulse", Diploma Thesis (Technische Universität Dresden, 2013).

[115]J. Weiss, M. Winkenbach, and U. Kilian, *Der Brockhaus Naturwissenschaft und Technik, Bd. 2: Ge bis Pg* (Brockhaus, 2003).

[116]I. Newton, *Opticks: Or a treatise of the reflections, refractions, inflections and colours of light. (based on the 4th ed., London 1730)* (Dover, New York, 1952).

[117]M. V. Murty and A. L. Narasimham, "Some new direct vision dispersion prism systems.", Applied Optics **9**, 859–862 (1970).

[118]N. Hagen and T. S. Tkaczyk, "Compound prism design principles, I.", Applied Optics **50**, 4998–5011 (2011).

[119]W. S. Franklin and B. MacNutt, *Light and sound: a text-book for colleges and technical schools* (Franklin and Charles, Bethlehem, Pa., 1909), p. 344.

[120]F. Duarte and J. Piper, "Dispersion theory of multiple-prism beam expanders for pulsed dye lasers", Optics Communications **43**, 303–307 (1982).

[121]F. Duarte, "Generalized multiple-prism dispersion theory for laser pulse compression: higher order phase derivatives", Applied Physics B **96**, 809–814 (2009).

[122]J. E. Howard, "Imaging properties of off-axis parabolic mirrors.", Applied Optics **18**, 2714–2722 (1979).

[123]ZEMAX LLC., *Optic Studio 14.2*, 2015.

[124]LT-Ultra-Precision-Technology GmbH, Herdwangen-Schönach, Germany, 2013.

[125]Korth Kristalle GmbH, Altenholz, Germany, 2013.

[126]Edmund Optics Inc., Barrington, NJ, USA, 2013.

[127]W. Seidel et al., "The THz user facility FELBE at the radiation source ELBE of Helmholtz-Zentrum Dresden-Rossendorf", International Conference on Infrared, Millimeter, and Terahertz Waves, IRMMW-THz, 4717 (2013).

[128]D. Oepts, A. F. G. Van Der Meer, and P. W. Van Amersfoort, "The Free-Electron-Laser user facility FELIX", Infrared Physics and Technology **36**, 297–308 (1995).

[129]R. A. Kaindl et al., "Generation, shaping, and characterization of intense femtosecond pulses tunable from 3 to 20 μm", Journal of the Optical Society of America B **17**, 2086 (2000).

[130]S. Haidar, K. Miyamoto, and H. Ito, "Generation of tunable mid-IR (5.5-9.3 μm) from a 2-μm pumped ZnGeP2 optical parametric oscillator", Optics Communications **241**, 173–178 (2004).

[131]Laser Components GmbH and Northumbria Optical Coatings Ltd., *Infrared narrow band pass filters*, 2013.

[132]J. Ashok, L. Varaprasad, and J. Birch, "Polyethylene $(C_2\,H_4)_n$ ", in *Handbook of optical constants of solids ii*, edited by E. D. Palik (Academic Press, San Diego, 1998), pp. 957–987.

[133]D. Lipka et al., "Dark current Monitor for the European XFEL", WEOC03, Proceedings of DIPAC, Hamburg, Germany, 572–574 (2011).

[134]P. Piot et al., "Generation and characterization of electron bunches with ramped current profiles in a dual-frequency superconducting linear accelerator", Physical Review Letters **108**, 1–4 (2012).

[135]InfraSpecs, Filderstadt, Germany, 2014.

[136]W. S. Zhu, J. R. Izatt, and B. K. Deka, "Pyroelectric detection of submicrosecond laser pulses between 230 and 530 microm.", Applied Optics **28**, 3647–3651 (1989).

[137]R. C. Webber, "Tutorial on beam current monitoring", AIP Conference Proceedings **546** (2000).

[138]L. S. Rothman et al., "The HITRAN2012 molecular spectroscopic database", Journal of Quantitative Spectroscopy and Radiative Transfer **130**, 4–50 (2013).

[139] V. E. Zuev and V. S. Komarov, *Statistical models of the temperature and gaseous components of the atmosphere (Atmospheric sciences library)* (D. Reidel Publishing Company, 1987).

[140] Harvard-Smithsonian Center for Astrophysics Cambride USA and V. E. Zuev Insitute of Atmosperic Optics Tomsk Russia, *Hitran on the Web*, 2014.

[141] C. A. Klein, R. P. Miller, and D. L. Stierwalt, "Surface and bulk absorption characteristics of chemically vapor-deposited zinc selenide in the infrared.", Applied Optics **33**, 4304–13 (1994).

[142] The MathWorks Inc., *Matlab R2013b*, 2013.

[143] FELIX Laboratory Radboud University, *Overview and specifications of the FELIX facility*, http://www.ru.nl/felix/facility-0/overview/, online, accessed 8th of October 2015.

[144] Lasnix, *Infrared Step Attenuators*, Berg, Germany, 2015.

[145] T. Kövener, "THz Spectrometer Calibration at FELIX", Master thesis (Universität Hamburg, 2016).

[146] Infrared Systems Development Corp., *Improvement of MCT detector grounding*, private communication, 2015.

[147] T. Plath et al., "Commissioning and diagnostics development for the new short-pulse injector laser at FLASH", in Proceedings of IBIC2013, Oxford, UK (2013), pp. 353–356.

[148] B. Schmidt, *Phase retrieval algorithm*, private communication, 2016.

[149] S. Wunderlich et al., "A Double-Prism Spectrometer for the Longitudinal Diagnosis of Femtosecond Electron Bunches with Mid-Infrared Transition Radiation", in Proceedings of IBIC2014, Monterey, CA, USA (2014), pp. 157–160.

[150] J. R. Taylor, *Fehleranalyse*, First ed. (VCH, Weinheim, 1988).

[151] D. Lipka, *Dark Current Monitor at FLASH*, private communication, 2016.

[152] F. Richard et al., "TESLA, The Superconducting Electron Positron Linear Collider with an Integrated X-ray Laser Laboratory, Technical Design Report Part 1", DESY-2001-011 (2001).

[153]D. Edwards (ed.), "TESLA Test Facility Linac - Design Report", TESLA Report, pages (1995).

[154]DESY, "A VUV Free Electron Laser at the TESLA Test Facility at DESY", TESLA-FEL report (1995).

[155]J. Andruszkow et al., "First Observation of Self-Amplified Spontaneous Emission in a Free-Electron Laser at 109 nm Wavelength", Physical Review Letters **85**, 3825–3829 (2000).

[156]S. Schreiber and B. Faatz, "First Lasing at FLASH II", in Proceedings of FEL2014, Basel, Switzerland (2014), pp. 7–8.

[157]A. Aschikhin et al., "The FLASHForward facility at DESY", Nuclear Instruments and Methods in Physics Research Section A: Accelerators, Spectrometers, Detectors and Associated Equipment **806**, 175–183 (2016).

[158]F. Stulle, "A Bunch Compressor for small Emittances and high Peak Currents at the VUV Free-Electron Laser", PhD thesis, DESY-THESIS-2004-041 (Universität Hamburg, 2004).

[159]M. Vogt et al., "The Free-Electron Laser FLASH at DESY", in Proceedings of IPAC2013, Shanghai, China (2013), pp. 1167–1169.

[160]S. Schreiber et al., "Simultaneous operation of three laser systems at the FLASH photoinjector", in Proceedings of FEL2015, Daejeon, Korea (2015), pp. 459–463.

[161]S. Casalbuoni et al., "Ultrabroadband terahertz source and beamline based on coherent transition radiation", Physical Review Special Topics - Accelerators and Beams **12**, 030705 (2009).

[162]E. Hass, "Longitudinal phase space diagnostics using coherent radiation at FLASH", working title, to be submitted, PhD thesis (Universität Hamburg, 2016).

[163]S. Wunderlich et al., "Broadband measurements of transition radiation at Astra-Gemini", Central Laser Facility Annual Report 2013-2014 (2014).

[164]N. Bourgeois, J. Cowley, and S. M. Hooker, "Two-Pulse Ionization Injection into Quasilinear Laser Wakefields", Physical Review Letters **111**, 155004 (2013).

[165] P. Biswas et al., "Effects of tin on IR reflectivity, thermal emissivity, Hall mobility and plasma wavelength of sol-gel indium tin oxide films on glass", Materials Letters **57**, 2326–2332 (2003).

[166] Präzisions Glas & Optik GmbH, Iserlohn, Germany, 2013.

[167] Universität Duisburg-Essen, Fachbereich Mathematik, AG Prof. Dr. Törner, Humboldt-Universität zu Berlin, AG Elektronisches Publizieren, J. Rycko, and Deutsche Nationalbibliothek, *DFG-Projekt DissOnlineTutor*, 2011.

[168] Mendeley Ltd., *Reference manager Mendeley Desktop*.

[169] N. Schlömer, *matlab2tikz*, online, via MathWorks MatlabCentral (http://www.mathworks.com/matlabcentral/).

[170] M. Niccoli, *Perceptually improved colormaps*, online, via MathWorks MatlabCentral (http://www.mathworks.com/matlabcentral/).

List of publications

[1]A. Aschikhin, C. Behrens, S. Bohlen, J. Dale, N. Delbos, L. di Lucchio, E. Elsen, J.-H. Erbe, M. Felber, B. Foster, L. Goldberg, J. Grebenyuk, J.-N. Gruse, B. Hidding, Z. Hu, S. Karstensen, A. Knetsch, O. Kononenko, V. Libov, K. Ludwig, A. Maier, A. Martinez de la Ossa, T. Mehrling, C. Palmer, F. Pannek, L. Schaper, H. Schlarb, B. Schmidt, S. Schreiber, J.-P. Schwinkendorf, H. Steel, M. Streeter, G. Tauscher, V. Wacker, S. Weichert, S. Wunderlich, J. Zemella, and J. Osterhoff, "The FLASHForward facility at DESY", Nuclear Instruments and Methods in Physics Research Section A: Accelerators, Spectrometers, Detectors and Associated Equipment **806**, 175–183 (2016).

[2]S. Wunderlich, C. Palmer, J.-P. Schwinkendorf, J. Osterhoff, B. Schmidt, J. Cowley, N. Bourgeois, A. Dyson, G. Cheung, C. Thornton, S. M. Hooker, S. J. Hawkes, N. Booth, and D. R. Symes, "Broadband measurements of transition radiation at Astra-Gemini", Central Laser Facility Annual Report 2013-2014 (2014).

[3]S. Wunderlich, E. Hass, M. Yan, and B. Schmidt, "A Double-Prism Spectrometer for the Longitudinal Diagnosis of Femtosecond Electron Bunches with Mid-Infrared Transition Radiation", in Proceedings of IBIC2014, Monterey, CA, USA (2014), pp. 157–160.

[4]J. Rönsch-Schulenburg, E. Hass, N. M. Lockmann, T. Plath, M. Rehders, J. Roßbach, G. Brenner, S. Dziarzhytski, T. Golz, H. Schlarb, B. Schmidt, E. Schneidmiller, S. Schreiber, N. Stojanovic, S. Wunderlich, and M. Yurkov, "Operation of FLASH With Short SASE-FEL Radiation Pulses", in Proceedings of FEL2014, Basel, Switzerland, 6 (2014), pp. 342–345.

[5]J.-P. Schwinkendorf, S. Wunderlich, L. Schaper, B. Schmidt, and J. Osterhoff, "TADPOLE for longitudinal electron-bunch diagnostics based on

electro-optic upconversion", Nuclear Instruments and Methods in Physics Research Section A: Accelerators, Spectrometers, Detectors and Associated Equipment **740**, 222–225 (2013).

[6]S. Wunderlich, S. Schefer, B. Schmidt, S. Schulz, S. Wesch, and M. C. Hoffmann, "Characterization of single-cycle THz pulses at the CTR source at FLASH", in Proceedings of FEL2012, Nara, Japan (2012), pp. 500–502.

[7]S. Wunderlich, "Electro-optic sampling of THz pulses at the CTR source at FLASH", Diploma Thesis, DESY-THESIS-2012-017 (Universität Hamburg, 2012).

[8]M. C. Hoffmann, S. Schulz, S. Wesch, S. Wunderlich, A. Cavalleri, and B. Schmidt, "Coherent single-cycle pulses with MV/cm field strengths from a relativistic transition radiation light source.", Optics letters **36**, 4473–5 (2011).

[9]M. C. Hoffmann, S. Schulz, S. Wesch, S. Wunderlich, and B. Schmidt, "MV/cm THz pulses from a coherent transition radiation source", in Proceedings of the 2011 International Conference on Infrared, Millimeter, and Terahertz Waves (Oct. 2011), pp. 1–2.

Acknowledgements - Danksagungen

- Dr. Bernhard Schmidt und Dr. Jens Osterhoff danke ich für die Aufnahme in die Arbeitsgruppe FLA und die Begleitung der Promotion. Von den kritischen und stets den Kern des Problems treffenden Diskussionen haben meine wissenschaftliche Arbeit und ich sehr profitiert.

- Prof. Dr. Jörg Roßbach, Dr. Bernhard Schmidt und Dr. Jens Osterhoff haben in Vorlesungen schon im Diplomstudium mein Interesse an der Beschleunigerphysik geweckt.

- Für den in der Bewertung dieser Arbeit entstandenen Aufwand möchte ich auch den Gutachtern und der Prüfungskommission danken.

- Mit Dr. Laurens Wissmann, Eugen Hass, Toke Kövener und Carlos Entrena-Utrilla als Büronachbarn wurde der Arbeitstag nicht nur angenehm, sondern oft durch vielfältige Diskussionen spannend und lehrrich gestaltet.

- Während der Strahlzeiten bei FLASH, ASTRA-GEMINI und FELIX war auf Eugen Hass, Jan-Patrick „JP“ Schwinkendorf, Dr. Charlotte Palmer, Toke Kövener und Dr. Peter Peier stets Verlass.

- Besonderer Dank geht an Dr. Charlotte Palmer für viele Diskussionen über physikalische und experimentelle Probleme und das Lektorat dieser Arbeit.

- Die Expertise von Dr. Christopher Behrens, Dr. Stephan Wesch und Dr. Sebastian Schulz, u. a. zur experimentellen Arbeit, stellte eine nicht vernachlässigbare Unterstützung dar.

- Mit euch, Eugen, Toke, Carlos, John, Slava, Matt, Lars, Lucas, JP, Charlotte, Timon und Arvid sowie allen unerwähnten habe ich auch außerhalb der Arbeit eine gute Zeit verbracht.

- Ursula „Uschi“ Djuanda und Iris Wetstein möchte ich für Unterstüzung in vielen Dingen des Arbeitsalltags danken.

- Kai Ludwig, Amir Rahali und Andrej Schleiermacher standen mir mit der wertvollen Unterstützung in technischen Belangen stets zur Seite. Auch bleiben die Beiträge von Albert Schleiermacher und Matthias Hoffmann immer in Erinnerung.

- Nicht unerwähnt bleiben darf die Unterstützung der Gruppe MCS, namentlich unter anderen Kay Rehlich, Thomas Bruns, Gerhard Schlesselmann, Philip Pototzki sowie Ludwig und Gevorg Petrosyan.

- Dr. Katja Honkavaara, Dr. Siegfried Schreiber, Dr. Bart Faatz und Dr. Mathias Vogt haben mir, neben der Schichtbesatzung, den Betrieb von FLASH näher gebracht und hierdurch zum Erfolg der gezeigten Messungen beigetragen. Dank gilt auch Dr. Juliane Rönsch-Schulenburg und Dr. Bernd Steffen.

- Dr. Britta Redlich und Dr. Alexander F. G. van der Meer, sowie dem FELIX-Team, gilt besonderer Dank für die Ermöglichung der Kalibrationsmessungen bei FELIX.

- Meinen Freunden, Kommilitonen sowie meiner Familie möchte ich für die großartige Unterstützung im Studium und während der Promotion danken.

Eidesstattliche Versicherung

Hiermit erkläre ich an Eides statt, dass ich die vorliegende Dissertationsschrift selbst verfasst und keine anderen als die angegebenen Quellen und Hilfsmittel benutzt habe.

Steffen Wunderlich
Hamburg, den 22.06.2016